Entwicklung von quantenmechanischen Simulationsmethoden zu computergestützten Materialdesign

Dissertation
for the acquisition of the academic title
Doktor-Ingenieur (Dr.-Ing.) in Materials Science.

submitted to the Council of the Faculty of Physics and Astronomy
of the Friedrich Schiller University in Jena

by M.S. Roman Łazarski
born in Rabka-Zdrój on 29.09.1988

Date of defence:
15.08.2017

Reviewers:
Prof. Dr. Marek Sierka, Friedrich-Schiller-Universität Jena
Prof. Dr. Thomas Heine, Universität Leipzig
Prof. Dr. Christof Hättig, Ruhr-Universität Bochum

I would like to dedicate this doctoral dissertation to my family,
especially to my parents and wife.

Contents

1 Introduction **5**
- 1.1 Motivation 5
- 1.2 Density Functional Theory for Molecular and Periodic Systems . . . 6
- 1.3 Metal-Oxide Nanoclusters 8

2 Density Functional Theory **13**
- 2.1 General Theory 13
  - 2.1.1 Basic Equations 13
  - 2.1.2 Density Fitting Scheme 16
- 2.2 Energy Calculation 18
  - 2.2.1 Coulomb Term: DF-Accelerated CFMM 18
  - 2.2.2 Exchange-Correlation Term 24
- 2.3 Energy Gradient 27
  - 2.3.1 Coulomb Term 27
  - 2.3.2 Exchange-Correlation Term 27
- 2.4 Implementation Details 28
- 2.5 Performance 30
  - 2.5.1 Energy 31
  - 2.5.2 Energy Gradients 38

3 Applications **45**
- 3.1 ZnO and CdO Nanoclusters 46
  - 3.1.1 Methods 47
  - 3.1.2 Results and Discussion 48
- 3.2 Mixed ZnO-TiO_2 Materials 65
  - 3.2.1 Computational Methods 66
  - 3.2.2 Results 67

4 Conclusions and Future Investigation **77**

4.1 Density Functional Theory for Molecular and Periodic Systems . . . 77
4.2 ZnO and CdO Nanoclusters 77
4.3 Mixed ZnO-TiO_2 Materials 79

A Multipole Expansion 81

B Details of Performance Analysis 83
B.1 Model Systems 83
B.2 Methods and Basis Sets 84

C Computational Details 87
C.1 Vertical Detachment Energy 87
C.2 Methods for ZnO 87
C.3 Methods for CdO 91
C.4 Methods for Mixed ZnO - TiO_2 Materials 91

Bibliography 93

Abstract:

Computationally aided development of novel materials requires an efficient and reasonably accurate simulation methods capable of describing both molecular as well as extended systems on an equal footing. Therefore, the methodological part of this thesis is devoted to an efficient implementation of density functional theory within the TURBOMOLE program package, which enables simulations of both molecules and extended systems under periodic boundary conditions on an equal footing.

Specifically, my contribution has been the improvement of efficiency and usability of the program by addressing its bottlenecks, extension to open shell systems and implementation of analytical energy gradients. In particular, an efficient, octree-based continuous fast multiple method has been implemented in order to significantly speed up Coulomb energy and gradient calculation.

With the improved efficiency and usability this implementation has been applied to atomic level structural characterization of ZnO and CdO nanoclusters. As the result, not only new structures are discovered, but it is also possible to demonstrate that their extraordinary long-lived excited states are due to electron–hole pair localization combined with structural rigidity of the nanoclusters.

Finally, mixed ZnO-TiO_2 nanoclusters as well as ZnO clusters adsorbed on the anatase (101) surface have been investigated. Striking structural similarities between structures of mixed ZnO-TiO_2 and pure TiO_2 clusters are found. In case of ZnO nanoclusters adsorbed on the anatase surface a significant reduction of the band gap of the system is shown. This suggest the way to tune electronic properties of TiO_2-based materials, in particular for solar cell applications, by deposition of ZnO nanoclusters on anatase-like nanostructures.

Keywords: density functional theory, periodic systems, resolution of identity, density fitting, lattice sums

Zusammenfassung:

Die rechnergestützte Entwicklung neuartiger Materialien erfordert effiziente und genaue Simulationsmethoden, die sowohl molekulare als auch periodische Systeme gleichermaßen gut beschreiben. Daher ist der methodische Teil dieser Arbeit einer recheneffizienten Implementierung der Dichtefunktionaltheorie innerhalb des TURBOMOLE-Programmpakets gewidmet, welche die Simulation von molekularen und ausgedehnten Systemen unter periodischen Randbedingungen erlaubt.

Hierbei bestand mein Beitrag in der Steigerung der Recheneffizienz und Verwendbarkeit des Programms durch die Bearbeitung der rechenintensivsten Programmteile, dessen Erweiterung für offenschalige Systeme sowie die Implementierung analytischer Energiegradienten. Dabei spielt die Implementierung einer “Octree”-basierten “continuous fast multipole” Methode zur deutlichen Beschleunigung der Berechnung der Coulombenergie und deren Gradient eine besondere Rolle.

Mit der verbesserten Effizienz und Verwendbarkeit des Programms gelang die strukturelle Charakterisierung von ZnO- und CdO-Nanoclustern auf atomaren Niveau. Im Ergebnis wurden nicht nur neuartige Strukturen entdeckt, sondern es war auch möglich zu zeigen, dass die außergewöhnlich langen Lebenszeiten der angeregten Zustände der Nanocluster in Zusammenhang mit der Lokalisierung von Elektronen-Loch-Paaren und deren struktureller Steifigkeit stehen.

Schließlich erfolgte ebenso die Untersuchung von ZnO- und gemischten ZnO-TiO_2-Nanoclustern, die auf der (101)-Anatasoberfläche adsorbieren. Im Fall von ZnO-Nanoclustern führte die Adsorption auf der Anatasoberfläche zu einer deutlichen Reduktion der Bandlücke. Dies zeigt einen möglichen Weg auf die elektronischen Eigenschaften von TiO_2-basierten Materialien durch die Abscheidung von ZnO-Nanoclustern auf anatas-ähnlichen Nanostrukturen gezielt zu beeinflussen, insbesondere für die Anwendung in Solarzellen.

This dissertation was typeset using LaTeX 2_e with TeXworks 0.4.5 as a text editor. Detailed informations about LaTeX and TeXworks are available at http://www.latex-project.org and https://www.tug.org/texworks, respectively.

The following software was used for this project:
VMD 1.9.1
Material Studio 7.0
Gimp 2.8.10
Microsoft Office 2016

CHAPTER 1

Introduction

1.1 Motivation

Computational studies of complex materials, for instance solid catalysts, photoactive materials or ceramics, often involve simulations of model systems with different dimensionality - small particles and molecules, models of surfaces, thin films and bulk materials. Such simulations require an efficient and accurate method capable of consistent description of both molecular and extended systems. Therefore, the methodological part of my thesis focuses on further development of a new extension of the TURBOMOLE program package,[1,5] which enables simulations of both molecules and extended systems under periodic boundary conditions (PBC) on an equal footing using density functional theory (DFT) methods. Specifically, the efficiency and usability of the program has been improved by addressing current bottlenecks, extending it to open shell systems, implementing shared-memory parallelization and energy gradients.

With the improved efficiency and usability the program has been applied to atomic level structural characterization of ZnO and CdO nanoclusters as well as ZnO nanoclusters adsorbed on the (101) surface of anatase. This work is motivated by the application of ZnO, CdO and TiO_2 based materials, particularly in nanostructured form, as potential bulding blocks for cluster assembled materials (CAM) and materials for dye-sensitized solar cells. The calculations presented in this thesis have been performed within a joint project with the experimental group of Prof. Dr. Gerd Ganteför at the University of Konstanz. They have performed time-resolved photoelectron spectroscopic studies of ZnO and CdO nanoclusters in gas phase and discovered an unusual behavior - extraordinary long-lived excited states. However, the interpretation of the experiments and full understanding of this behavior has not been possible without the aid of DFT calculations described in my thesis. As the result, not only new structures of ZnO and CdO clusters are discovered, but it is also possible to demonstrate that the extraordinary long-lived excited states are due to electron–hole pair localization combined with structural rigidity of the nanoclusters. In addition, an unprecedented ”inverse quantum confinement effect” in ZnO and CdO clusters - the decrease of the band gap with decreasing cluster size is discovered.

In the last part of my thesis mixed ZnO-TiO_2 nanoclusters as well as ZnO clusters adsorbed on the anatase (101) surface have been investigated. Striking structural similarities have been found between structures of mixed ZnO-TiO_2 and pure TiO_2 clusters as well as the "inverse quantum confinement effect" in ZnO-TiO_2 clusters is shown. For ZnO nanoclusters adsorbed on the anatase surface a significant reduction of the band gap in the system has been found. This suggest the way to tune electronic properties of TiO_2-based materials, in particular for solar cell applications, by deposition of ZnO nanoclusters on anatase-like nanostructures.

1.2 Density Functional Theory for Molecular and Periodic Systems

The relatively low computational cost combined with accuracy makes DFT methods important tools in contemporary computational chemistry and physics. DFT calculations are typically performed using a finite set of basis functions in order to solve algebraic rather than differential equations. The most common basis sets are plane waves (PW) and Gaussian-type orbitals (GTO).[52] PW are inherently periodic in three dimensions (3D) and require large simulation cells for calculations of lower dimensional systems – molecules (0D), chains and polymers (1D) or surfaces (2D) – in order to prevent overlapping of periodic images of the charge density. In contrast, GTO allow for treating systems of any dimensionality on an equal footing without the need for constructing artificial 3D periodic models.[46,85] GTO are also particularly well suited for DFT calculations on sparsely packed systems, such as zeolites and metal-organic frameworks.[46,85]

When using GTO, the computationally most demanding parts of DFT calculations are the electronic Coulomb (J) and exchange-correlation (E_{XC}) contributions. For the E_{XC} part several efficient numerical integration algorithms exist,[23,126,132,133] among them the hierarchical scheme implemented in TURBOMOLE, capable of achieving $O(N)$ scaling for systems of any dimensionality.[28] Due to the long range nature of electrostatic interactions, an efficient evaluation of the Coulomb term is a much more challenging task, in particular under periodic boundary conditions.[29,52,85] For GTO-based molecular and periodic DFT calculations the continuous fast multipole method (CFMM)[85,86,125,151] is computationally one of the most efficient approaches. In CFMM, the Coulomb problem is partitioned into far-field (FF) and near-field (NF) portions. The FF part which comprises the major part of interactions including the long-ranged crystal part is evaluated very efficiently using multipole expansions. The NF interactions are treated by a direct integration and represent computationally the most demanding part for both molecular and periodic systems.[125]

The computational cost of the direct integration can be significantly reduced by using the density fitting (DF) procedure, also known as resolution of identity (RI) approximation.[13,47,51,137] In this method the electron density is approximated by a linear combination of atom-centred auxiliary basis functions. The corresponding expansion coefficients are determined by minimization of the difference between exact and auxiliary electron density in a particular metric. It has been shown that among different metric choices the Coulomb one leads to a variational problem and the smallest fitting error.[71,137] For molecular systems very efficient methods combining DF with multipole expansions[122] or the continuous fast multipole method (CFMM)[123] have been developed. They allow to reduce the asymptotic scaling to nearly $O(N)$. However, the extension of DF approximation to periodic systems is not straightforward, due to a slow decay behaviour of the auxiliary density expansion coefficients and divergent terms in the Coulomb metric matrix under periodic boundary conditions (PBC).[71,139] To circumvent these problems several methods have been developed, including the use of non-Coulomb metrics,[71,139] introducing basis sets comprising GTO and chargeless Poisson basis functions,[94] combining electron and nuclear charge densities,[48,67] and restricting the fitting domain.[66] The Coulomb lattice sums within these methods are usually evaluated using the Ewald summation technique.[53] The basis for my thesis is the recent fast and robust DF scheme for molecular and periodic systems operating entirely in direct space, that has been developed by Burow et. al.[29] Its core is the decomposition of auxiliary density into charged and chargeless parts. The use of the Coulomb metric under periodic boundary conditions constraints the charged part. The determination of the chargeless component is variational and involves only convergent Coulomb lattice sums.

In my thesis a full GTO-based DFT implementation has been developed that treats molecules as well as extended systems with 1D, 2D and 3D periodicity on an equal footing. The novel aspect and the core of the implementation is a combination of DF and CFMM. Furthermore, the resulting DF-CFMM scheme for calculation of the Coulomb interactions and the numerical scheme for exchange-correlation term[28] are extended to energy gradients. This is an important component of any electronic structure theory code that enables evaluation of forces acting on nuclei, location of stationary points on potential energy surfaces and conducting molecular dynamics simulations.[24,27,77,119]

Computational efficiency and asymptotic $O(N)$ scaling behaviour of the implementation is demonstrated for various molecular and periodic model systems (see sec. B.1). It is shown, that that the DF-CFMM scheme allows calculation of both energy and its gradient with efficiency competitive to DF algorithms based on PW.[8,31,92,138]

1.3 Metal-Oxide Nanoclusters

With the improved efficiency and usability the DFT implementation developed in my thesis has been applied to atomic level structural characterization of ZnO and CdO nanoclusters as well as ZnO nanoclusters adsorbed on the (101) surface of anatase. At the nano- and subnanoscale, some properties of nanostructured metal oxides can be very different from those of their atomic and bulk counterparts. The extreme confinement due to the proximity of the interfaces stabilizes new structures and phases that otherwise cannot be obtained as bulk materials.[81] This opens new possibilities for the development of highly functional tailor-made structures by a bottom up approach with clusters serving as building blocks, leading to the so-called cluster-assembled materials (CAMs).[32,37]

There are special prerequisites for clusters to serve as such building blocks, namely, a very rigid structure that also favours three-dimensional assembly and large HOMO–LUMO gaps to prevent fusion of clusters.[32] To this date, fullerites with carbon fullerenes as building blocks that meet all of these requirements present the only CAM obtained from gas-phase entities.[55,99] However, theoretical predictions indicate that new crystalline phases may be accessible via coalescence of size-selected clusters with ZnO, CdO, and MgO as prominent examples.[6,12,32,37,81] For these clusters, highly symmetric alternant cage structures have been predicted.[40–42,54,60,80,114,136,142,143,145,152] Unlike carbon fullerenes comprising five- and six-membered rings, these cages are constructed from rings containing four and six atoms. This tendency arises from the need to avoid homobonding. Similar highly symmetric alternant cage structures have been predicted for numerous binary semiconductors $(XY)_n$ including other species from groups II-VI[61,93,95,97,102,134,135,144] and III-V[38,39,78,98,117,127,128,153,158,160] compounds.

Small clusters have been found to show a strong size dependence ("every atom counts")[68] of their properties such as the gas phase stability,[42] and catalytic activity.[17,87] For example, an unusually long-lived excited state has been observed in Au_6^-; its lifetime is owed to a planar structure and its excitation into an orbital outside the cluster plane, thus resulting in low de-excitation probability. Such an extraordinary long lifetime has not been found in other Au_n^- clusters.[141] Besides cluster geometries, long excited state lifetimes can be influenced by degree of solvatation[25,26] or oxidation.[79] However, general indicators that always apply have not been identified.

The calculations presented in the thesis are motivated by experiments conducted in the group of Prof. Dr. Gerd Ganteför at the University of Konstanz. They performed time-resolved photoelectron spectroscopic studies of ZnO and CdO nanoclusters in gas phase and discovered an unusual behavior - extraordinary long-lived excited states. However, the interpretation of the experiments and full understanding of this behavior is not possible without the aid of DFT calculations described in my thesis. As the result, not only new structures of ZnO and CdO clusters have been discovered, but it has been also possible to demonstrate that the extraordinary long-lived excited states are due to electron–hole pair localization combined with structural rigidity of the nanoclusters. In addition, an unprecedented "inverse quantum confinement effect" in ZnO and CdO clusters - the decrease of the band gap with decreasing cluster size has been discovered. For both oxides the highly symmetric alternant cage structures and large band gaps have been predicted, confirming their validity as CAM building blocks. Striking similarity between $(ZnO)_n^-$ and $(CdO)_n^-$ clusters leads to the idea of an alternant cage cluster assembled materials (ACCAMs) construction kit helpful in design of novel materials of unprecedented properties.

Finally, the DFT implementation developed in my thesis has been used to investigate mixed ZnO-TiO_2 based materials. Such materials, particularly in nanostructured form as nanoparticles, nanotubes and thin films, play an essential role in many fields of modern material science,[10,33,120] in particular as materials for dye-sensitized solar cells.[9,73,129,157] Despite widespread use, ZnO and TiO_2 based systems have some drawbacks. For TiO_2 it is a low electron mobility, and fast recombination of electrons and holes after excitation. For ZnO, the main drawback is its vulnerability to photo and chemical corrosion. Moreover for both ZnO and TiO_2 the maximum of light absorption is blue shifted compared to solar spectrum peak. Therefore, many efforts have been taken to develop new, more efficient materials by adjusting the structure of ZnO and TiO_2 by combining both materials or by combining them with other compounds. Recently, systems containing both ZnO and TiO_2 have been investigated by several authors. For example, Zhao et al.[162] synthesized Zn-doped TiO_2 nanoparticles with high photocatalytic activity. The ZnO has been found to be presented in the form of small clusters dispersed on the surface of anatase-like TiO_2 nanoparticles. Another studies on combined TiO_2–

ZnO materials have been conducted by Xu et al.,[155] who developed high-efficiency solid-state dye-sensitized solar cells with efficiency comparable to liquid-state solar cells.

In my thesis mixed ZnO-TiO_2 nanoclusters as well as ZnO clusters adsorbed on the anatase (101) surface have been investigated. Striking structural similarities between structures of mixed ZnO-TiO_2 and pure TiO_2 nanoclusters have been found, along with the "inverse quantum confinement effect". In case of ZnO nanoclusters adsorbed on the anatase surface a significant reduction of the band gap of the combined system has been shown. This suggest the way to tune electronic properties of TiO_2-based materials, in particular for solar cell applications, by deposition of ZnO nanoclusters on anatase-like nanostructures.

CHAPTER 2

Density Functional Theory

In this chapter an implementation of Kohn–Sham density functional theory with Gaussian type orbitals as basis functions that treats molecular and periodic systems of any dimensionality on an equal footing is presented. The key component of the implementation is a combination of density fitting/resolution of identity (DF) approximation and continuous fast multipole method (CFMM) applied for the electronic Coulomb term. This DF-CFMM scheme operates entirely in the direct space and partitions Coulomb interactions into far-field part evaluated using multipole expansions and near-field contribution calculated employing density fitting. The exchange-correlation term is evaluated using the hierarchical numerical integration scheme of Burow et al.[28] Computational efficiency and favourable asymptotic $O(N)$ scaling behaviour of the DF-CFMM scheme as well as of its extension to energy gradient is demonstrated for various molecular and periodic systems including three dimensional models presented in app. B.1. This chapter contains verbatim quotes from the related articles[88,89] published during my PhD, of which I am the first author.

2.1 General Theory

2.1.1 Basic Equations

The general scheme of presented GTO-based DFT implementation for periodic systems follows the standard procedures available in similar programs.[46,52,85] Here, only the most important equations are given for the sake of completeness.

The translational symmetry of solids leads to Bloch orbitals $\psi^{\mathbf{k}}_{p\sigma}$ and one-particle energies $\varepsilon^{\mathbf{k}}_{p\sigma}$ depending on the band index p, spin σ, and the wave vector $\mathbf{k}$ within the Brillouin zone (BZ), which is the unit cell of reciprocal space. The orbitals

$$\psi^{\mathbf{k}}_{p\sigma}(\mathbf{r}) = \frac{1}{\sqrt{N_{\mathrm{UC}}}} \sum_{\mathbf{L}} e^{i\mathbf{kL}} \sum_{\mu} C^{\mathbf{k}}_{\mu p\sigma} \mu_{\mathbf{L}}(\mathbf{r}) \tag{2.1}$$

are expanded in GTO basis functions $\mu(\mathbf{r} - \mathbf{R}_\mu - \mathbf{L}) \equiv \mu_{\mathbf{L}}(\mathbf{r})$ centred at atomic positions $\mathbf{R}_\mu$ in direct lattice cells $\mathbf{L}$ over all N_{UC} unit cells. The matrix of expansion coefficients $\mathbf{C}^{\mathbf{k}}_\sigma$ is determined by solving Kohn-Sham equations in GTO basis,

$$\mathbf{F}^{\mathbf{k}}_\sigma \mathbf{C}^{\mathbf{k}}_\sigma = \mathbf{S}^{\mathbf{k}} \mathbf{C}^{\mathbf{k}}_\sigma \varepsilon^{\mathbf{k}}_\sigma, \tag{2.2}$$

separately for each $\mathbf{k}$ in the BZ. The same equations hold for the molecular case, where only $\mathbf{L} = \mathbf{k} = \mathbf{0}$ is a valid choice and N_{UC} is one. Eq. 2.2 contains the reciprocal space Kohn-Sham (KS) and the overlap matrices $\mathbf{F}^{\mathbf{k}}_\sigma$ and $\mathbf{S}^{\mathbf{k}}$, respectively, obtained as Fourier transforms of real space matrices

$$F^{\mathbf{k}}_{\mu\nu\sigma} = \sum_{\mathbf{L}} e^{i\mathbf{k}^{\mathrm{T}}\mathbf{L}} F^{\mathbf{L}}_{\mu\nu\sigma} \tag{2.3}$$

$$S^{\mathbf{k}}_{\mu\nu} = \sum_{\mathbf{L}} e^{i\mathbf{k}^{\mathrm{T}}\mathbf{L}} S^{\mathbf{L}}_{\mu\nu}. \tag{2.4}$$

The elements $F^{\mathbf{L}}_{\mu\nu\sigma}$ contain three contributions: elements $T^{\mathbf{L}}_{\mu\nu}$ of the kinetic energy matrix, elements $J^{\mathbf{L}}_{\mu\nu}$ of the Coulomb matrix, and elements $X^{\mathbf{L}}_{\mu\nu\sigma}$ of the exchange-correlation matrix,

$$F^{\mathbf{L}}_{\mu\nu\sigma} = T^{\mathbf{L}}_{\mu\nu} + J^{\mathbf{L}}_{\mu\nu} + X^{\mathbf{L}}_{\mu\nu\sigma}. \tag{2.5}$$

The evaluation of $T^{\mathbf{L}}_{\mu\nu}$ is identical to the molecular case and $X^{\mathbf{L}}_{\mu\nu\sigma}$ are calculated using a hierarchical integration scheme[28] presented in sec. 2.2.2. The calculation of $J^{\mathbf{L}}_{\mu\nu}$ and $X^{\mathbf{L}}_{\mu\nu\sigma}$ requires the real space density matrix obtained by integration

$$D^{\mathbf{L}}_{\mu\nu\sigma} = \frac{1}{V_k} \int_{\mathrm{BZ}} D^{\mathbf{k}}_{\mu\nu\sigma} e^{i\mathbf{k}^{\mathrm{T}}\mathbf{L}} d\mathbf{k} \tag{2.6}$$

of the reciprocal space density matrix

$$D^{\mathbf{k}}_{\mu\nu\sigma} = \sum_{p} f^{\mathbf{k}}_{p\sigma} \left(C^{\mathbf{k}}_{\mu p\sigma} \right)^{*} C^{\mathbf{k}}_{\nu p\sigma} \tag{2.7}$$

over the BZ with volume V_k. The orbital coefficients $C^{\mathbf{k}}_{\mu p\sigma}$ are taken from an initial guess or from the previous solution of eq. 2.2. The occupation numbers $f^{\mathbf{k}}_{p\sigma}$ at zero temperature are either zero or one for occupied and virtual orbitals, respectively. The reciprocal space integral in eq. 2.6 is evaluated numerically on a finite grid of k-points.

Within a self-consistent-field (SCF) cycle, the calculation of all contributions to the KS and overlap matrices is first completed in direct space and then eq. 2.2 is solved in reciprocal space. The last step is accomplished within a loop over a grid of k-points, where the direct space matrices are transformed into the orthonormal orbital basis on a single k-point. In this way, a regular matrix eigenvalue problem is obtained in eq. 2.2, which is solved by diagonalization of the KS matrix. The elements $D^{\mathbf{k}}_{\mu\nu\sigma}$ in eq. 2.7 are formed from the eigenvectors $C^{\mathbf{k}}_{\mu p\sigma}$ of eq. 2.2 and are subsequently transformed on the fly to yield the direct space density matrix according to eq. 2.6. In each SCF cycle, the total energy per unit cell, E, is calculated as

$$E = \sum_{\mu\nu\mathbf{L}} \sum_{\sigma} D^{\mathbf{L}}_{\mu\nu\sigma} T^{\mathbf{L}}_{\mu\nu} + E_{\mathrm{XC}} + J, \tag{2.8}$$

where J and E_{XC} are the Coulomb and exchange-correlation (XC) energy contributions, calculated as described in secs. 2.2.1 and 2.2.2, respectively.

An important feature of the real space KS matrix elements $F^{\mathbf{L}}_{\mu\nu\sigma}$ is their exponential decay with increasing separation of the basis functions μ and ν. Combined with the direct space symmetry relation of the matrices $M = F$, T, J, X_σ, D_σ defined previously,

$$M^{-\mathbf{L}}_{\nu\mu} = M^{\mathbf{L}}_{\mu\nu}, \tag{2.9}$$

the exponential decay allows for a very efficient sparse storage of the real space matrices.[28] There is a further a reciprocal space symmetry relation

$$M^{-\mathbf{k}}_{\mu\nu} = \left(M^{\mathbf{k}}_{\mu\nu}\right)^*, \tag{2.10}$$

which shows that all direct space matrix elements must be real, if the BZ contains for each $\mathbf{k}$ the corresponding $-\mathbf{k}$ and real GTO basis functions are used.

Once the SCF calculation is converged, energy gradient may be computed. First energy derivatives $E^{A\alpha}$ with respect to displacement of nuclei A along the Cartesian component α are obtained by differentiation of eq. 2.8 and are given as[85]

$$E^{A\alpha} = \sum_{\sigma} \left(D^{\mathbf{L}}_{\mu\nu\sigma} T^{\mathbf{L}A\alpha}_{\mu\nu} - W^{\mathbf{L}}_{\mu\nu\sigma} S^{\mathbf{L}A\alpha}_{\mu\nu\sigma} \right) + E^{A\alpha}_{\mathrm{XC}} + J^{A\alpha}, \tag{2.11}$$

where $T^{\mathbf{L}A\alpha}_{\mu\nu}$ and $S^{\mathbf{L}A\alpha}_{\mu\nu\sigma}$ are first derivatives of the kinetic energy and overlap matrix elements, respectively. Their calculation is similar to the molecular case.[56,112,113] Elements $W^{\mathbf{L}}_{\mu\nu\sigma}$ of the real-space energy weighted density matrix are obtained by numerical integration over the first Brillouin zone as

$$W^{\mathbf{L}}_{\mu\nu\sigma} = \sum_{\mathbf{k}} w_{\mathbf{k}} e^{i\mathbf{k}^{\mathrm{T}}\mathbf{L}} W^{\mathbf{k}}_{\mu\nu\sigma} \text{ with } W^{\mathbf{k}}_{\mu\nu\sigma} = \sum_{p} f^{\mathbf{k}}_{p\sigma} \varepsilon^{\mathbf{k}}_{p\sigma} \left(C^{\mathbf{k}}_{\mu p\sigma} \right)^{*} C^{\mathbf{k}}_{\nu p\sigma}. \tag{2.12}$$

The Pulay force $-\sum_{\mu\nu\mathbf{L}} \sum \sigma W^{\mathbf{L}}_{\mu\nu\sigma} S^{\mathbf{L}A\alpha}_{\mu\nu\sigma}$ is related to basis set incompleteness.[113] Derivatives of Coulomb ($J^{A\alpha}$) and exchange-correlation ($E^{A\alpha}_{\mathrm{XC}}$) terms are calculated as described in sec. 2.3. Similarly to the energy case, efficient sparse storage of matices introduced in eq. 2.11 is achieved using symmetry relations 2.9 and 2.10.

All time-consuming steps of the DF-CFMM scheme have been parallelized for shared memory machines using the OpenMP application programming interface.[2]

2.1.2 Density Fitting Scheme

A full description of the method is given in ref. 29 and here only the basic summary is provided. The total crystal electron density ρ_{c} is a (infinite) sum of local densities $\rho_{\mathbf{L}}$ centred in cells translated by $\mathbf{L}$,

$$\rho_{\mathrm{c}} = \sum_{\mathbf{L}} \rho_{\mathbf{L}}, \tag{2.13}$$

with

$$\rho_{\mathbf{L}} = \sum_{\mu\nu\mathbf{L}'} \sum_{\sigma} D^{\mathbf{L}'}_{\mu\nu\sigma} \mu_{\mathbf{L}} \nu_{\mathbf{L}\mathbf{L}'}, \tag{2.14}$$

where the shorthand notation $\nu_{\mathbf{L}}(\mathbf{r} - \mathbf{L}') \equiv \nu_{\mathbf{L}\mathbf{L}'}$ is used and the subscript $\mathbf{0}$ is omitted for $\mathbf{L} = \mathbf{0}$. Atom-centred GTO auxiliary basis functions that are elements of vector $\boldsymbol{\alpha}$ are denoted as α.

The total crystal electron density ρ_{c} is approximated by auxiliary crystal electron density $\tilde{\rho}_{\mathrm{c}}$,

$$\rho_{\mathrm{c}} \approx \tilde{\rho}_{\mathrm{c}} = \sum_{\mathbf{L}} \tilde{\rho}_{\mathbf{L}}, \tag{2.15}$$

composed of unit cell auxiliary densities

$$\tilde{\rho}_{\mathbf{L}} = \sum_{\alpha} \mathbf{c}^T \boldsymbol{\alpha}_{\mathbf{L}}. \tag{2.16}$$

The vector of expansion coefficients $\mathbf{c}$ is independent of the lattice vectors $\mathbf{L}$, since it is identical in every unit cell. It is determined by minimizing the Coulomb repulsion D of the residual density $\delta\rho = \rho_c - \tilde{\rho}_c$

$$\begin{aligned} D &= \iint \delta\rho\left(\mathbf{r}\right) \frac{1}{\mid \mathbf{r} - \mathbf{r}' \mid} \sum_{\mathbf{L}} \delta\rho_{\mathbf{L}}\left(\mathbf{r}'\right)\, d\mathbf{r}\, d\mathbf{r}' \\ &= \left(\delta\rho \mid \delta\rho_{\mathbf{L}}\right) = \left(\rho_c - \tilde{\rho}_c \mid \rho_{\mathbf{L}} - \tilde{\rho}_{\mathbf{L}}\right). \end{aligned} \tag{2.17}$$

Unless explicitly stated, in eq. 2.17 and throughout this chapter a direct space lattice sum over lattice vectors $\mathbf{L}$ is understood on the right hand side of Coulomb integrals.

In periodic systems D is finite only if $\delta\rho$ is chargeless, i.e.,

$$\int \delta\rho\left(\mathbf{r}\right) d\mathbf{r} = 0 \quad \Rightarrow \quad \int \tilde{\rho}\left(\mathbf{r}\right) d\mathbf{r} = N_{\mathrm{el}}. \tag{2.18}$$

Thus, the charge of $\tilde{\rho}$ is naturally constrained to the number of electrons, N_{el}. In order to explicitly enforce this condition $\tilde{\rho}$ is decomposed into charged and chargeless components, $\tilde{\rho}_{||}$ and $\tilde{\rho}_{\perp}$, respectively,

$$\tilde{\rho} = \tilde{\rho}_{||} + \tilde{\rho}_{\perp} = \mathbf{c}_{||}^T \boldsymbol{\alpha} + \mathbf{c}_{\perp}^T \boldsymbol{\alpha} \tag{2.19}$$

with

$$\int \tilde{\rho}_{||}\left(\mathbf{r}\right) d\mathbf{r} = N_{\mathrm{el}} \quad \text{and} \quad \int \tilde{\rho}_{\perp}\left(\mathbf{r}\right) d\mathbf{r} = 0. \tag{2.20}$$

The vectors of expansion coefficients $\mathbf{c}_{||}$ and $\mathbf{c}_{\perp}$ are orthogonal to each other and can be expressed with help of projection matrices

$$\mathbf{P}_{||} = \mathbf{n}\mathbf{n}^T \quad \text{and} \quad \mathbf{P}_{\perp} = \mathbf{1} - \mathbf{n}\mathbf{n}^T \tag{2.21}$$

as

$$\mathbf{c}_{||} = \mathbf{P}_{||}\mathbf{c} \quad \text{and} \quad \mathbf{c}_{\perp} = \mathbf{P}_{\perp}\mathbf{c}. \tag{2.22}$$

The vector $\mathbf{n}$ in eq. 2.21 is a normalized charge vector of the auxiliary basis with elements

$$n_\alpha = \frac{1}{|\mathbf{q}|} q_\alpha \quad \text{with} \quad \mathbf{q} = \left(q_1, q_2, \ldots\right) \quad \text{and} \quad q_\alpha = \int \alpha\left(\mathbf{r}\right) d\mathbf{r}. \tag{2.23}$$

The same projection matrices are used to define the vectors of charged and chargeless auxiliary basis functions $\boldsymbol{\alpha}_{\|}$ and $\boldsymbol{\alpha}_{\perp}$, respectively, as $\boldsymbol{\alpha}_{\|} = \mathbf{P}_{\|}\boldsymbol{\alpha}$ and $\boldsymbol{\alpha}_{\perp} = \mathbf{P}_{\perp}\boldsymbol{\alpha}$. Due to the mentioned charge constraint of $\tilde{\rho}$, the expansion coefficients $\mathbf{c}_{\|}$ of the charged component $\tilde{\rho}_{\|}$ take the form

$$\mathbf{c}_{\|} = \frac{N_{\mathrm{el}}}{|\mathbf{q}|}\mathbf{n}. \tag{2.24}$$

The complementary chargeless part $\tilde{\rho}_{\perp}$ is determined by minimization of D (eq. 2.17) with respect to all elements of $\mathbf{c}_{\perp}$. This leads to a system of linear equations

$$\left(\mathbf{V}_{\perp} + \mathbf{P}_{\|}\right)\mathbf{c}_{\perp} = \boldsymbol{\xi}_{\perp}, \tag{2.25}$$

where $\mathbf{V}_{\perp}$ is the projected Coulomb metric matrix

$$\mathbf{V}_{\perp} = \mathbf{P}_{\perp}\mathbf{V}\mathbf{P}_{\perp} = \left(\boldsymbol{\alpha}_{\perp} \mid \boldsymbol{\alpha}_{\perp\mathbf{L}}^{T}\right) \tag{2.26}$$

and vector $\boldsymbol{\xi}_{\perp}$ is given by

$$\boldsymbol{\xi}_{\perp} = \left(\boldsymbol{\alpha}_{\perp} \mid \rho_{\mathbf{L}} - \tilde{\rho}_{\|\mathbf{L}}\right). \tag{2.27}$$

An important property of this DF scheme is that all lattice sums in eqs. 2.25–2.27 are convergent since they employ exclusively chargeless quantities. Contrary to other approaches for DF in extended systems,[48,67] this formulation does not use the nuclear charge distribution to obtain such convergent lattice sums.

The final set of expansion coefficients of the auxiliary density is obtained as $\mathbf{c} = \mathbf{c}_{\|} + \mathbf{c}_{\perp}$.

2.2 Energy Calculation

2.2.1 Coulomb Term: DF-Accelerated CFMM

The elements $J_{\mu\nu}^{\mathbf{L}'}$ of the real space Coulomb matrix are calculated using the auxiliary density as

$$J_{\mu\nu}^{\mathbf{L}'} = \left(\mu\nu_{\mathbf{L}'} \mid \tilde{\rho}_{\mathbf{L}} - \rho_{\mathrm{n}\mathbf{L}}\right), \tag{2.28}$$

where ρ_{n} denotes the unit cell nuclear charge distribution. They are used to calculate the total Coulomb energy including the nuclear contribution as

$$J = \sum_{\mu\nu\mathbf{L}'} D_{\mu\nu}^{\mathbf{L}'} J_{\mu\nu}^{\mathbf{L}'} - \frac{1}{2}\left(\tilde{\rho} + \rho_{\mathrm{n}} \mid \tilde{\rho}_{\mathbf{L}} - \rho_{\mathrm{n}\mathbf{L}}\right). \tag{2.29}$$

The efficiency of the implementation arises from use of continuous fast multipole method (CFMM)[83–86,149] for evaluation of Coulomb lattice sums appearing in eqs. 2.27 – 2.29. This results in DF-accelerated CFMM (DF-CFMM) scheme, with all calculations performed entirely in the direct space. This section provides basic definitions and description of the algorithm, in particular of the octree-based scheme used to store and manipulate multipole expansions.

2.2.1.1 Partitioning of Coulomb Lattice Sums

The definition of well-separated charge distributions plays the central role in the DF-CFMM. Two charge distributions centred at $\mathbf{P}$ and $\mathbf{Q}$ with extents (radii) r_P and r_Q, respectively, are well-separated if the distance between the centres is larger than the sum of their extents, i.e.,

$$|\mathbf{P} - \mathbf{Q}| \geq r_P + r_Q. \tag{2.30}$$

The extents in eq. 2.30 ensure that for well-separated distributions the error of the Coulomb interaction introduced by the multipole approximation is smaller than a given threshold ε. Definitions for the extents of charge distributions are given in ref. 122.

The Coulomb lattice sums in eqs. 2.27 – 2.29 are partitioned into the crystal near-field (CNF) and far-field (CFF) contributions as depicted in fig. 2.1. In a full lattice sum of the form $(\rho_1 \mid \rho_{2\mathbf{L}})$ the distribution ρ_1 in the central unit cell ($\mathbf{L} = \mathbf{0}$) interacts with an infinite number of distributions $\rho_{2\mathbf{L}}$, i.e., ρ_2 translated by all possible $\mathbf{L}$. The distributions ρ_1 and ρ_2 can contain point charges (nuclei), as well as continuous charge distributions (shell pairs $\mu\nu_{\mathbf{L}}$ or/and auxiliary basis functions α).

The CNF contribution consists of ρ_1 interacting with $\rho_{2\mathbf{L}}$ for a finite number of $\mathbf{L}$ corresponding to the neighbouring unit cells. The remaining part of the lattice sum defines the CFF, i.e.,

$$\sum_{\mathbf{L}} (\rho_1 \mid \rho_{2\mathbf{L}}) = \sum_{\mathbf{L} \in \mathrm{CNF}} (\rho_1 \mid \rho_{2\mathbf{L}}) + \sum_{\mathbf{L} \in \mathrm{CFF}} (\rho_1 \mid \rho_{2\mathbf{L}}) \,. \tag{2.31}$$

A lattice vector $\mathbf{L}$ belongs to the CFF if it fulfils two conditions: (i) all charge

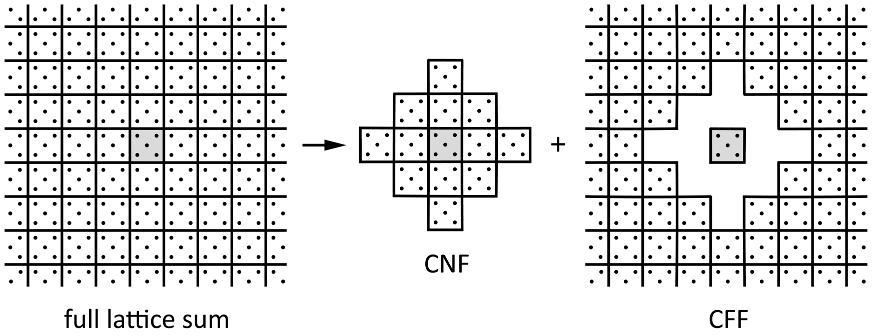

Figure 2.1: Partitioning of a Coulomb lattice sum into the CNF and CFF contributions. The central unit cell with $\mathbf{L} = \mathbf{0}$ is marked in grey.

distributions forming ρ_1 are well separated from those of $\rho_{2\mathbf{L}}$, and (ii) $|\mathbf{L}| \geq ws \times (r_1^{max} + r_2^{max})$, where r_1^{max} and r_2^{max} are maximum distances between the unit cell centre and all charge centres comprising ρ_1 and ρ_2, respectively, and ws is the well-separateness criterion. Note, that this definition of ws is different than the one used by other authors, e.g., in refs. 84 and 151.

The infinite lattice sums of the CFF part for systems of 1D, 2D and 3D periodicity with arbitrary lattice vectors are evaluated using multipole expansions and recurrence relations derived by Kudin and Scuseria[86] for calculation of the lattice sum $\mathbf{S}$ of so called "external to local" translation operators. $\mathbf{S}$ is calculated only once per SCF run and stored, since it depends only on the size and shape of the unit cell. This contribution to Coulomb interaction is obtained in negligible time. The evaluation of the CNF part of the Coulomb lattice sum is the bottleneck of calculations for periodic systems. This contribution is evaluated as described in sec. 2.2.1.2

2.2.1.2 Crystal Near-Field Contribution

The CNF contribution of the lattice sum $(\rho_1 \mid \rho_{2\mathbf{L}})$ is evaluated employing CFMM that combines high computational efficiency and favourable scaling approaching $O(N)$. The key feature of the CFMM is an octree-based hierarchical spatial decomposition of the charge distributions ρ_1 and ρ_2. This allows partitioning of Coulomb interactions between the two distributions into far-field (FF) and near-field (NF) contributions. The NF part is evaluated by means of direct integration. The FF part comprises the majority of interactions and is calculated very efficiently using a hierarchy of multipole expansions. The CFMM implementation in RIPER closely follows the algorithm described in refs. 83–85, 149 and 151. The main differences are: (i) the NF contribution to the Coulomb matrix elements is evaluated employing density fitting, and (ii) octree construction and the spatial decomposition are applied directly to ρ_1 and $\rho_{2\mathbf{L}}$ only for $\mathbf{L} = 0$. The interactions between ρ_1 and $\rho_{2\mathbf{L}}$ for the remaining $\mathbf{L} \in \text{CNF}$ are calculated using replicas of the octree.

The construction of the octree is based on the fractional tiers scheme of White and Head-Gordon.[150] It achieves an optimum balance between the NF and FF work by allowing for an arbitrary number of the lowest level boxes. In contrast, standard boxing schemes restrict the number of lowest level boxes to be a power of eight. In short, a cubic parent box enclosing all distribution centres of ρ_1 and ρ_2 is constructed that is large enough to yield a predefined number n_{targ} of distribution centres per lowest level box. The parent box is successively subdivided in half along all Cartesian axes yielding the octree. In the next step all charge distributions comprising ρ_1 and ρ_2 are sorted into boxes. This is achieved by assigning the centre of each distribution (nuclear point charge, auxiliary basis function or shell pair) of ρ_1 and ρ_2 to the smallest box with the edge length $L_i \geq 2r_i/(ws - 1)$, where r_i is the distribution extent. This condition ensures that on each tree level the distributions from well-separated boxes do not overlap. Nuclear point charges are sorted into the lowest-level boxes by their coordinates.

The CNF contribution of the lattice sum $(\rho_1 \mid \rho_{2\mathbf{L}})$ is calculated using the following scheme, depicted schematically in fig. 2.2. The necessary definitions of multipole and Taylor expansions as well as translation operators are introduced in app. A and derived in ref. 149.

Step 1: Formation and Translation of Multipole Expansions

This step does not involve any periodic images of ρ_2 and is identical for molecular and periodic systems. For each occupied octree box at all levels multipole expansions about the centre of the box are formed for charge distributions comprising ρ_1 and ρ_2 that belong to the given box. These multipole expansions are calculated using the

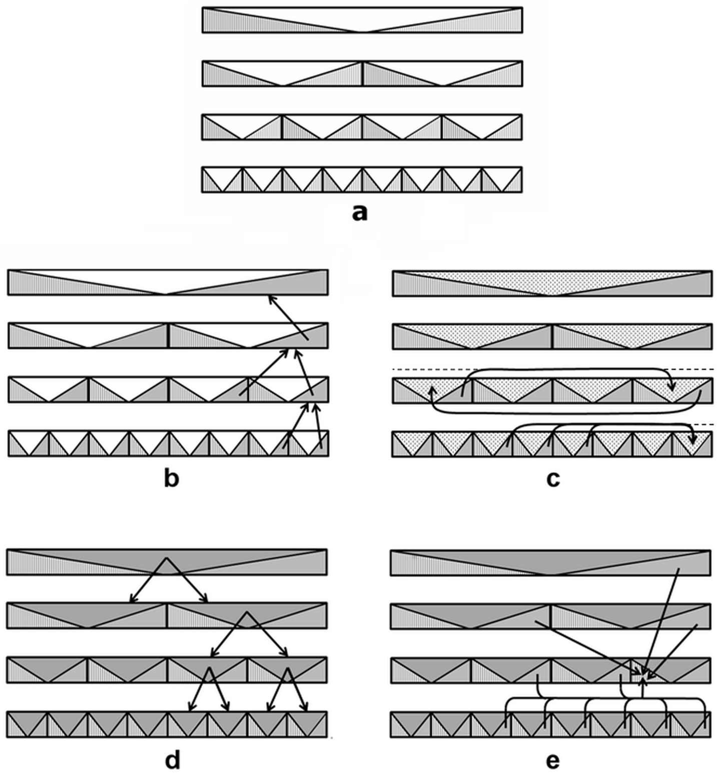

Figure 2.2: 1D scheme representation of DF-CFMM with $ws = 3$ in the CNF part of the lattice sum $(\rho_1 \mid \rho_{2\mathbf{L}})$: a) formation of partial multipole expansions of ρ_1 (left lower triangle in each box) and ρ_2 (right lower triangle), b) upwards translation and summation of partial multipole expansions of ρ_2, c) formation of Taylor expansions (upper triangle) from partial multipole expansions in well-separated boxes whose parents are not well-separated; dashed lines represent contributions from periodic replicas of the octree, d) downward shift and summation of Taylor expansions, e) calculation of the NF contribution between non-well-separated boxes at all levels and between levels.

method described in ref. 122. The expansions are stored separately for ρ_1 and ρ_2 (see fig. 2.2a). Multipole expansions of ρ_2 are translated upwards applying the "external to external" translation operator A and accumulated starting from the lowest level of the octree (fig. 2.2b). After this step each box contains partial multipole expansion of charge distributions of ρ_2 contained in the box itself and in its child boxes.

Step 2: Formation and Translation of Taylor Expansions

In this step the partial multipole expansion of ρ_2 about the centre of a box $i_{\mathbf{L}}$ (*i.e.,* box i shifted by a lattice vector $\mathbf{L} \in$ CNF) is transformed into the Taylor expansion about the centre of box j. This transformation uses the "external to local" operator B and is performed only for pairs of boxes at the same level of the octree that are well-separated while their parents are not (cf. fig. 2.2c). Two boxes $i_{\mathbf{L}}$ and j with edge lengths L_i and L_j, respectively, are called well-separated if the distance d_{ij} between their centres satisfies the condition

$$d_{ij} \geq ws \times \frac{(L_i + L_j)}{2}. \tag{2.32}$$

Since the partial multipole expansions along the octree are formed only for $\rho_{2\mathbf{L}}$ with $\mathbf{L} = \mathbf{0}$ (Step 1), this procedure formally involves replica of the octree shifted by $\mathbf{L} \in$ CNF. Using the replica allows for a significant speedup of this "external to local" transformation step by first calculating the sum of operators B for all $\mathbf{L} \in$ CNF that fulfill the condition given by eq. 2.32. This sum is then applied to transform partial multipole expansion of ρ_2 about the centre of box i into the Taylor expansion about the centre of box j for all well-separated $i_{\mathbf{L}}$ in only one step. This is the main difference to the implementation of Kudin et al.[83,84,86] who sort charge distributions for all $\mathbf{L} \in$ CNF into one bigger octree.

The local Taylor expansions are passed down the tree using the operator C. This pass starts at the highest level and translates Taylor expansions of each parent box to the centres of the child boxes. The expansions within child boxes are summed up and the procedure is repeated until the lowest level of the octree is reached (fig. 2.2d).

Step 3: Far-field Contribution

After steps 1 and 2 each box within the octree contains partial Taylor expansions of $\rho_{2\mathbf{L}}$ from all well-separated boxes $i_{\mathbf{L}}$ for $\mathbf{L} \in \mathrm{CNF}$. These expansions are combined with partial multipole expansions of ρ_1 yielding the FF portion of the CNF contribution to lattice sum $(\rho_1 \mid \rho_{2\mathbf{L}})$.

Step 4: Near-field Contribution

In this step the remaining interactions between non-well-separated boxes and within boxes are evaluated by direct integration at all octree levels. This is the most time-consuming step of the algorithm. Note, that the NF part includes interactions between the boxes at different levels, as depicted in fig. 2.2e. The resulting NF contribution is combined with the FF part obtained in step 3 yielding the CNF part of the lattice sum $(\rho_1 \mid \rho_{2\mathbf{L}})$.

2.2.2 Exchange-Correlation Term

In this section an evaluation scheme of E_{XC} term in eq. 2.8 is described. During the course of my work the initial algorithm of Burow et al.[28] has been extended to meta-GGA case. For simplicity, only the closed-shell formalism is presented here. The total crystal electron density ρ_{c} (see eqs. 2.13 and 2.14) is therefore rewritten as

$$\rho_{\mathrm{c}} = \sum_{\mathbf{L}} \rho_{\mathbf{L}}, \text{ with } \rho_{\mathbf{L}} = \sum_{\mu\nu\mathbf{L}'} D_{\mu\nu}^{\mathbf{L}'-\mathbf{L}} \mu_{\mathbf{L}} \nu_{\mathbf{L}\mathbf{L}'}. \tag{2.33}$$

The XC energy is defined as an integral over the unit cell (UC),

$$E_{\mathrm{XC}} = \int_{\mathrm{UC}} f\left(\rho_{\mathrm{c}}, \gamma, \tau\right) d\mathbf{r} \tag{2.34}$$

with the exchange-correlation function[20,34,57,63,70,90,106,107,109,130,140]

$$f = f\left(\rho_{\mathrm{c}}, \gamma, \tau\right), \tag{2.35}$$

the gradient invariant

$$\gamma = |\nabla \rho_{\mathrm{c}}|^2 \tag{2.36}$$

and kinetic energy density

$$\tau = \frac{1}{2} \sum_{\mu \mathbf{L} \nu \mathbf{L}'} D_{\mu\nu}^{\mathbf{L}'-\mathbf{L}} \nabla \mu_{\mathbf{L}} \nabla \nu_{\mathbf{L}\mathbf{L}'}. \tag{2.37}$$

In practice the integral given by eq. 2.34 is too complex to be evaluated analytically. Therefore, numerical integration using a finite set of grid points $\mathbf{r}_m$ with weights w_m is performed, i.e., eq. 2.34 is replaced by

$$E_{\mathrm{XC}} = \sum_m w_m f \left(\rho_{\mathrm{c}}^m, \gamma^m, \tau^m \right) \tag{2.38}$$

where ρ_{c}^m, γ^m and τ^m are values of ρ_{c}, γ and τ at a grid point $\mathbf{r}_m$. The presented implementation uses multi-centre grids composed of atom-centred grids and restricted to atoms of one UC in the case of periodic systems.[28] Calculation of the weights w_m uses the Scuseria scheme.[126] For molecular systems the Becke renormalization[21] scheme has also been implemented. Elements $X_{\mu\nu}^{\mathbf{L}}$ of the real space XC matrix are calculated as

$$\begin{aligned} X_{\mu\nu}^{\mathbf{L}} = \sum_m \sum_{\mathbf{L}'} w_m \Bigg[& \left.\frac{\partial f}{\partial \rho_c}\right|_{\mathbf{r}_m} \left(\mu_{\mathbf{L}'}^m \nu_{\mathbf{L}'\mathbf{L}}^m \right) \\ & + 2 \sum_{\alpha = x,y,z} \left.\frac{\partial f}{\partial \gamma} \rho_c^\alpha \right|_{\mathbf{r}_m} \left(\mu_{\mathbf{L}'}^m \nu_{\mathbf{L}'\mathbf{L}}^{m\alpha} + \mu_{\mathbf{L}'}^{m\alpha} \nu_{\mathbf{L}'\mathbf{L}}^m \right) \\ & + \frac{1}{2} \sum_{\alpha = x,y,z} \left.\frac{\partial f}{\partial \tau}\right|_{\mathbf{r}_m} \left(\mu_{\mathbf{L}'}^{m\alpha} \nu_{\mathbf{L}'\mathbf{L}}^{m\alpha} \right) \Bigg] \end{aligned} \tag{2.39}$$

where superscript α denotes derivatives with respect to the corresponding Cartesian displacement component. Note, that ρ_{c}^α are simply elements of the density gradient $\nabla \rho_{\mathrm{c}}$.

The XC energy, and elements $X_{\mu\nu}^{\mathbf{L}}$ are calculated using the integration scheme developed by Burow et al.[28] The method shows an $O(N)$ scaling behaviour achieved by a hierarchical spatial grouping of basis functions and grid points employing an octree. This octree is constructed as described in section 2.2.1.2. Subsequently, all grid points and basis functions are sorted into the octree. Grid points are assigned to boxes simply by their coordinates. Assignment of basis functions is based on their extents.[28] Using the notation introduced in ref. 28,

$$F^m = w_m \left.\frac{\partial f}{\partial \rho_c}\right|_{\mathbf{r}_m} \tag{2.40}$$

$$\left(F^m_x, F^m_y, F^m_z\right) = 2w_m \left.\frac{\partial f}{\partial \gamma}\nabla\rho_c\right|_{\mathbf{r}_m} \tag{2.41}$$

$$F^m_\tau = \frac{1}{2}w_m \left.\frac{\partial f}{\partial \tau}\right|_{\mathbf{r}_m} \tag{2.42}$$

and

$$z^m_{\mathbf{L}\mu} = \frac{1}{2}F^m\mu^m_{\mathbf{L}} + \sum_\alpha F^m_\alpha \mu^{m\alpha}_{\mathbf{L}} \quad \text{and} \quad z^{m\alpha}_{\tau\mathbf{L}\mu} = \frac{1}{2}F^m_\tau \mu^{m\alpha}_{\mathbf{L}}, \tag{2.43}$$

eq. 2.39 can be rewritten as

$$X^{\mathbf{L}}_{\mu\nu} = \sum_m \sum_{\mathbf{L}'} \left(z^m_{\mathbf{L}'\mu}\nu^m_{\mathbf{L}'\mathbf{L}} + \mu^m_{\mathbf{L}'} z^m_{\mathbf{L}'\nu} + \sum_\alpha \left(z^{m\alpha}_{\tau\mathbf{L}'\mu}\nu^{m\alpha}_{\mathbf{L}'\mathbf{L}} + \mu^{m\alpha}_{\mathbf{L}'\mathbf{L}} z^{m\alpha}_{\tau\mathbf{L}'\nu} \right) \right). \tag{2.44}$$

This equation is similar to that given by Burow et al.[28] with an additional term related to meta-GGA functional. Calculation of the XC energy using eq. 2.38 and terms defined in eqs. 2.40 – 2.42 requires values of ρ_c, γ and τ on grid points. They are very efficiently calculated using optimized matrix-matrix multiplication subroutines and intermediate matrices $\mathbf{B}^p$ and $\mathbf{B}^{p(1)}$, with dimensions $M_p \times K_p$ and $3 \times M_p \times K_p$, respectively, where M_p is the number of grid points and K_p is the number of basis functions assigned to box p. The elements of $\mathbf{B}^p$ and $\mathbf{B}^{p(1)}$ are defined as

$$B^p_{\mu\mathbf{L}m} = \sum_{\nu\mathbf{L}'} D^{\mathbf{L}'-\mathbf{L}}_{\mu\nu}\nu^m_{\mathbf{L}'\mathbf{L}} \quad \text{and} \quad B^{p(1)}_{\mu\mathbf{L}m\alpha} = \sum_{\nu\mathbf{L}'} D^{\mathbf{L}'-\mathbf{L}}_{\mu\nu}\nu^{m\alpha}_{\mathbf{L}'\mathbf{L}} \tag{2.45}$$

where $\mu^m_{\mathbf{L}\mathbf{L}'}$ and $\mu^{m\alpha}_{\mathbf{L}\mathbf{L}'}$ are values of all contributing basis functions and their derivatives, respectively, on a grid point m. The values of basis functions on the grid points in box p are stored in a $M_p \times K_p$ matrix $\boldsymbol{\xi}$. Similarly, first derivatives of basis functions on grid points in the box p are stored in $\boldsymbol{\xi}^p$. The values of ρ_c, ρ^α_c and τ on each grid point m are calculated accumulating contributions from boxes as

$$\rho^m_c = \sum_p \text{row}_m\left[\mathbf{B}^p\right] \times \text{row}_m\left[\xi^p\right]^{\mathbf{T}} \tag{2.46}$$

$$\rho^{m\alpha}_c = \sum_p \text{row}_m\left[\mathbf{B}^p\right] \times \text{row}_m\left[\xi^{p(1)}\right]^{\mathbf{T}} \tag{2.47}$$

$$\tau_c^m = \sum_p \mathrm{row}_m \left[\mathbf{B}^{p(1)}\right] \times \mathrm{row}_m \left[\xi^{p(1)}\right]^{\mathbf{T}} \tag{2.48}$$

with $\mathrm{row}_m\,[\mathbf{M}]$ denoting the m-th row of $\mathbf{M}$. In practice, operations in eqs. 2.46 – 2.48 are performed using optimized matrix-matrix multiplication subroutines. Finally, the total energy is evaluated according to eq. 2.38.

2.3 Energy Gradient

2.3.1 Coulomb Term

First derivatives of the Coulomb part of energy gradient $J^{A\alpha}$ with respect to the displacement of the nuclei A are obtained by differentiation of eq. 2.29

$$J^{A\alpha} = \left(\rho_1 \mid \rho_{2\mathbf{L}}^{A\alpha}\right) + \left(\rho_1^{A\alpha} \mid \rho_{2\mathbf{L}}\right), \tag{2.49}$$

where

$$\rho_1 = \rho - \frac{1}{2}\left(\tilde{\rho} + \rho_{\mathrm{n}}\right) \text{ and } \rho_{2\mathbf{L}} = \tilde{\rho}_{\mathbf{L}} - \rho_{\mathbf{L}}. \tag{2.50}$$

The CFF contribution to the gradient term introduced in eq. 2.49 is evaluated in negligible time using the operator $\mathbf{S}$ (cf. sec. 2.2.1.1 and ref. 86)

The CNF part $J_{\mathrm{CNF}}^{A\alpha}$ derived from eqs. 2.49 and 2.50 may be written as[89]

$$\begin{aligned} J_{\mathrm{CNF}}^{A\alpha} = & \left(\rho^{A\alpha} \mid \sum_{\mathbf{L}\in\mathrm{CNF}} \left(\tilde{\rho}_{\mathbf{L}} - \rho_{\mathrm{n}\mathbf{L}}\right)\right) + \\ & \left(\tilde{\rho}^{A\alpha} \mid \sum_{\mathbf{L}\in\mathrm{CNF}} \left(\rho_{\mathbf{L}} - \rho_{\mathrm{n}\mathbf{L}}\right)\right) + \left(\rho_{\mathrm{n}}^{A\alpha} \mid \sum_{\mathbf{L}\in\mathrm{CNF}} \left(\rho_{\mathrm{n}\mathbf{L}} - \rho_{\mathbf{L}}\right)\right) \end{aligned} \tag{2.51}$$

The above terms are calculated using the CFMM scheme described in sec. 2.2.1.2

2.3.2 Exchange-Correlation Term

First derivatives of E_{XC} with respect to the displacement of the nuclei A, obtained by differentiation of eq. 2.38, are given as

$$\nabla_A E_{\mathrm{XC}} = \sum_m \left(w_m \nabla_A f\left(\rho_c^m, \gamma^m, \tau^m\right) + f\left(\rho_c^m, \gamma^m, \tau^m\right) \nabla_A w_m\right). \tag{2.52}$$

The first term in eq. 2.52 can be transformed applying the chain rule to differentiate the function f.[69,112] For the gradient component $E_{\mathrm{XC}}^{A\alpha}$ this yields

$$E_{\mathrm{XC}}^{A\alpha} = -2\sum_{m}\sum_{\mu_A\mathbf{L}}\sum_{\nu_A\mathbf{L}'}\left[\left.\frac{\partial f}{\partial \rho_c}\right|_{\mathbf{r}_m} \mu_{\mathbf{L}}^{m\alpha}\nu_{\mathbf{LL}'}^{m} + 2\sum_{\beta=x,y,z}\left.\frac{\partial f}{\partial \gamma}\,\rho_c^{\beta}\right|_{\mathbf{r}_m}\left(\mu_{\mathbf{L}}^{m\alpha\beta}\nu_{\mathbf{LL}'}^{m} + \mu_{\mathbf{L}}^{m\alpha}\nu_{\mathbf{LL}'}^{m\beta}\right)\right.$$
$$\left. +\frac{1}{2}\sum_{\beta=x,y,z}\left.\frac{\partial f}{\partial \tau}\right|_{\mathbf{r}_m}\mu_{\mathbf{L}}^{m\alpha\beta}\nu_{\mathbf{LL}'}^{m\beta}\right], \tag{2.53}$$

where μ_A denotes restricted summation over basis functions μ centred at the atom A. Using $\mathbf{B}^{p}$ and $\mathbf{B}^{p(1)}$ (see eq. 2.45), as well as the intermediate quantities given by eqs. 2.40 – 2.42, the exchange-correlation energy gradients are finally evaluated as

$$E_{\mathrm{XC}}^{A\alpha} = -2\sum_{m}\sum_{\mu_A\mathbf{L}}\sum_{p}\left[F^{m}B^{p}_{\mu_{\mathbf{L}}m}\mu_{\mathbf{L}}^{m\alpha} + \sum_{\beta=x,y,z}F_{\beta}^{m}\left(B^{p}_{\mu_{\mathbf{L}}m}\mu_{\mathbf{L}}^{m\alpha\beta} + B^{p(1)}_{\mu_{\mathbf{L}}m}\mu_{\mathbf{L}}^{m\alpha}\right)\right.$$
$$\left. +\frac{1}{2}\sum_{\beta=x,y,z}F_{\tau}^{m}B^{p(1)}_{\mu_{\mathbf{L}}m\beta}\mu_{\mathbf{L}}^{m\alpha\beta}\right]. \tag{2.54}$$

Again $\mathbf{B}^{p}$ and $\mathbf{B}^{p(1)}$ are used for efficient calculations on grid points using optimized matrix-matrix multiplication subroutines.[3]

The second term in eq. 2.52 is usually neglected since its calculation is computationally very demanding and does not lead to a significant accuracy improvement.[15,131] Therefore my work has been focused on efficient implementation of the first contribution to $E_{\mathrm{XC}}^{A\alpha}$ only. For the sake of completeness, the second term has been added later. Moreover, energy derivatives with respect to cell parameters have been implemented.

2.4 Implementation Details

The methodology described in this chapter has been implemented within the TURBOMOLE[1,5] program package. In order to save computational time, several quantities are precalculated and stored before entering the main SCF loop (i.e., iterative building of the KS matrix and solution of eq. 2.2). The most important is the list of significant basis function products $\mu\nu_{\mathbf{L}}$ which along with the symmetry relation given by eq. 2.9 allow for efficient sparse storage of all matrices in eq. 2.5. This is because the elements of these matrices have significant contribution only for non-vanishing $\mu\nu_{\mathbf{L}}$. The list is created based on the overlap criterion neglecting angular parts of the basis functions. Due to the exponential decay of $\mu\nu_{\mathbf{L}}$ with increasing separation between the centres of μ and $\nu_{\mathbf{L}}$ the length of this list shows asymptotic $O(N)$ scaling. For local exchange-correlation density functional approximations, the real space density matrix elements, eq. 2.6, may also be stored only for the significant $\mu\nu_{\mathbf{L}}$ products.

The lattice sums in eqs. 2.27 – 2.29 involve combinations of different types of charge distributions. It is efficient and yet simple to use the same common set of lattice vectors for partitioning all lattice sums into CNF and CFF portions (cf. eq. 2.31). Similarly, the products $\mu\nu_{\mathbf{L}}$, auxiliary basis functions α and nuclear point charges are all sorted into one common octree. The direct space elements $S^{\mathbf{L}}_{\mu\nu}$ and $T^{\mathbf{L}}_{\mu\nu}$ of the overlap and kinetic energy matrices, respectively, as well as the combined Coulomb metric matrix $\mathbf{V} = \mathbf{V}_\perp + \mathbf{P}_\parallel$ along with its Cholesky factorization needed for the solution of eq. 2.25 are evaluated and stored prior to the main SCF loop. The procedure used to calculate $\mathbf{V}$ is the same as used in ref. 29. Sparse matrix storage is used for all direct space matrices in eq. 2.5.

The procedures used within the main SCF loop are analogous to other implementations.[46,85] The main difference is the application of DF-CFMM for the evaluation of the Coulomb matrix elements $J^{\mathbf{L}}_{\mu\nu}$ and the Coulomb energy J. The procedure implemented consists of the following steps

- Calculation of the vector $\boldsymbol{\xi}_\perp$, eq. 2.27. First, the vector $\boldsymbol{\xi} = \big(\boldsymbol{\alpha} \mid \rho_{\mathbf{L}} - \tilde{\rho}_{\parallel\mathbf{L}}\big)$ is calculated using CFMM. $\boldsymbol{\xi}_\perp$ is obtained applying charge projection $\boldsymbol{\xi}_\perp = \mathbf{P}_\perp \boldsymbol{\xi}$ with the projection matrix $\mathbf{P}_\perp$ given in eq. 2.21.

- Solution of eq. 2.25 for the chargeless component $\mathbf{c}_\perp$ of the auxiliary density using precalculated Cholesky factorization of $\mathbf{V}_\perp + \mathbf{P}_\parallel$.

- Assembly of the final auxiliary density $\tilde{\rho}$ according to eqs. 2.19 and 2.24.

- Calculation of the Coulomb matrix elements $J^{\mathbf{L}}_{\mu\nu}$ according to eq. 2.28 using

CFMM.

- Calculation of the total Coulomb energy J. The second term in eq. 2.29 is evaluated using CFMM. The CNF part of this term is simplified as discussed in ref. 29.

The integral in eq. 2.6 is evaluated approximately on grids of sampling points $\mathbf{k}_\alpha$ with weights ω_α. Uniform grids centred at the Γ-point with N_α subdivisions along each reciprocal vector α are used. This is similar to the method proposed by Monkhorst and Pack.[100]. To reduce the computational cost, time-reversal symmetry between $\mathbf{k}$ and $-\mathbf{k}$ points is used. The weights ω_α for each point are set to be equal, with exception of the Γ-point, for which the halved value is set (due to lack of symmetric counterpart). Weights of all k-points add up to 1. Therefore eq. 2.6 may be rewritten as

$$D^{\mathbf{L}}_{\mu\nu\sigma} \approx \omega_\alpha \sum_{\mathrm{k}}^{\mathrm{BZ}} e^{i\mathbf{k}_\alpha^{\mathrm{T}}\mathbf{L}} D^{\mathbf{k}_\alpha}_{\mu\nu\sigma} \, . \tag{2.55}$$

In the current implementation, open shell defect states with a single one-particle energy in k-space can also be investigated. The implemented methods have been augmented with schemes for semi-conductors and metals (see refs. 111 and 82 and citations therein).

Once the SCF calculations are finished energy gradient is evaluated from eqs. 2.49 and 2.51 using the CFMM scheme for Coulomb contribution and the extended numerical integration scheme for the XC part.

All steps of the DF-CFMM scheme as well as the SCF and gradient calculation procedure described above are parallelized for shared-memory machines using the OpenMP application programming interface.[2]

2.5 Performance

Performance of the implementation for the formation of the KS matrix is evaluated for series of model systems described in app. B, with examples depicted in fig. B.1. All calculations have been carried out using the Becke-Perdew (BP86) exchange-correlation functional.[20,106] The performance and scaling behaviour investigations have employed the split-valence plus polarization (def2-SVP)[116,147] and the pob-TZVP[105] basis sets for molecular and periodic systems, respectively with appropriate auxiliary basis sets.[146] The method details are described in sec. B.2.

2.5.1 Energy

CPU times per SCF iteration for the Coulomb term, its NF and FF parts and the exchange-correlation contribution (matrix and energy) are shown in figs. 2.3 – 2.5. The scaling exponents are determined using logarithmic fit for the largest models in each series. The overlap and kinetic energy matrices are precalculated before entering the SCF loop and stored in a sparse format. Their evaluation time is negligible. The computational cost of remaining SCF procedures, such as formation of the density matrix, orbitals orthonormalization and KS matrix diagonalization is not included since even for the largest test systems the computational cost of the KS matrix formation is the dominant one as shown in tab. 2.1. For the largest model, a $4 \times 4 \times 4$ hematite supercell with 19072 basis functions, it takes about 73% of the total CPU time per SCF iteration. An exception is the alkane series, for which the computational cost of KS matrix formation is comparable to its diagonalization (cf. tab. 2.1). It is noted that for even larger systems the diagonalization of the KS matrix will become the dominant step due to its cubic scaling. However, the availability of an efficient procedure for the formation of the KS matrix opens a possibility for future implementation of low-scaling methods that avoid matrix diagonalization.[58]

As shown in fig. 2.3a the evaluation of the KS matrix for alkane chains achieves approximately linear scaling. For all molecules in the series the CPU times for calculation of the Coulomb and exchange-correlation contributions are similar. Alkanes with over 3000 basis functions exhibit sublinear scaling for the Coulomb term with dominant contribution from the NF part. CPU times for the evaluation of the FF part are less than 5 seconds for the largest alkane in the series.

Fig. 2.3b shows CPU times per SCF iteration for the series of H-terminated graphite sheets. For small models the scaling of the evaluation of the Coulomb term is approximately quadratic and decreases to 1.5 for larger sheets. The computational cost of the NF part is dominant whereas the FF contribution takes only a small

Table 2.1: Performance results for the largest model systems studied: number of basis (N_{bf}) and auxiliary (N_{aux}) basis functions, CPU times (min) per SCF iteration for calculation of the Coulomb (t_J) and exchange-correlation (t_{XC}) terms as well as the whole SCF iteration (t_{SCF}). Computational methods are described in sec. B.2

system	N_{bf}	N_{aux}	t_J	t_{XC}	t_{SCF}
alkane chain $C_{200}H_{402}$	5010	17024	1.2	1.5	4.7
graphite sheet $C_{210}H_{38}$	3340	13266	5.1	1.2	6.9
diamond chunk $C_{246}H_{184}$	4610	17214	78.8	7.5	87.9
1D carbon nanotube $(C_{64})_n$	960	3904	3.8	0.8	4.7
2D α-quartz surface $(Si_{96}O_{192}H_{64})_n$	5024	18528	82.1	4.8	89.4
3D magnesium oxide $(Mg_{64}O_{64})_n$	2496	8320	92.5	4.5	97.5
3D NaCl with F-centre $(Na_{256}Cl_{255})_n$	10985	33729	360.1	18.4	449.6
3D hematite $(Fe_{256}O_{384})_n$	19072	53632	1163.3	62.6	1681.8
3D faujasite $(Si_{192}O_{384})_n$	9408	35520	144.6	4.9	171

portion of the CPU time. The exchange-correlation term shows a perfect linear scaling with the system size and is evaluated significantly faster than the Coulomb contribution.

As shown in fig. 2.3c the scaling behaviour of the formation of the KS matrix for the series of diamond pieces is less favourable than for other molecular systems. CPU times are dominated by the NF part of the Coulomb term, with scaling exponents decreasing from 2.7 to 2.5 with increasing system size. The computational cost of the Coulomb FF contribution and the exchange-correlation part is small with scaling exponents of 1.4 and 1.2, respectively.

Fig. 2.4a shows CPU times per SCF iteration for the series of 1D periodic carbon nanotubes. The times for the formation of the KS matrix are dominated by the Coulomb NF contribution. Calculation of both the NF and FF parts shows nearly $O(N)$ complexity. Formation of the exchange-correlation term achieves a sublinear scaling.

The series of 2D periodic hydroxylated α-quartz (0001) surface models shows similar behaviour with the major part of computational time for the formation of the KS matrix due to the Coulomb NF contribution with scaling exponent of 1.3 (cf. fig. 2.4b). Evaluation of the exchange-correlation and Coulomb FF contributions takes only a small portion of the CPU time with the later showing a sublinear scaling behaviour.

The evaluation of the Coulomb NF part is also the dominant step for the series of 3D periodic models of magnesium oxide (cf. fig. 2.5a). Similar to other periodic test systems the calculation of the FF and exchange-correlation parts takes only little CPU time. The computational effort for the formation of the KS matrix shows nearly perfect linear scaling behaviour with the system size.

Similarly, the timings for the evaluation of the KS matrix in case of the series of F-centre models are dominated by the Coulomb NF contribution with scaling exponent of 1.4 (fig. 2.5b). The computational cost of the exchange-correlation term and the Coulomb FF part is negligible. In both systems calculation of the Coulomb FF contribution achieves a sublinear scaling.

Fig. 2.5c shows CPU times per SCF iteration for the series of hematite supercells. CPU times are dominated by the NF part of the Coulomb term, with scaling exponent of 1.2. For FF part of the Coulomb contribution and the exchange-correlation term a sublinear scaling behaviour is achieved with scaling exponents of 0.7 and 0.9, respectively.

In summary, for all systems the formation of the KS matrix is dominated by the Coulomb NF contribution. For molecular systems it shows an increase of computational complexity with increasing “dimensionality” – from linear alkane models to bulky diamond pieces. For systems comprising about 3000 basis functions the CPU time for the formation of the KS matrix grows from less than one to approximately 30 minutes for alkane and diamond chunk, respectively. Similarly, the scaling exponents increase from 1.0 to 2.5. The main reason for this behaviour is a steep increase of the computational cost of the NF Coulomb contribution due to an increasing number of overlapping charge distributions (basis functions pairs and auxiliary basis functions). This effect is more important for compact systems and diminishes with increasing system size, as demonstrated by the decreasing scaling exponents for H-terminated graphite sheets and diamond chunks. In case of alkane chains the formation of the KS matrix is particularly efficient due to the linear structure resulting in small number of overlapping charge distributions. The sublinear scaling behaviour observed for alkane chains comprising over 3000 basis functions is most probably caused by CPU cache effects.

In periodic systems the computational time for the formation of the KS matrix grows with increasing periodicity from 1D (carbon nanotubes) to 3D (MgO, F-centre models and hematite supercells). For about 1000 basis functions it takes about 4 minutes for carbon nanotube, 10 minutes for hydroxylated α-quartz (0001) surface and over half an hour for 3D systems. Similarly to the molecular case, this effect arises from larger number of near-field Coulomb interactions in denser systems. The scaling exponents for all periodic model systems are close to 1.0, with the highest value of 1.4 for F-centre models. For 2D and 3D systems the Coulomb FF and the exchange-correlation contributions are evaluated within virtually negligible CPU time.

The parallel efficiency of the DF-CFMM implementation is examined using the 3D all-silica faujasite model (fig. B.1i) with the unit cell containing 576 atoms and 9408 basis functions. Tab. 2.2 shows wall times for the evaluation of the Coulomb and exchange-correlation contributions on up to 24 CPU cores. The overall parallel performance is very good with efficiency of 85% for 24 cores. Parallel calculation of the KS matrix using 24 cores takes only about 7.5 minutes.

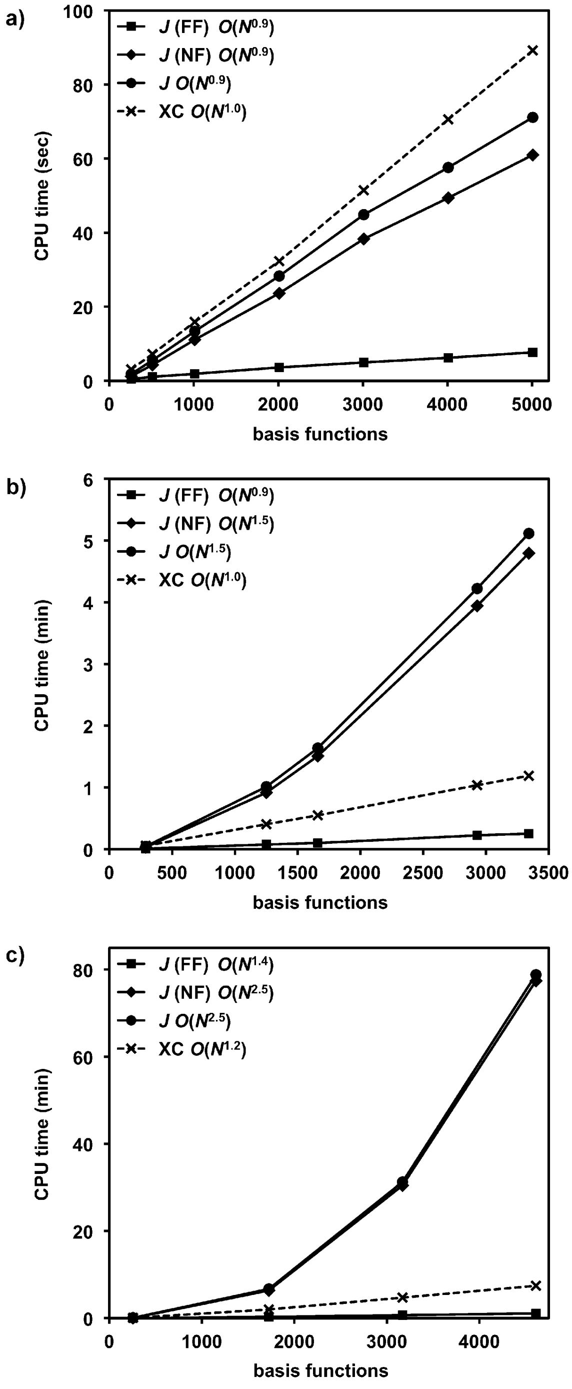

Figure 2.3: CPU timing per SCF iteration for calculation of the NF and FF Coulomb (J) contributions, the total Coulomb term (matrix and energy) and the exchange-correlation (XC) term for a) alkane chains, b) graphite sheets and c) diamond pieces.

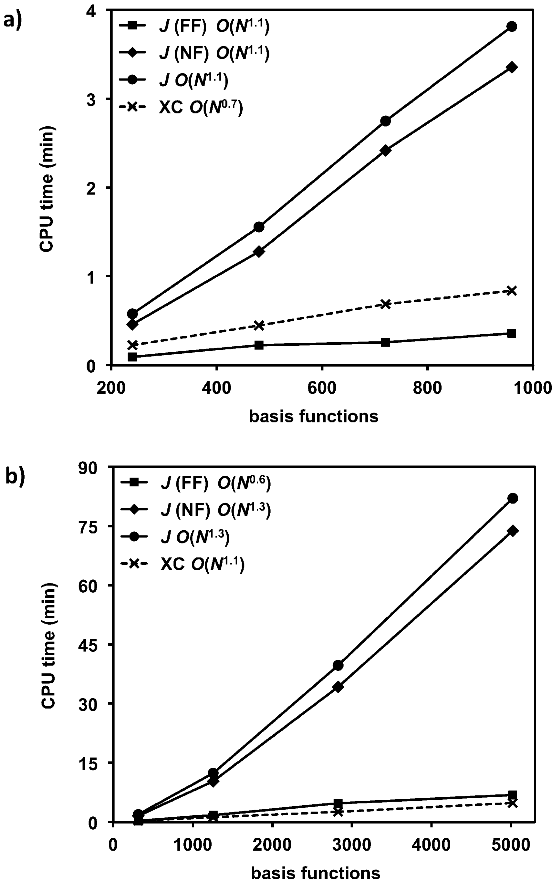

Figure 2.4: CPU timing per SCF iteration for calculation of the NF and FF parts of the CNF Coulomb (J) contribution, the total Coulomb term (matrix and energy) and the exchange-correlation (XC) term for a) 1D carbon nanotubes and b) 2D hydroxylated α-quartz (0001) surfaces.

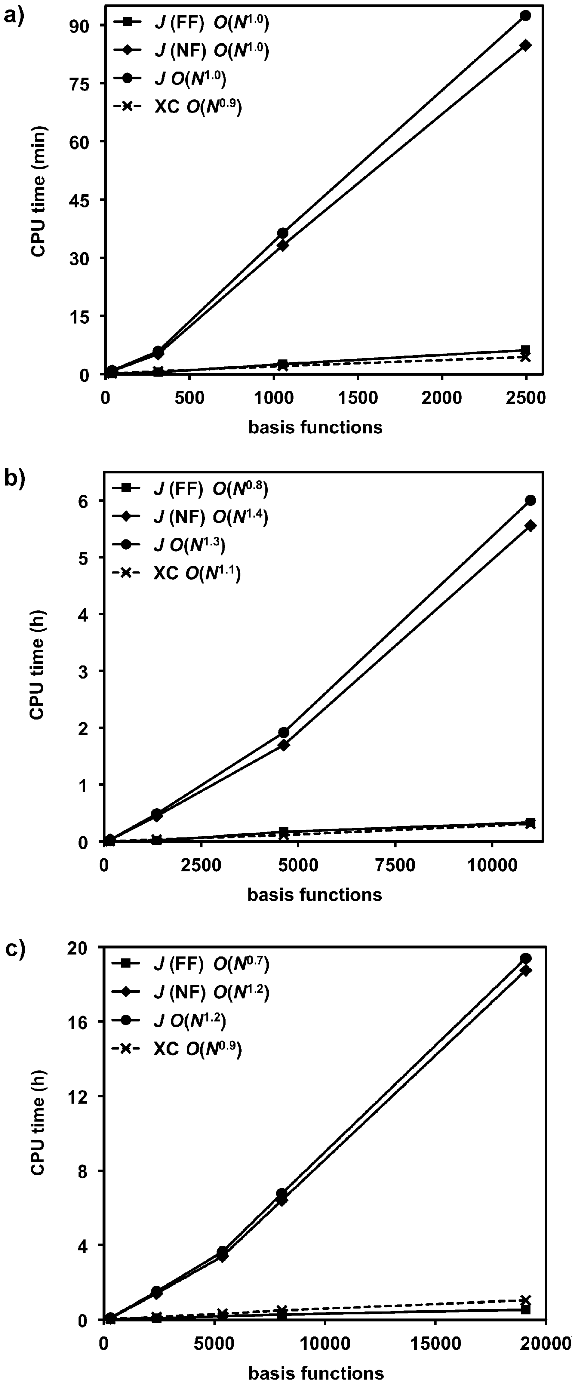

Figure 2.5: CPU timing per SCF iteration for calculation of the NF and FF parts of the CNF Coulomb (J) contribution, the total Coulomb term (matrix and energy) and the exchange-correlation (XC) term for supercells of 3D systems of a) MgO, b) NaCl containing the F-centre and c) hematite.

Table 2.2: 3D periodic faujasite zeolite model (576 atoms and 9408 basis functions): wall times (min) per SCF iteration for parallel computing of the near-field ($t_{\mathbf{J}}^{\mathrm{NF}}$) and far-field ($t_{\mathbf{J}}^{\mathrm{FF}}$) contributions to the Coulomb matrix ($\mathbf{J}$), eq. 2.28, and the $\boldsymbol{\xi}_{\perp}$ vector ($t_{\boldsymbol{\xi}_{\perp}}^{\mathrm{NF}}$ and $t_{\boldsymbol{\xi}_{\perp}}^{\mathrm{FF}}$), eq. 2.27. For comparison total wall times for calculation of the Coulomb t_J and exchange-correlation t_{XC} terms along with the overall parallel efficiency E are given. Computational methods are described in sec. B.2

CPU cores	$t_{\mathbf{J}}^{\mathrm{NF}}$	$t_{\mathbf{J}}^{\mathrm{FF}}$	$t_{\boldsymbol{\xi}_{\perp}}^{\mathrm{NF}}$	$t_{\boldsymbol{\xi}_{\perp}}^{\mathrm{FF}}$	t_J	t_{XC}	E
1	66.5	6.5	62.0	6.5	144.6	4.9	–
2	37.6	3.2	31.8	3.2	77.4	2.6	93%
4	18.8	1.6	15.9	1.6	38.7	1.3	93%
6	13.5	1.1	10.7	1.1	26.9	0.9	90%
12	8.6	0.5	5.4	0.5	15.3	0.5	78%
24	3.6	0.3	2.8	0.3	7.1	0.2	85%

2.5.2 Energy Gradients

CPU times for evaluation of the Coulomb and XC energy gradient contributions are depicted on figs. 2.6 – 2.8. The scaling exponents are obtained by logarithmic fits for the largest systems in each series. Calculations of the XC energy gradient are performed without using grid point weights derivatives, e.g. using only the first term of eq. 2.52

Fig. 2.6a shows CPU gradient evaluation times for the series of alkane chains. The computational cost is dominated by the Coulomb contribution. Calculations of both Coulomb and XC parts shows approximately $O(N)$ complexity, with the latter one showing sublinear scaling for systems containing over 3000 basis functions. For the largest alkane in the series with 5010 basis and 17024 auxiliary basis functions the overall CPU time for energy gradient calculation is below 5 minutes.

In case of H-terminated graphite sheets the scaling behaviour of gradient calculation is less favourable. The CPU times are dominated by the Coulomb part, with scaling exponents close to 2.0 as shown in fig. 2.6b. In contrast, the XC contribution achieves sublinear scaling for the largest systems.

Similar quadratic scaling behaviour for gradient calculation is observed for H-terminated diamond chunks (fig. 2.6c). The scaling exponent for the computationally dominant Coulomb term decreases with systems size from 2.4 to 2.1 for the largest systems, whereas the XC contribution with scaling exponent of 1.3 is evaluated within negligible CPU time.

Fig. 2.7a shows CPU gradient evaluation times for the series of 1D periodic carbon nanotubes. Both the XC and Coulomb contributions show almost linear scaling behaviour with exponents of 1.1 and 1.3, respectively, where Coulomb part is the dominant one and the XC term is evaluated within virtually negligible CPU time. The scaling exponent for the total CPU time is 1.2.

Similarly, for the series of 2D periodic α-quartz (0001) surface models a scaling exponent of 1.2 is achieved for total CPU time. The Coulomb part is the dominant one, whereas computational effort for evaluation of the XC term is negligible. For the later contribution, the sublinear scaling behaviour with exponent of 0.9 is obtained.

The sublinear scaling exponent of 0.9 and the virtually negligible CPU time for evaluation of the XC contribution is also obtained for the series of 3D periodic magnesium oxide supercells, as shown in fig. 2.8a. The dominant Coulomb contribution shows almost linear scaling with the system size.

For the series of NaCl models with F-centre nearly linear scaling of the gradient evaluation is achieved. The computational cost is dominated by the Coulomb term, while the cost of the XC contribution is again negligible. The scaling exponents for both terms are 1.1 and 1.0, respectively.

Fig. 2.8c shows the scaling behaviour of energy gradient calculation for the series of 3D periodic hematite supercells. The overall scaling exponent is 1.3, and similar to other periodic benchmark systems the XC term is evaluated much more efficiently than the Coulomb one.

In summary, the Coulomb contribution to the gradient, in particular the NF part of the CNF contribution, dominates the overall computational cost for both molecular and periodic systems. Only for very elongated structures such as alkane chains the evaluation of the XC term contributes significantly to the CPU time. As shown in tab. 2.3, computational effort of the energy gradient is comparable to that of the Kohn-Sham matrix formation. For the largest periodic models evaluation of energy gradient requires even less CPU time than a single SCF iteration. In case of molecular systems the CPU times and the corresponding scaling exponents for energy gradient calculation increase from linear alkane models to bulky diamond pieces. For models containing about 3000 basis functions CPU times change from 3 (alkane chains) to about 50 (diamond pieces) minutes. Similarly, scaling exponents increase from 1.0 to 2.0. This behaviour is similar to the energy case and diminishes with increasing system size as demonstrated by the decreasing scaling exponents for diamond chunks. Such "surface effect" is absent in case of periodic systems and the scaling exponents for energy gradient calculation are all close to 1.0. For periodic models the computational cost of energy gradient calculation increases with increasing dimensionality of the system. The CPU time for models with about 1000 basis functions changes form 3 minutes for 1D carbon nanotube to 10 minutes for 2D quartz surface and about 20 minutes for 3D systems (magnesium oxide, NaCl F-centres and hematite).

Tab. 2.4 summarizes wall times and parallel efficiency of the gradient implementation on up to 24 cores employing the 3D all-silica faujasite model shown in fig. B.1i. The parallel efficiency of about 90% is very good even for 24 CPU cores.

Table 2.3: Performance results for the largest models studied (see sec. B.1): Number of basis (N_{bf}) and auxiliary basis (N_{aux}) functions as well as CPU times (min) for: Coulomb near- field (t_{NF}), Coulomb far-field (t_{FF}) and XC (t_{XC}) gradient contributions, total gradient (t_{grad}) and Kohn-Sham matrix formation (t_{KS}). Computational methods are described in sec. B.2

system	N_{bf}	N_{aux}	t_{NF}	t_{FF}	t_{XC}	t_{grad}	t_{KS}
alkane chain	5010	17024	3.5	0.3	1.2	5.0	3.0
graphite sheet	3340	13266	9.8	0.5	1.0	11.3	7.8
diamond chunk	4610	17214	88.1	2.5	5.8	96.4	80.3
1D carbon nanotube	1216	3904	3.24	0.84	0.45	4.53	3.9
2D α-quartz surface	6240	18528	53.3	12.1	3.8	69.2	71.6
3D magnesium oxide	2496	8320	49.7	8.4	2.6	60.7	63.9
3D NaCl with F-centre	10985	33729	177.1	30.9	11.7	219.7	242.6
3D hematite	19072	53632	681.4	48.5	45.1	775.0	900.2
3D faujasite	11712	35520	73.3	18.5	5.2	97.0	99.6

Table 2.4: 3D periodic faujasite zeolite model (576 atoms and 9408 basis functions): wall times (min) per SCF iteration for parallel computing of the Coulomb (t_{Coul}) and the exchange-correlation (t_{XC}) term as well as total gradient (t_{grad}). In the last column the overall parallel efficiency E is given. Computational methods are described in sec. B.2

CPU cores	t_{Coul}	t_{XC}	t_{grad}	E
1	81.0	4.6	86.4	–
2	40.8	2.3	43.6	99%
3	28.2	1.6	30.1	96%
4	22.2	1.2	23.5	92%
6	15.2	0.8	16.2	89%
12	7.4	0.40	8.1	89%
24	73.8	0.20	84.1	88%

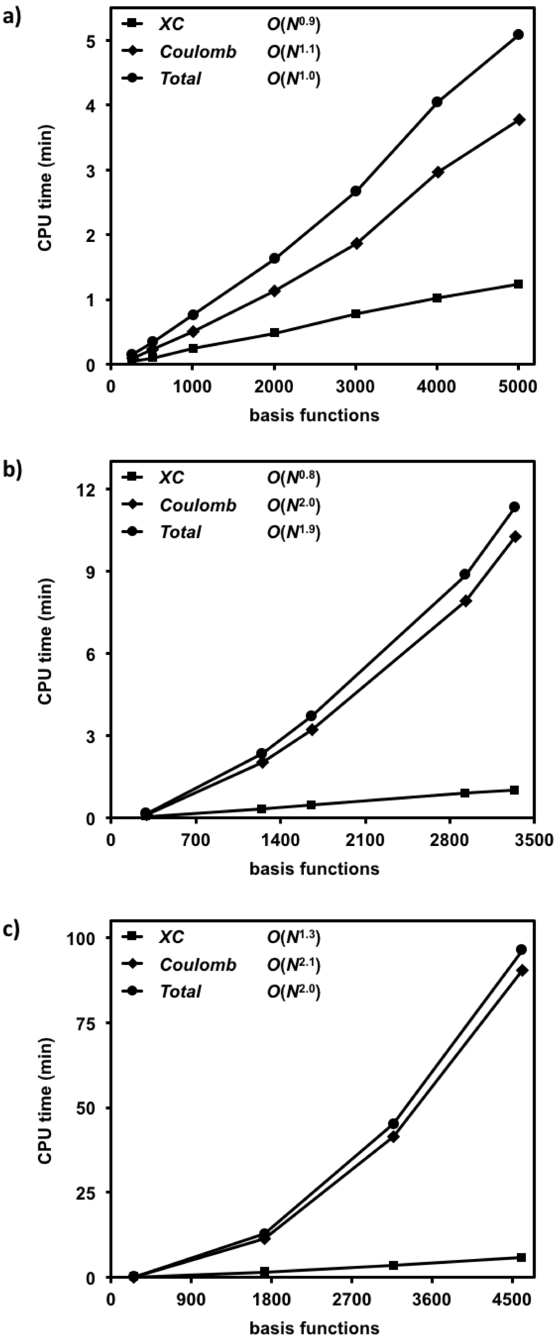

Figure 2.6: CPU times for the Coulomb and XC contributions to energy gradients: a) alkane chains, b) graphite sheets and c) diamond chunks.

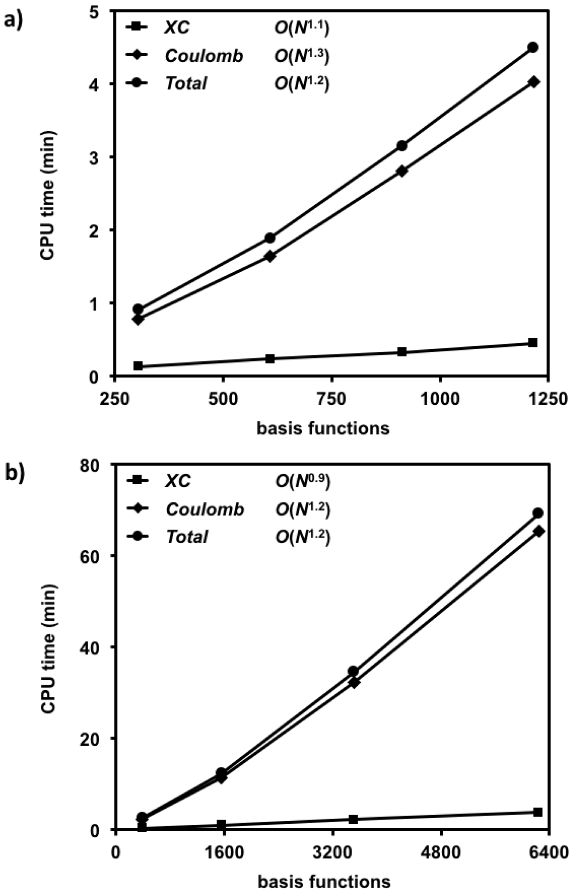

Figure 2.7: CPU times for the Coulomb and XC contributions to energy gradients: a) 1D carbon nanotubes and b) 2D hydroxylated α-quartz (0001) surfaces.

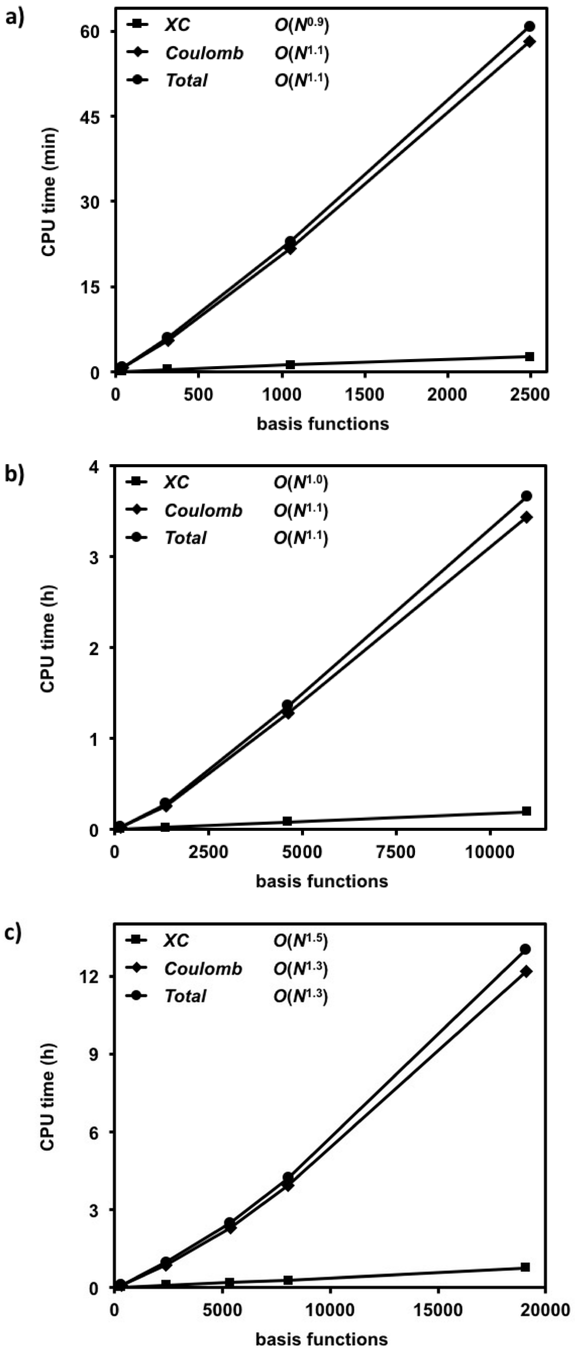

Figure 2.8: CPU times for the Coulomb and XC contributions to energy gradients: a) MgO, b) NaCl systems containing the F-centre and c) hematite.

CHAPTER 3

Applications

With the improved efficiency and usability the DFT implementation described in the previous chapter along with other TURBOMOLE[1,5] modules has been applied to atomic level structural characterization of pure ZnO and CdO as well as mixed ZnO-TiO_2 nanoclusters and ZnO nanoclusters adsorbed on the (101) surface of anatase.

In case of ZnO and CdO nanoclusters theoretical studies are combined with conventional and time-resolved photoelectron spectroscopy (TR–PES, performed by group of Prof. Dr. Gerd Ganteför at the University of Konstanz). It is revealed that these clusters form highly symmetric, rigid structures with a HOMO–LUMO gaps significantly below those of their bulk phase counterparts. These properties make ZnO and CdO clusters promising building blocks for cluster-assembled materials with unprecedented properties. In addition, electron-hole pair localization in the excited state of the cluster anions combined with their structural rigidity leads to extraordinary long-lived states above the band gap virtually independent of the cluster size, defying the rule "every atom counts". The long lifetimes of excited states observed during the experiment are proposed as a general probe helpful in identifying suitable structures for CAMs and hence simplifying their design.

Investigation of combined TiO_2–ZnO matrials revealed apparent similarity of structure as well as excitation energy of pure $(TiO_2)_n$ and mixed $(ZnO)(TiO_2)_n$ clusters. Moreover, the binding of the $(ZnO)_{12}$ cage on the (101) anatase surface has been investigated. A significant decrease of the band gap in adsorption structure has been shown.

This results can be applied in research of novel materials (CAMs or mixed ZnO/TiO_2 systems) with tuned electronic properties which may be used in particular in development solar cells able to catch sunlight in visible regime.

3.1 ZnO and CdO Nanoclusters

In recent years, an increasing scientific and technological interest has been attracted to nanostructured metal oxides in form of clusters, nanoparticles, and nanofilms.[55] At the nano and subnanoscale, some properties of these systems can be very different from those of their atomic and bulk counterparts. The extreme confinement due to the proximity of the interfaces stabilizes new structures and phases that otherwise cannot be obtained as bulk materials.[81] This opens new possibilities for the development of highly functional tailor-made structures by a bottom up approach with clusters serving as building blocks, leading to the so-called cluster-assembled materials (CAMs).[32,37]

There are special prerequisites for clusters to serve as such building blocks, namely, a very rigid structure that also favours three-dimensional assembly and large HOMO–LUMO gaps to prevent fusion of clusters.[32] To this date, fullerites with carbon fullerenes as building blocks that meet all of these requirements present the only CAM obtained from gas-phase entities.[55,99] However, theoretical predictions indicate that new crystalline phases may be accessible via coalescence of size-selected clusters with ZnO, CdO, and MgO as prominent examples.[6,12,32,37,81]

Small clusters have been found to show a strong size dependence ("every atom counts")[68] of their properties such as the gas phase stability,[42] and catalytic activity.[17,87] For example, an unusually long-lived excited state has been observed in Au_6^-; its lifetime is owed to a planar structure and its excitation into an orbital outside the cluster plane, thus resulting in low de-excitation probability. Such an extraordinary long lifetime has not been found in other Au_n^- clusters.[141] Besides cluster geometries, long excited state lifetimes can be influenced by degree of solvatation[25,26] or oxidation.[79] However, general indicators that always apply have not been identified.

In this chapter size-properties dependency is examined for small ZnO and CdO clusters. For these clusters, highly symmetric alternant cage structures have been predicted.[32,37,40–42,54,60,72,80,95,114,124,136,142,143,145,152] Unlike carbon fullerenes comprising five- and six-membered rings, these cages are constructed from rings containing four and six atoms. This tendency arises from the need to avoid homobonding.

This study reports the first combined experimental and theoretical study of gas-phase $(ZnO)_n^-$ and $(CdO)_n^-$ clusters. The lowest energy structures are determined by global structure optimizations at the DFT level and analysed via time-dependent DFT (TD–DFT).

3.1.1 Methods

Experiment. Time-resolved photoelectron spectroscopic studies of ZnO and CdO clusters in gas phase have been performed by the experimental group of Prof. Dr. Gerd Ganteför. In their experiment, metal is vaporized in a pulsed-arc discharge source (PACIS), reacted with oxygen, and mass-selected via time-of-flight mass spectroscopy. A selected cluster bunch is then irradiated with a laser pulse of energy 4.66 (UV) and 3.1 (blue) eV for ZnO and CdO, respectively, which yields the photoelectron spectrum (PES) of the particular cluster species. Time-dependent behaviour of these species following excitation (1.55 eV, red) is probed by detachment of the excited electron via a second laser pulse (3.1 eV, blue; pump–probe spectroscopy).

Calculations. All calculations are performed using the TURBOMOLE[1,5] program package. The multipole accelerated resolution of identity method for Coulomb term[122] along with appropriate auxiliary basis sets[146] is used to speed up the calculations. Structures of the clusters have been obtained from unbiased global structure optimizations employing genetic algorithm (GA)[121] at the DFT level using the PBE[107] exchange-correlation functional and the split-valence def2-SVP[116] basis set. Up to 100 of the most stable structures obtained with GA have been subsequently refined using the quadruple zeta valence plus a double set of polarization functions (def2-QZVPP)[147] basis set. Remaining calculations employ the PBE[107] exchange-correlation functional along with the def2-QZVPP[147] and, in case of $(ZnO)_5$, augmented correlation-consistent polarized valence quintuple-zeta (aug-cc-pV5Z)[49] basis sets. For Cd atoms the appropriate[11] effective core potential (ECP) is used. For all structures reported, the energy minima have been verified by analytical[43,44] and numerical harmonic frequency calculations for the ground and excited states, respectively. Detailed analysis of used method is presented in app. C.

3.1.2 Results and Discussion

3.1.2.1 Zinc Oxide

Size selected $(\mathrm{ZnO})_n^-$ (n = 5, 8, 12, 13, 14, 16) clusters have been investigated by conventional and time-resolved photoelectron spectroscopy accompanied by detailed analysis via TD–DFT. This combined approach not only provide an evidence for the alternant cage structures predicted for $(\mathrm{ZnO})_n$ nanoclusters but also demonstrate their so far unprecedented electronic properties. Laser excitation (1.55 eV) invariably results in exceptionally long-lived excited states independent of the number of ZnO monomers in the investigated size regime. Computational studies find spin density localization on a subset of Zn atoms upon structural relaxation of excited states (electron-hole pair localization) accompanied by radiative lifetimes on the order of 100 ns in all investigated $(\mathrm{ZnO})_n^-$ (n = 5, 8, 12, 13, 14, 16) cluster ions. This behaviour is independent of the symmetry, structure, and size of the clusters. Thus, electron-hole pair localization following the excitation along with structural rigidity of their cage-like structures can be regarded as a prerequisite for extended excited state lifetimes in ZnO cluster anions. In addition, the same behaviour could be observed for n = 18 and 23 also supporting the interpretation, albeit no theoretical assessment has been carried out due to high computational demands of global structure optimizations at the DFT level.

Rough estimates for the HOMO–LUMO gap values have been obtained using PE spectra recorded at 4.66 eV. The procedure uses the slopes of the peaks to determine adiabatic detachment energies (ADEs) of the first and second feature in the PE spectra, arising from detachment of electrons form orbitals corresponding to HOMO and LUMO, and then takes their difference as a measure for the gap size. Spectra of pentamer and dodecamer serving as an example of this method are shown in fig. 3.1. The corresponding values presented in tab. 3.1 show somewhat larger errors due to this crude approach. However, they support results of the calculations, which yield band gaps of approximately 2 eV, well below bulk ZnO. The congruence of theory and experiment is further confirmed by a good agreement of the measured and calculated vertical detachment energies (VDEs), as shown in tab. 3.1.

Calculated structures of $(ZnO)_n^-$ are shown in fig. 3.2. It is noteworthy that for each cluster size, the neutral as well as the ground and excited state of the anion virtually share the same structure.

Electronic properties of $(ZnO)_n^-$ ($n = 5, 8, 12, 13, 14, 16, 18, 23$) cluster anions have been probed by TR–PES. The intensity decay of the excited state obtained by 1.55 eV excitation is followed by electron detachment with a 3.1 eV probe pulse. The temporal evolution of the transient pump–probe feature (A) and the waterfall plot of $(ZnO)_5^-$ is shown in fig. 3.3. The complete row of clusters investigated by red-blue pump–probe spectroscopy shows lifetimes far exceeding the 80 ps limit of the experiment. Conventional UV PES with a photon energy of 4.66 eV could not be obtained for $n = 18$ and 23, most probably because of their low photoionization cross sections. Nevertheless, time-dependent experimental data for $n = 18$ and 23 is shown to corroborate the generality of the long-lived excited state.

The labelling of excited states are presented in fig. 3.4 and fig. 3.5 which also depicts the general excitation–de-excitation scheme. Basically, all studied cluster anions are excited vertically from the ground state D_0 into D_1^* which relaxes, oftentimes via Jahn–Teller type distortion, to D_1 from which electron detachment is observed. This causes the time-variant photodetachment feature to be found at lower energies than 1.55 eV above the ground state. Similar behaviour is exhibited by C_{60}^-.[50] D_1 is vertically de-excited to D_0^*, which finally relaxes back to the ground state D_0. The good agreement between experimental and calculated VDEs (tab. 3.1) mostly confirms structures reported previously and shown in fig. 3.2.[6,12,41,96,101,114,115,136,142,143,145,161] However, the conducted calculations predict HOMO–LUMO gaps of the clusters in the range of 1.94 - 2.57 eV, well below the band gap of bulk zinc oxide (hexagonal and cubic) of 3.3 eV. As already mentioned, the actual gap of the clusters can roughly be estimated from the experimental PE spectra and indeed turns out to be approximately 2 eV (cf. tab. 3.1). This means that the general principle for band gaps to grow with decreasing particle size due to the quantum confinement is broken here, that is, $(ZnO)_n$ clusters show an "inverse quantum confinement effect". Such behaviour is also known from small TiO_2 cluster anions; however, in this case, the bulk value is reached fast at $n = 7$.[156]

Clusters investigated here retain their reduced band gap up to at least 16 ZnO units. These properties might offer a unique possibility to create oxide semiconductors with lower band gaps, a much sought after material, because sulfides and selenides admittedly provide smaller gaps but are less stable and oftentimes undergo photocorrosion.[72] The allotropes of carbon suggest a route to materials with lower band gaps, whereas graphite has no gap at all, C_{60}^- fullerite exhibits $\Delta E_g = 1.7$ eV,[36] and diamond 5.5 eV. The gap in C_{60}^- from the photoelectron spectrum is 1.6 eV,[76] which is very close to the bulk value. Diamond and zinc oxide share the same structure in bulk; therefore, the approach to lower the forbidden zone in ZnO by creating a fullerite-like phase seems viable. Moreover, the conducted investigations demonstrate that ZnO clusters meet perfectly all prerequisites for good CAM building blocks, namely very rigid structures, large HOMO–LUMO gaps in the range of 2 eV, and high symmetry favouring three-dimensional assembly (especially $(ZnO)_{12}^-$ and $(ZnO)_{16}^-$; see fig. 3.2. Such thermally stable, low-band gap and low-density CAMs from dodeca- and hexadecamers of zinc oxide have been predicted by theory.[40,42,54,60,80]

As a remarkable feature, all $(ZnO)_n^-$ ($n = 5, 8, 12, 13, 14, 16, 18, 23$) clusters exhibit very long excited state lifetimes defying the common rule in cluster science "every atom counts". Calculated radiative decay times are approximately 100 ns (see tab. 3.2) and very well explain the observed ones far in excess of 80 ps for all species under investigation. Nonradiative decay pathways seem to be absent in most cases (fig. 3.3). This absence is explained in terms of the rigid structures of these clusters since calculations find virtually the same structure for neutral, anion, and also the excited state of the anion (fig. 3.2). The unusually long-lived excited states are not related to cluster symmetry (fig. 3.2) but rather to the localization of electron density to a subset of Zn atoms (electron-hole pair localization, fig. 3.4, column 4). These properties make small zinc oxide cluster anions potential candidates for dye- or quantum-dot-sensitized solar cells, in which chromophores are used to inject conduction band electrons into suitable electron transporting media, for example, TiO_2.[72]

Stabilization of the anionic form could be achieved by counterbalancing additional charge by a cryptated cation, as it has been shown by A. W. Castleman and S. N. Khanna et al. for As_7^{3-}.[32,37] In addition, the dominant losses responsible for the Shockley-Queisser limit in solar energy conversion are thermalization of hot carriers to the band edges. This means that neutral clusters with their long-lived states above the band gap (see tab. 3.2) possess the first prerequisite for hot carrier extraction (hot carrier chromophores).[103]

The time-dependent photoelectron spectroscopic investigation of zinc oxide nanostructures shows that the excited state with its long lifetime prevails even if the number of ZnO units is changed. This type of behaviour is rather uncommon in small clusters but is not undesired because it makes structures and their respective properties more predictable. This is very advantageous for experiments on surfaces because a targeted feature can then be conserved even if mass resolution is too low to distinguish between adjacent homologues. In addition, cluster-assembled materials are more easily realized because small deviations in the building block would not carry so much weight. Time-dependent functional calculations suggest an electron-hole pair localization that combined with rigid structures of the clusters leads to long-lived excited states, independent of the cluster size and geometrical structure.

Table 3.1: Vertical detachment energies (VDEs) of $(\mathrm{ZnO})_n^-$ (n = 5, 8, 12, 13, 14, 16) as well as the HOMO–LUMO gap ($\Delta\mathrm{E_g}$) of $(\mathrm{ZnO})_n$ clusters (eV). For octamer, values calculated for the two most stable isomers **8A** and **8B**, respectively are presented.

n (structure)	VDE		$\Delta\mathrm{E_g}$	
	exp	calc	exp	calc
5 (**5A**)	1.7	1.82	2.0 ± 0.3	2.57
8	1.9-2.0	1.98, 2.13	not possible	2.29, 2.06
12	2.0	2.22	1.9 ± 0.3	2.43
13	2.1	2.37	1.9 ± 0.3	1.94
14	2.2	2.41	1.8 ± 0.3	1.98
16	2.1	2.44	1.9 ± 0.3	2.14

Table 3.2: Radiative decay time τ (ns) of the lowest dipole allowed excitations in ZnO_n^- and ZnO_n clusters.

n (structure)	5 (**5A**)	8 (**8A**)	8 (**8B**)	12	13	14	16
$\tau_{(\mathrm{ZnO})_n^-}$	81	95	91	70	85	93	98
$\tau_{(\mathrm{ZnO})_n}$	6	80	1963	205	1922	518	266

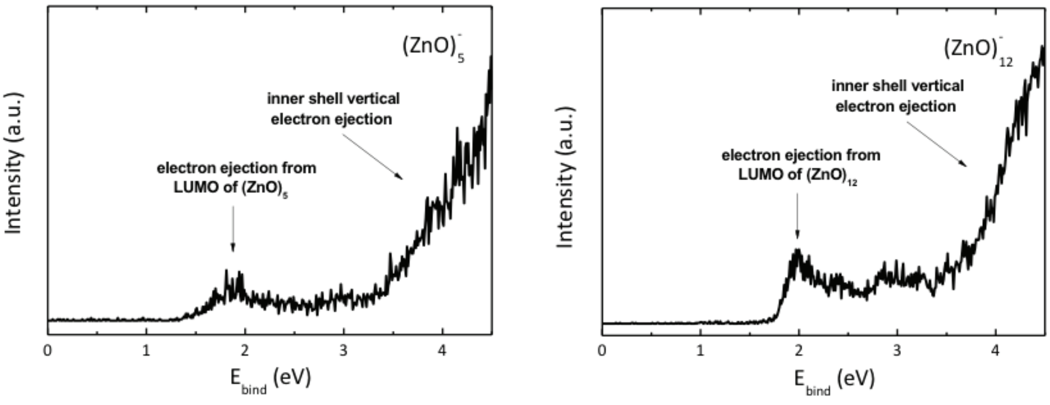

Figure 3.1: Photoelectron spectra obtained with an excitation energy of 4.66 eV for pentamer (left) and dodecamer (right).

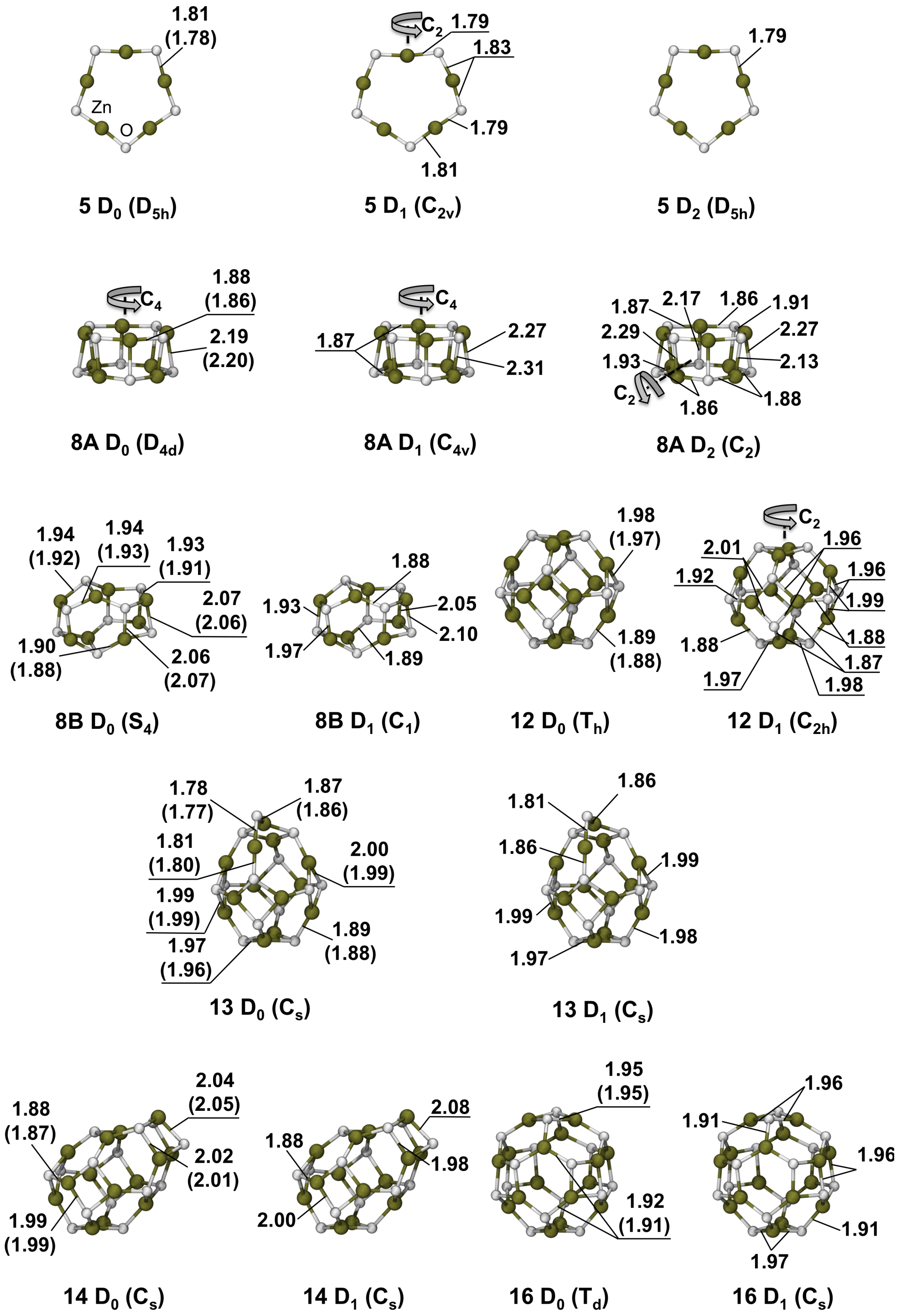
1.81
(1.78)
Zn
O
C2
1.79
1.83
1.79
1.81
1.79
C4
1.88
(1.86)
2.19
(2.20)
C4
1.87
2.27
2.31
1.87
2.17
1.86
1.91
2.29
2.27
1.93
2.13
C2
1.86
1.88
1.94
(1.92)
1.94
(1.93)
1.93
(1.91)
2.07
(2.06)
1.90
(1.88)
2.06
(2.07)
1.88
1.93
2.05
2.10
1.97
1.89
1.98
(1.97)
1.89
(1.88)
C2
2.01
1.96
1.92
1.96
1.99
1.88
1.88
1.87
1.97
1.98
1.78
(1.77)
1.87
(1.86)
1.81
(1.80)
2.00
(1.99)
1.99
(1.99)
1.97
(1.96)
1.89
(1.88)
1.81
1.86
1.86
1.99
1.99
1.97
1.98
1.88
(1.87)
2.04
(2.05)
2.02
(2.01)
1.99
(1.99)
1.88
2.08
1.98
2.00
1.95
(1.95)
1.92
(1.91)
1.96
1.91
1.96
1.91
1.97

5 D_0 (D_{5h}) 5 D_1 (C_{2v}) 5 D_2 (D_{5h})

8A D_0 (D_{4d}) 8A D_1 (C_{4v}) 8A D_2 (C_2)

8B D_0 (S_4) 8B D_1 (C_1) 12 D_0 (T_h) 12 D_1 (C_{2h})

13 D_0 (C_s) 13 D_1 (C_s)

14 D_0 (C_s) 14 D_1 (C_s) 16 D_0 (T_d) 16 D_1 (C_s)

Figure 3.2: Calculated structures of the ground (D_0) and excited (D_1 and D_2) states of $(ZnO)_n^-$ (n = 5, 8, 12, 13, 14, 16), along with related symmetry point groups. Labelling of excited states is presented in fig. 3.5; for pentamer D_2 denotes state after second lowest excitation. Selected Zn-O bond lengths in angstroms and those for neutral clusters in parentheses.

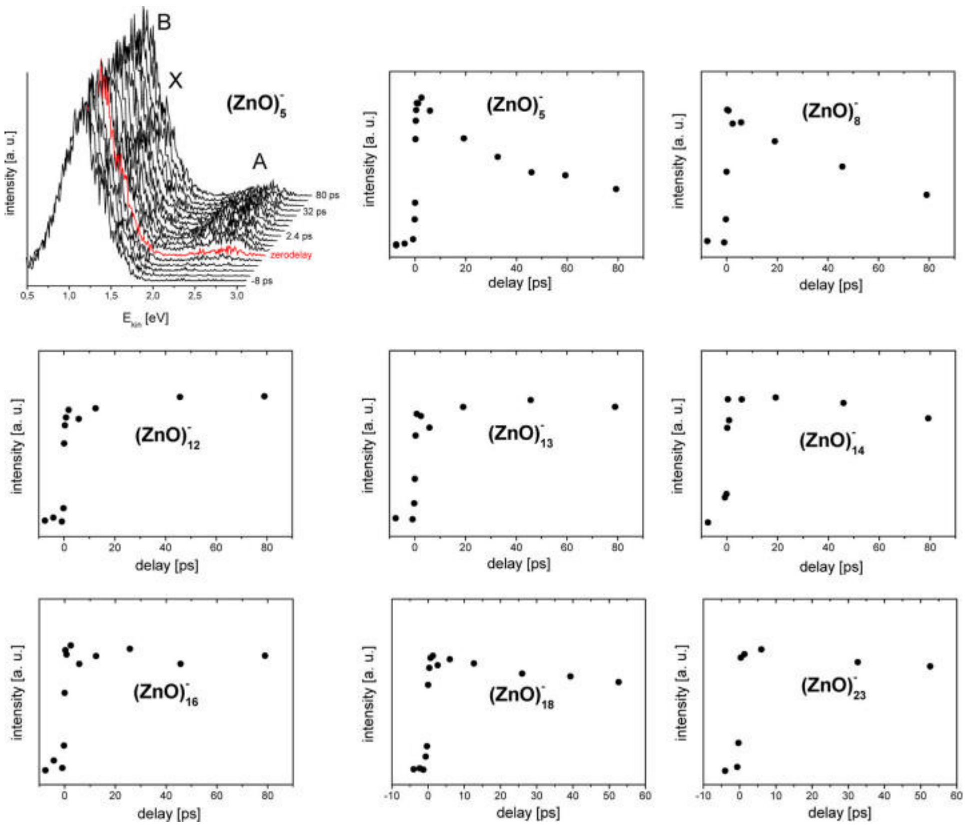

Figure 3.3: Temporal evolution of the transient pump–probe feature (A) following excitation of $(\mathrm{ZnO})_n^-$ (n = 5, 8, 12, 13, 14, 16, 18, 23) with a 1.55 eV laser pulse. In case of $(\mathrm{ZnO})_5^-$, the waterfall plot showing the actual photoelectron spectra at different time delays is presented in addition. Feature A corresponds to the photodetachment from the D_1 state via a 3.1 eV (blue) pulse. Feature B probably stems from photodetachment out of D_1 via a 1.55 eV (red) pulse (two-photon process, red), and finally X is related to the detachment of an electron from D_0. States labelling is presented in figs. 3.5 and 3.4.

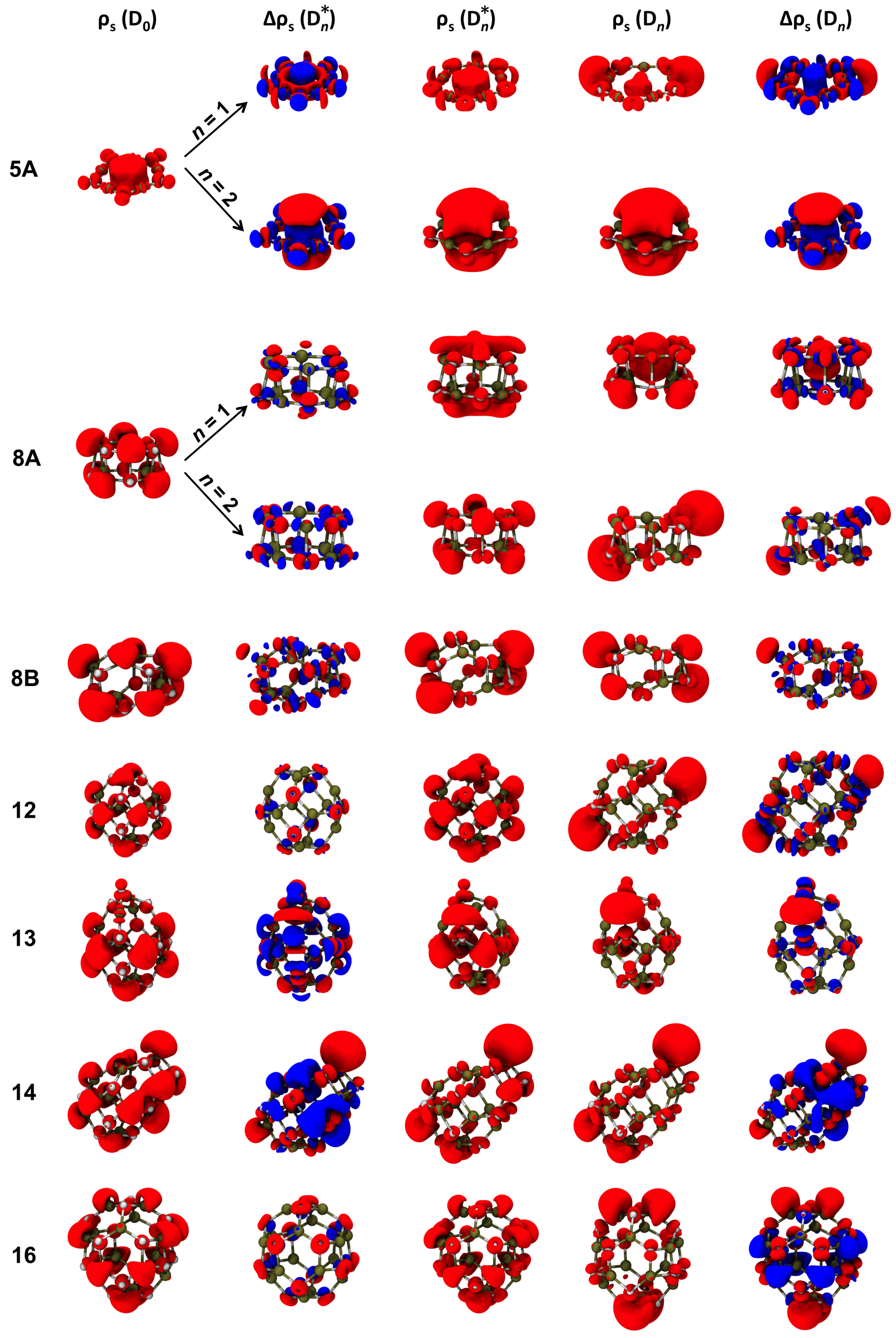
ρs (D0)
Δρs (D*n)
ρs (D*n)
ρs (Dn)
Δρs (Dn)
5A
n = 1
n = 2
8A
n = 1
n = 2
8B
12
13
14
16

Figure 3.4: Spin density isosurfaces for $(\mathrm{ZnO})_n^-$ clusters. The ground state (D_0) and the lowest excited vertical (D_1^*, D_2^*) and adiabatic (D_1, D_2) states are shown in columns 1, 3, and 4, respectively. Columns 2 and 5 show the differential spin density for vertical excitations leading to D_1^* and D_1 states, respectively. Positive values in red, negative values in blue.

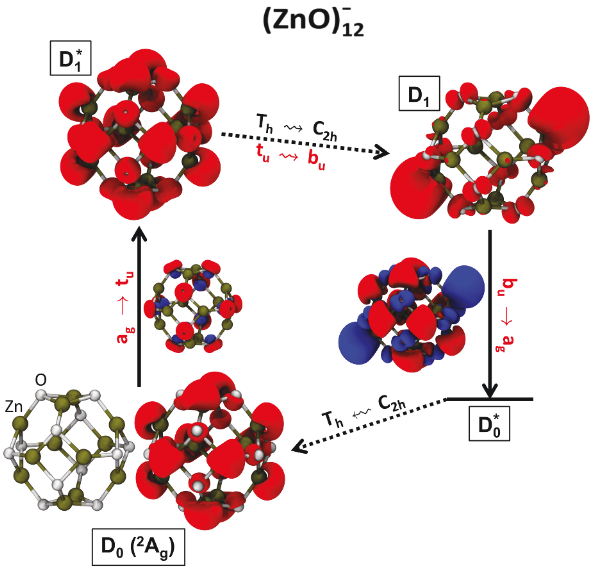
$(ZnO)_{12}^{-}$
D_1^*
D_1
$T_h \rightsquigarrow C_{2h}$
$t_u \rightsquigarrow b_u$
$a_g \rightarrow t_u$
$b_u \rightarrow a_g$
O
Zn
$T_h \leftsquigarrow C_{2h}$
D_0^*
D_0 (^2A_g)

Figure 3.5: Spin density isosurfaces of the ground and excited states of $(ZnO)_{12}^{-}$ (general excitation–de-excitation scheme). Chenges of spin density during excitation and de-excitation shown next to vertical arrows (positive values in red, negative in blue)

3.1.2.2 Cadmium Oxide

Calculated global minimum structures of $(CdO)_n^-$ and $(CdO)_n$ are shown in fig. 3.6. The computed VDEs and ADEs along with corresponding values extracted from PES are summarized in tab. 3.3. In case of VDEs, the agreement between theory and experiment is very good, confirming the structure predictions. For ADEs, the discrepancies are somewhat larger, likely due to peak broadening arising from probing hot species. With the exception of $n = 16$, the VDEs of $(CdO)_n^-$ are roughly 0.5 eV above the VDEs determined previously for $(ZnO)_n^-$ clusters. In all examined structures, the unpaired electron occupies the fully symmetric SOMO. Below the most stable structures of $(CdO)_n$ are described. The striking similarity to corresponding ZnO cluster is emphasized.

The global minimum **8** of both anionic and neutral CdO octamer is the D_{4d} symmetric double four-membered ring shown in fig. 3.6. This result is consistent with the computational study of Matxain et al.[95] and further confirmed by excellent agreement between calculated and experimental VDEs of 2.43 and 2.4 eV, respectively (tab. 3.3). This structure is similar to one of the two lowest energy structures found for ZnO octamer. (see fig. 3.2) Both the structure of the most stable cluster and the spin density distribution in the anion (see figs. 3.6 – 3.8) are virtually identical to $(ZnO)_8^-$.

For the CdO nonamer, the most stable structure is the D_{3h} symmetric tube-like assembly composed of three hexagonal rings (**9A**, fig. 3.6). This structure has been reported as the global minimum by Matxain et al.[95] and also proposed as the global minimum of ZnO nonamer.[136] However, in other studies, **9A** has been reported only as a low energy local minimum and the C_{3h} symmetric cage-like **9B** (fig. 3.6) as the global minimum.[6,142] During my work both structures have been identified as low-lying minima for $(CdO)_9$ and $(CdO)_9^-$ with **9A** only 0.17 and 0.30 eV more stable than **9B** for the anionic and neutral cluster, respectively. To compare these results with ZnO, additional calculations for the ZnO nonamer have been performed. Both the tube- and the cage-like structures have been found to be local minima for $(ZnO)_9$ and $(ZnO)_9^-$. However, the stability order of both structures is reversed with respect to CdO. The C_{3h} symmetric cage is 0.27 and 0.15 eV more stable than the D_{3h} symmetric tube for $(ZnO)_9^-$ and $(ZnO)_9$, respectively. Calculated VDE for the global minimum **9A** of $(CdO)_9^-$ is 2.59 eV, in good agreement with the experimental value of 2.4 eV. The calculated HOMO–LUMO gap of $(CdO)_9$ is 1.21 eV (see tab. 3.3).

The most stable structure of $(CdO)_{12}$ and $(CdO)_{12}^-$ is the T_h symmetric cage **12** shown in fig. 3.6. This structure has been reported as the global minimum for both CdO[95] and ZnO dodecamer. Calculated VDE of 2.85 eV is close to the experimental value of 2.6 eV (tab. 3.3). The calculated HOMO–LUMO gap of $(CdO)_{12}$ is 1.54 eV (tab. 3.3). The spin density of the anion (cf. figs. 3.4, 3.7 and 3.8) closely resembles that of $(ZnO)_{12}^-$.

The C_s symmetric **16A** (fig. 3.6) composed of a fused cubic fragment and hexagonal tube reminiscent of $(CdO)_9^-$ is the global minimum structure of both $(CdO)_{16}$ and $(CdO)_{16}^-$. To my best knowledge, this is the first report of the global minimum for this cluster. **16A** differs from the T_d symmetric cage **16B** found as the global minimum of ZnO hexadecamer (fig. 3.6). However, **16B** is a low energy minimum that is 0.43 and 0.30 eV less stable than the global minimum **16A** for $(CdO)_{16}$ and $(CdO)_{16}^-$, respectively. In case of ZnO, **16B** is 2.0 and 1.9 eV more stable than **16A** for $(ZnO)_{16}$ and $(ZnO)_{16}^-$, respectively. It is noteworthy that the global minimum of CdO hexadecamer partially adopts the cubic rock salt structure of bulk CdO. This may indicate a faster structural convergence of CdO clusters toward the bulk limit as compared to ZnO. Calculated VDE for the most stable structure of $(CdO)_{16}^-$ is 3.0 eV, in good agreement with the experimental value of 2.9 eV (tab. 3.3). In contrast to smaller clusters, the unpaired electron of $(CdO)_{16}^-$ is strongly localized already in the ground state as shown in figs. 3.7 and 3.8. The calculated HOMO–LUMO gap of $(CdO)_{16}$ is 0.79 eV, significantly lower than for smaller cluster sizes (tab. 3.3).

The CdO clusters show structural rigidity similar to that of their ZnO counterparts; in all cases the neutral and anionic species share virtually the same structure. Because all $(CdO)_n$ are closed-shell entities with rigid structures, the observed VDE corresponds to electron detachment from the LUMO of the neutral cluster. Fig. 3.8 demonstrates that shapes of the frontier orbitals (SOMO in anionic and LUMO in neutral clusters) in $(CdO)_n^-$ are virtually identical to those in $(ZnO)_n^-$. If present, the second feature in PES due to electron ejection from the HOMO of the neutral species can be used to provide a rough estimate of the HOMO–LUMO gap, ΔE_g, of the neutral cluster. Unfortunately, the photoionization cross section with a UV photon of 4.66 eV used in the experiments is too low to produce utilizable spectra, and a 3.1 eV photon does not trigger electron detachment from the HOMO of the neutral clusters. However, in the previous study of $(ZnO)_n^-$ anions it has been possible to estimate the experimental ΔE_g from the PES, which are in reasonable agreement with calculated values. It revealed an ”inverse quantum confinement effect” with band gaps of $(ZnO)_n$ clusters well below that of bulk ZnO. The calculated HOMO–LUMO gaps for $(CdO)_n$ clusters in the range of 0.79-1.65 eV (tab. 3.3) are also well below the band gap of bulk cadmium oxide (2.2 eV) and indicate a similar effect.

Time-resolved photoelectron spectroscopy measurements have been carried out for $(CdO)_n^-$ clusters with $n = 8$, 9, 12 and 16. Similarly to the case of ZnO the observed radiative decay times are far in excess of the 50 ps limit of the experiment. Corresponded calculated values tare between 186 and 471 ns (tab. 3.3). Nonradiative decay pathways seem to be nearly absent in all cases. This is the same type of behaviour as found in $(ZnO)_n^-$ clusters. In all examined structures, the lowest (SOMO → LUMO) excitation is accompanied by spin density reorganization leading to its depletion from the inner to the outer part of the cluster and localization of the unpaired electron. The subsequent structure relaxation leads to further electron localization on a subset of Cd atoms. The corresponding spin densities are shown in fig. 3.7. The general excitation and recombination mechanism for all $(CdO)_n^-$ clusters is virtually identical to that of $(ZnO)_n^-$ (cf. figs. 3.5 and 3.9). In all investigated cluster anions, the ground state D_0 is excited vertically into D_1^*, which relaxes, in case of $(CdO)_{12}^-$ via a cluster analogy of the Jahn-Teller type distortion, to D_1 from which electron detachment is observed. D_1 recombines vertically to D_0^*, which relaxes back to the ground state D_0. These results are validated by a good agreement between experimental and calculated VDEs of the D_1 state of $(CdO)_n^-$ (tab. 3.3). The calculated stability difference between ground states before (D_0^*) and after relaxation (D_0) is small, further confirming the rigidity of the clusters.

For $(CdO)_8^-$, the estimated radiative decay time of state D_1 of 379 ns (see tab. 3.3) confirms experimentally observed long lifetime of the excited state of $(CdO)_8^-$. The calculated VDE is 1.34 eV, somewhat lower than the experimental value of 1.8 eV. Vertical excitation results in a spin density reorganization that is virtually the same (see ref. 62) as in case of $(ZnO)_8^-$. However, in contrast to $(ZnO)_8^-$ (cf. fig. 3.2), relaxation of the lowest excited-state structure does not lead to symmetry lowering.

In $(CdO)_9^-$ the lowest excitation is at 1.08 eV. The estimated decay time for **9A** D_1 is 258 ns (tab. 3.3). The calculated VDE is 1.57 eV, in very good agreement with the experimental value of 1.6 eV.

For $(CdO)_{12}^-$, the lowest excitation is the 12 $D_0 \rightarrow$ 12 D_1^* (SOMO → LUMO) transition at 1.33 eV. The triple degeneracy of the 12 D_1^* state leads to an excited-state Jahn–Teller-type distortion upon structure relaxation resulting in symmetry reduction from T_h to C_{2h}. In the final D_1 state, the unpaired electron is located within the b_u symmetric SOMO, localized mainly outside the cluster (fig. 3.7). The calculated VDE of the excited state of 1.69 eV is in good agreement with the experimental value of 1.6 eV. The estimated decay time for the 12 $D_1 \rightarrow$ 12 D_0^* transition is 186 ns (tab. 3.3). The spin density changes during vertical excitation and geometry relaxation are virtually the same as in the case of $(ZnO)_{12}^-$ (cf. 3.9).

The electronic excited states of $(CdO)_{16}^-$ are denser than in the case of smaller clusters resulting in numerous low energy transitions. The lowest one is the **16A** $D_0 \rightarrow$ **16A** D_1^* (SOMO → LUMO) transition at 0.98 eV. The calculated VDE of the D_1 state is 2.13 eV, in good agreement with the experimental value of 1.9 eV (tab. 3.3). The estimated decay time is 471 ns.

Tab. 3.4 summarizes calculated decay times for the lowest dipole allowed singlet excitations of the neutral $(CdO)_n$ clusters. In case of $(CdO)_8$, the two lowest transitions at 1.87 and 1.92 eV are dipole forbidden. For the dodecamer, there is a dark excitation at 1.67 eV. It is noteworthy that for all but $(CdO)_8$ clusters the excitation energies are significantly lower than for the bulk phase (2.2 eV). The estimated radiative decay times vary between 161 and 19382 ns for octamer and hexadecamer, respectively.

Table 3.3: Experimental and calculated vertical detachment energies (VDEs) of $(\mathrm{CdO})_n^-$ in the ground and excited states as well as adiabatic detachment energies (ADEs) in the ground state, vertical excitation energies (ΔE) and radiative decay times τ (ns), calculated HOMO–LUMO gaps (Δ E_g) and binding energies (Δ E_b) of $(\mathrm{CdO})_n$ clusters. Energies in eV.

structure	VDE(D_0)		VDE(D_1)		ADE(D_0)		ΔE	τ	E_g	E_b
	exp	calc	exp	calc	exp	calc				
8	2.4	2.43	1.8	1.34	2.2	2.41	1.24	379	1.65	-3.34
9A	2.4	2.59	1.6	1.57	2.2	2.57	1.08	258	1.21	-3.38
12	2.6	2.85	1.6	1.69	2.4	2.83	1.33	186	1.54	-3.56
16A	2.9	3.00	1.9	2.13	–	2.93	0.98	471	0.79	-3.65

Table 3.4: Calculated radiative decay time τ (ns) of the lowest dipole allowed excitations in $(\mathrm{CdO})_n$ (singlet excitations).

n	8	9	12	16
τ	161	2945	1625	19 382

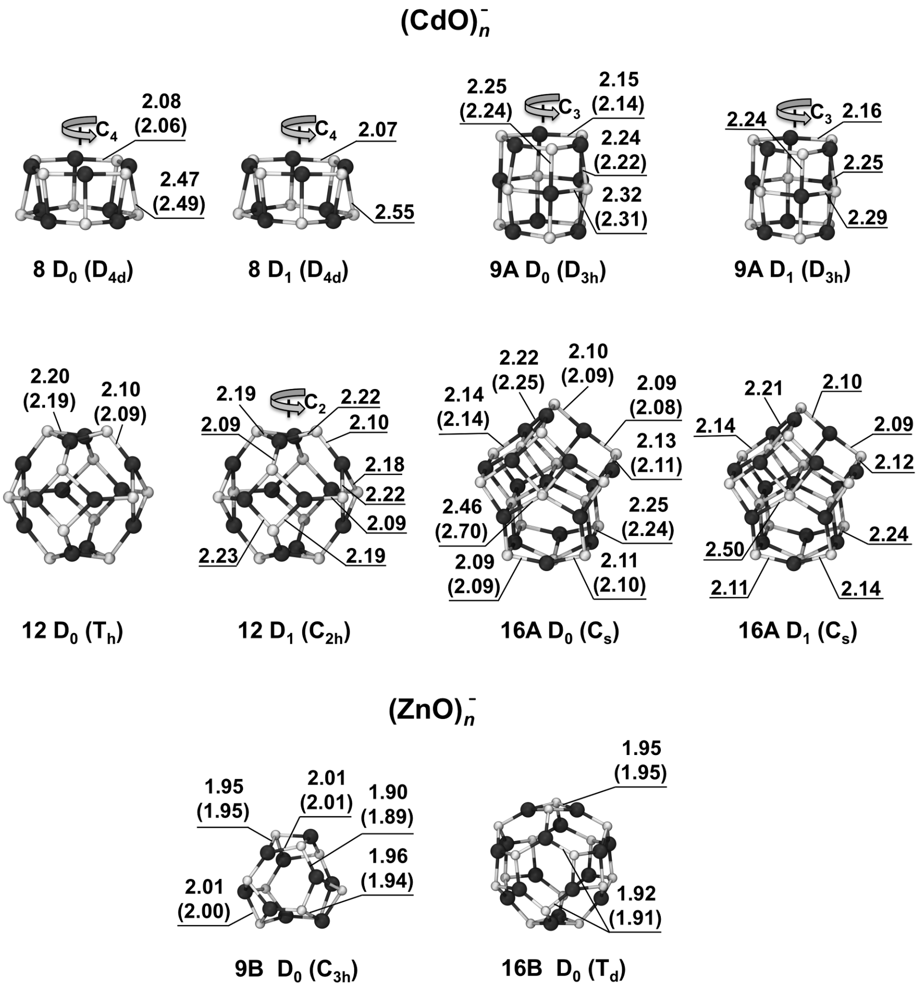
(CdO)n-
C4
2.08
(2.06)
2.47
(2.49)
8 D0 (D4d)
C4
2.07
2.55
8 D1 (D4d)
2.25
(2.24)
C3
2.15
(2.14)
2.24
(2.22)
2.32
(2.31)
9A D0 (D3h)
2.24
C3
2.16
2.25
2.29
9A D1 (D3h)
2.20
(2.19)
2.10
(2.09)
12 D0 (Th)
2.19
C2
2.22
2.09
2.10
2.18
2.22
2.09
2.23
2.19
12 D1 (C2h)
2.22
(2.25)
2.10
(2.09)
2.14
(2.14)
2.09
(2.08)
2.13
(2.11)
2.46
(2.70)
2.25
(2.24)
2.09
(2.09)
2.11
(2.10)
16A D0 (Cs)
2.21
2.10
2.14
2.09
2.12
2.50
2.24
2.11
2.14
16A D1 (Cs)
(ZnO)n-
1.95
(1.95)
2.01
(2.01)
1.90
(1.89)
1.96
(1.94)
2.01
(2.00)
9B D0 (C3h)
1.95
(1.95)
1.92
(1.91)
16B D0 (Td)

Figure 3.6: Global minimum structures of the ground (D_0) and excited (D_1) states of $(CdO)_n^-$ ($n = 8, 9, 12, 16$) along with the corresponding symmetry point group of D_0. Selected Cd-O bond lengths in angstroms, values for the ground state of neutral clusters in parentheses. For comparison, the global minimum structures of $(ZnO)_9^-$ and $(ZnO)_{16}^-$ are shown.

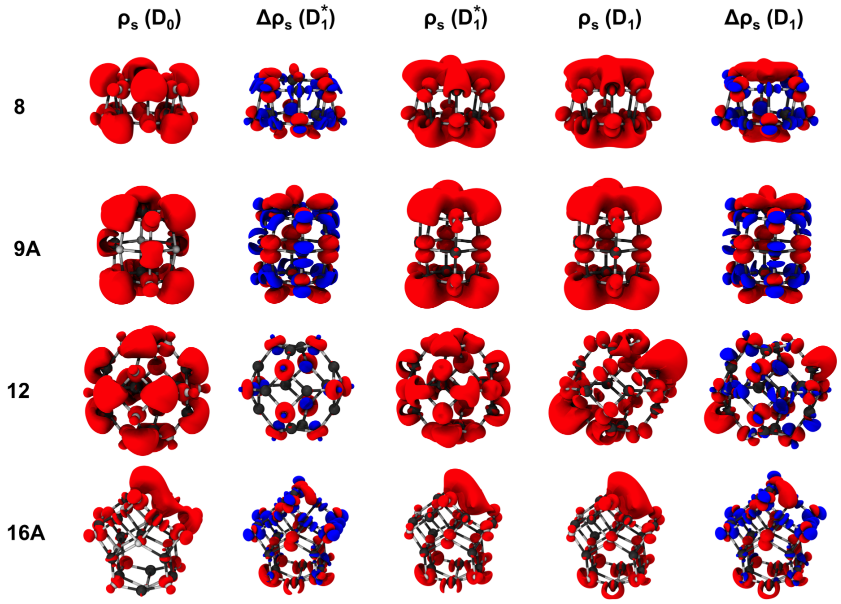

Figure 3.7: Spin density isosurfaces for $(\mathrm{CdO})_n^-$ clusters. The ground state (D_0) and the lowest excited vertical (D_1^*) and adiabatic (D_1) states are shown in columns 1, 3 and 4, respectively. Columns 2 and 5 show the differential spin density for vertical excitations leading to D_1^* and D_1 states, respectively. Positive values in red, negative values in blue.

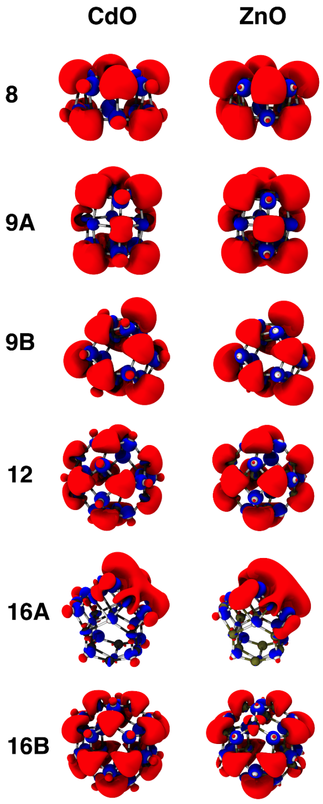
CdO
ZnO
8
9A
9B
12
16A
16B

Figure 3.8: Comparison of SOMO isosurfaces for $(\mathrm{CdO})_n^-$and $(\mathrm{ZnO})_n^-$.

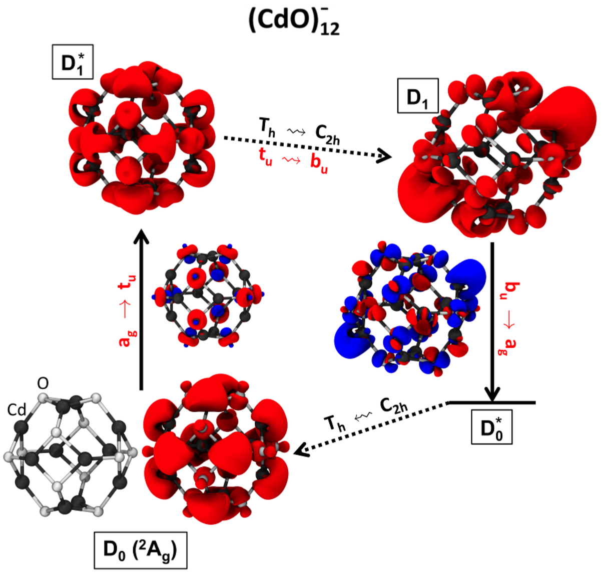

Figure 3.9: General excitation–recombination scheme for $(\mathrm{CdO})_n^-$. Changes of the spin density during excitation and recombination are shown next to the vertical arrows (positive values in red, negative values in blue).

3.2 Mixed ZnO-TiO$_2$ Materials

ZnO and TiO$_2$ based materials, particularly in nanostructured form as nanoparticles, nanotubes and thin films, play an essential role in many fields of modern material science,[10,33,120] in particular as materials for dye-sensitized solar cells[9,73,129,157]. Despite widespread use, ZnO and TiO$_2$ based systems have some drawbacks. For TiO$_2$ it is a low electron mobility, and fast recombination of electrons and holes after excitation. For ZnO, the main drawback is its vulnerability to photo and chemical corrosion. Moreover for both ZnO and TiO$_2$ the maximum of light absorption is blue shifted compared to solar spectrum peak. Therefore, many efforts have been taken to develop new, more efficient materials by adjusting the structure of ZnO and TiO$_2$ by combining both materials or by combining them with other compounds. Recently, systems containing both ZnO and TiO$_2$ have been investigated by several authors. For example, Zhao et al.[162] synthesized Zn-doped TiO$_2$ nanoparticles with high photocatalytic activity. The ZnO has been found to be presented in the form of small clusters dispersed on the surface of anatase-like TiO$_2$ nanoparticles. Another studies on combined TiO_2–ZnO materials have been conducted by Xu et al.[155], who developed high-efficiency solid-state dye-sensitized solar cells with efficiency comparable to liquid-state solar cells. In this chapter properties of the nanoparticles as a function of their size and composition are investigated, along with interactions of ZnO clusters with the surface of large, anatase-like TiO_2 nanoparticles. This will guide development of mixed materials with unprecedented properties, in particular solar cells able to catch sunlight in visible regime.

3.2.1 Computational Methods

As in the previous sections, all DFT and TD-DFT calculations have been performed using the TURBOMOLE[1,5] program package. The multipole accelerated resolution of identity method for Coulomb term[122] along with appropriate auxiliary basis sets[146] is used to speed up the calculations. Structures of neutral and anionic $(TiO_2)_n$ as well as neutral $(TiO_2)_n$ZnO clusters have been obtained by global optimizations employing genetic algorithm (GA)[121] at the DFT level using the PBE[107] exchange-correlation functional and the polarized split valence SVP[116,147] basis sets. The most stable structures have been subsequently refined using the quadruple zeta valence plus a double set of polarization functions (def2-QZVPP)[147] basis set along with PBE0[4] exchange-correlation functional (see app. C).

For examination of absorption of $(ZnO)_{12}$ cluster on anatase PBE[107] exchange-correlation functional and pob-TZVP basis sets[105] have been used (see app. C). Calculations of the bulk phase use the triclinic unit cell containing 4 TiO_2 units with lattice vectors $a = b = 3.82$ Å and $c = 9.70$ Å. The number of k-points used in calculations is 7, 7 and 3 for a, b and c, respectively. The (101) surface is constructed using 2D unit cells with composition $(Ti_4O_8)_n$, where n is the number of oxide layers in model system. The lattice vectors are $a = 3.82$ Å and $b = 10.43$ Å, and the corresponding number of k-points is 9 and 3, respectively. For supercells the number of k-points is varied accordingly.

3.2.2 Results

3.2.2.1 Structure of TiO_2 Clusters

The most stable structures of the $(TiO_2)_n$ clusters with $n = 1$–9 are shown in figs. 3.10 and 3.11 All clusters contain at least one dangling oxygen, i.e. oxygen coordinated to just one Ti atom.

In case of the monomer the most stable structure is C_{2v} symmetric, with bond angle equals to 112° for neutral and 125° for anionic species, which is in good agreement with values of 113° and 128°, respectively, reported by Chertihin and Andrews.[35] The three lowest energy isomers of $(TiO_2)_2$ are presented in fig. 3.10. The **1A** and **1B** structures are C_{2h} and C_{2v} symmetric, respectively and contain two dangling oxygens. The more C_{3v} symmetric compact **1C** structure contains one dangling oxygen. All the structures have been reported before.[7,30,91,156] For neutral cluster the **1A** structure is predicted to be the global minima, as reported before.[22] In case of $(TiO_2)_3$ the most stable structure for both neutral and anionic species is **3A**. This C_s symmetric structure has previously been reported as a global minimum,[7,22,91,156] and **3B** is predicted as another low lying structure[7,91] For $(TiO_2)_4$ the most low lying structures are **4A** and **4B**. For anionic species **4A** is more stable than **4B**, while for neutral one the energetical order is reverted. This is in agreement with previously reported results.[22,91] In case of $(TiO_2)_5$ three low-lying structures have been identified (cf. fig. 3.10). These are the C_1 symmetric **5A** and two more compact C_s symmetric structures **5B** and **5C**. To my best knowledge, none of them has been reported before, however structure **5C** resembles the global minimum proposed in ref. 22. For anionic and neutral clusters the global minima found by the calculations are **5A** and **5C**, respectively.

In case of $(TiO_2)_6$ the most stable structures determined by GA are C_2 symmetric **6A**, C_s symmetric **6B** and C_s symmetric **6C**. Here **6A** is the global minimum for both anionic end neutral clusters, in agreement with the results presented before.[22] For $(TiO_2)_7$ the most stable structures are c_1 symmetric **7A**, **7B** and **7C**, with **7A** as global minimum for both anionic and neutral species, again in agreement with previous reports.[22] For $(TiO_2)_8$ the most stable structure for the anion is **8A**. The

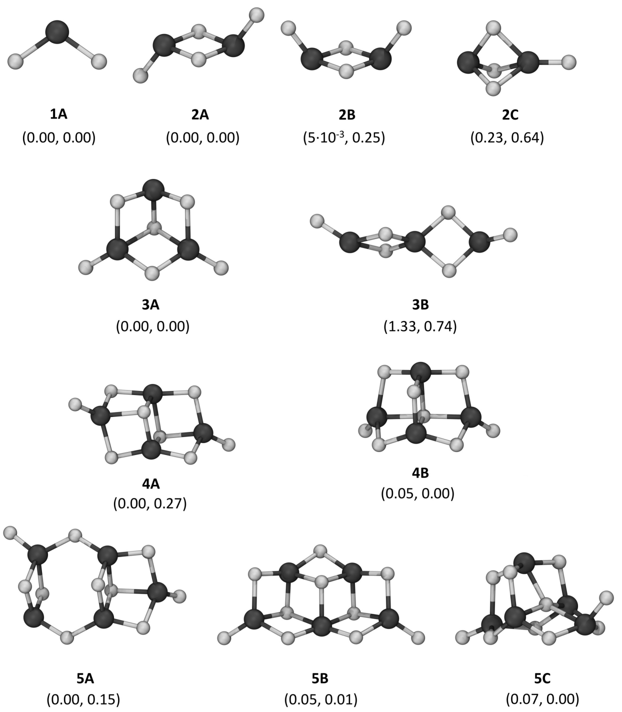

Figure 3.10: Low-energy isomers of $(\mathrm{TiO_2})_n$ clusters for n= 1–5. Relative stabilities (eV) for anionic and neutral clusters in parentheses.

8B isomer is only 0.0008 eV less stable. For neutral clusters the energetical order is inverted, with **8B** 0.11 eV more stable than **8A**. The **8A** have been proposed as $\mathrm{TiO_2}$ octamer minimum by Berardo et al.[22] For $(\mathrm{TiO_2})_9$ the most stable structures for the anion are **9A** and **9B**, with energy difference 0.08 eV. For neutral clusters energetical order is inverted with the **9B** 0.05 eV more stable than **9A**.

Vertical and adiabatic detachment energies along with HOMO-LUMO gaps for the clusters are presented in table (3.5).

3.2.2.2 Structure of $(\mathrm{TiO_2})_n\mathrm{ZnO}$ Clusters

For $(\mathrm{TiO_2})_n\mathrm{ZnO}$ clusters the most stable structures are presented in figs. 3.12 and 3.13. All reported structures are similar to those of pure $(\mathrm{TiO_2})_n$.

For $\mathrm{TiO_2ZnO}$ the most stable structures are **2a** and **2b** with $\mathrm{C_s}$ and $\mathrm{C_{3v}}$ symmetry, respectively, with the latter one 0.81 eV less stable. Structure **1a** is analogous to **2A** and **2B** with one dangling oxygen removed. Similarly, structure **2b** corresponds

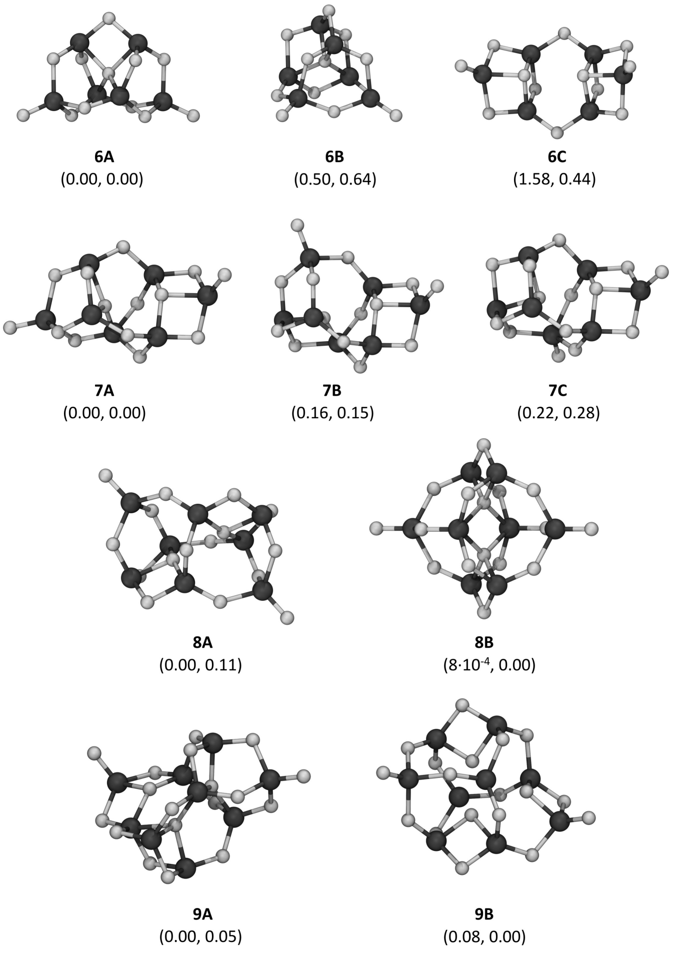

6A
(0.00, 0.00)

6B
(0.50, 0.64)

6C
(1.58, 0.44)

7A
(0.00, 0.00)

7B
(0.16, 0.15)

7C
(0.22, 0.28)

8A
(0.00, 0.11)

8B
(8·10^{-4}, 0.00)

9A
(0.00, 0.05)

9B
(0.08, 0.00)

Figure 3.11: Low-energy isomers of $(\mathrm{TiO}_2)_n$ clusters for $n = 6$–9. Relative stabilities (eV) for anionic and neutral clusters in parentheses.

Table 3.5: Comparison of the calculated spectroscopic properties of (n = 1–9) with experimental data reported by Zhai and Wang.[156] Vertical (VDE) and adiabatic (ADE) detachment energies along with HOMO-LUMO gap ΔE. All values in eV, numbers in parentheses represent estimated experimental uncertainties in the last digits.

n	VDE			ADE			ΔE		
	PBE	PBE0	exp	PBE	PBE0	exp	PBE	PBE0	exp
1	1.48	1.54	1.59(3)	1.52	1.59	1.59(3)	2.09	2.78	2.22(10)
2 a	1.66	1.62		1.92	2.17		2.75	3.22	
2 b	1.92	1.86	2.06(5)	2.18	2.18	2.27(5)	2.46	3.19	2.59(10)
2 c	1.90	2.03		2.08	2.30		2.06	2.59	
3 a	2.69	2.92	2.78(10)	2.99	3.38	3.15(5)	1.05	2.30	2.26(10)
3 b	2.05	2.03		2.21	2.79		2.74	3.02	

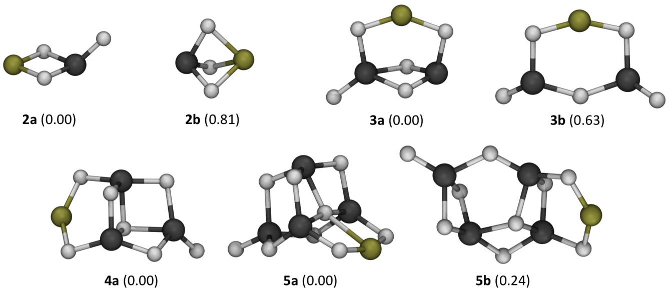

2a (0.00) **2b** (0.81) **3a** (0.00) **3b** (0.63)

4a (0.00) **5a** (0.00) **5b** (0.24)

Figure 3.12: Low-energy isomers of $(TiO_2)_nZnO$ clusters for n = 1–4. Relative energies stabilities (eV) in parentheses.

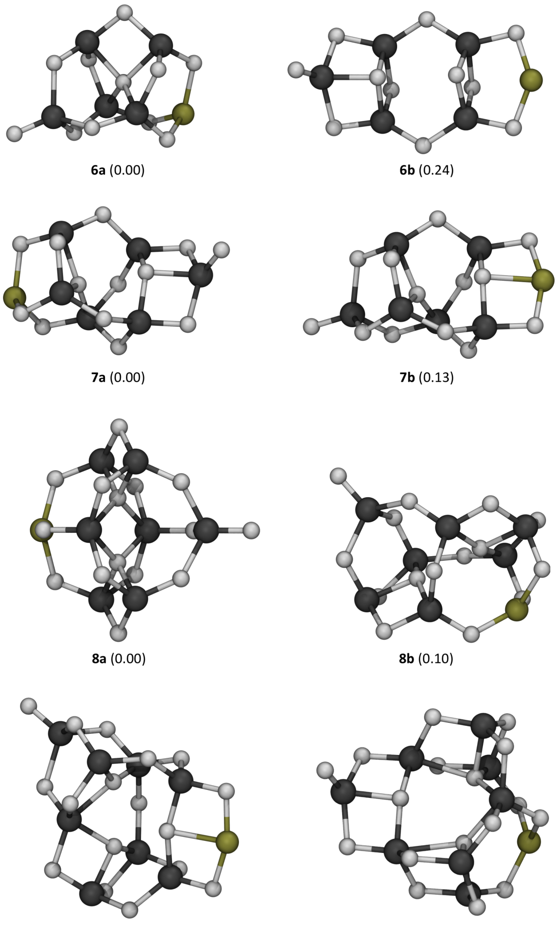

6a (0.00) **6b** (0.24)

7a (0.00) **7b** (0.13)

8a (0.00) **8b** (0.10)

9a (0.00) **9b** (0.01)

Figure 3.13: Low-energy isomers of $(\mathrm{TiO_2})_n\mathrm{ZnO}$ clusters for n = 5–8. Relative stabilities (eV) are given in parentheses

to **2C**. In case of $(TiO_2)_2ZnO$ the most stable structure is C_s symmetric **3a**, similar to the **3A** isomer of titanium dioxide. The C_2 symmetric **3b** is 0.64 eV higher than **3a** and has no counterpart among low lying $(TiO_2)_3$ structures. Structure **4a** is the global minimum of $(TiO_2)_3ZnO$. It can be derived from both **4A** and **4B** by replacing one Ti-O group by Zn and slight reorganization of remaining atoms. For $(TiO_2)_4ZnO$ the most stable structure is **5a**, similar to the global minimum of neutral TiO_2 pentamer **5C**. Isomer **5b** is 0.24 eV less stable, and corresponds to **5A**.

In case of $(TiO_2)_5ZnO$ two global minima **6a** and **6b** correspond to pure TiO_2 clusters **6A** and **6B**. Isomer **6a** is 0.24 eV more stable than **6b**. The global minima of $(TiO_2)_6ZnO$ are **7a** and **7b**, with the first one 0.13 eV more stable than the latter one. Both structures are very similar and differ only by exchange of Zn and TiO group. Again, a striking similarity with structures **7A**, **7B** and **7C** is observed. For $(TiO_2)_7ZnO$ the global minimum **8a** corresponds to the **8B**. Isomer **8b** is 0.10 eV less stable, with its structure similar to **8A**. The most stable isomers of $(TiO_2)_8ZnO$ are two energetically close **9a** and **9b**, with the latter one 0.01 eV less stable. Despite some similarities, none of them can be derived from lowest lying structures of $(TiO_2)_9$.

3.2.2.3 Excitation Energies of Pure and Zn-Containing Clusters

Values of VDE, ADE and HOMO–LUMO gaps of the most stable $(TiO_2)_n^-$ clusters are presented in tab. 3.6 Results of Zhai et. al.[156] are given for comparison. Fair agreement between calculated and experimental properties confirms validity of the used method. Similarly to the case of ZnO and CdO an "inverse quantum confinement effect" is observed, at least for $n \leq 7$.

Calculated values of the lowest singlet excitations for $(TiO_2)_n$ and $(TiO_2)_nZnO$ neutral clusters are presented in tab. 3.7. The difference between excitations energy of corresponding pure TiO_2 and Zn-containing clusters of 1.79 for the smallest structure decreases with increasing system size, and almost vanishes already at $n = 7$. Thus, it is suggested that tuning electronic properties of TiO_2 nanoclusters by combining them with ZnO is not feasible.

Table 3.6: Comparison of the calculated spectroscopic properties of $(\mathrm{TiO}_2)_n^-$ (n = 1–9) with experimental data reported by Zhai and Wang.[156] Vertical (VDE) and adiabatic (ADE) detachment energies along with HOMO–LUMO gap (ΔE). All values in eV, numbers in parentheses represent estimated experimental uncertainties in the last digits.

n	ADE		VDE		ΔE	
	exp	calc	exp	calc	exp	calc
1	1.59(3)	1.54	1.59(3)	1.59	2.22(10)	2.78
2	2.06(5)	1.62	2.27(5)	2.17	2.59(10)	3.22
3	2.78(10)	2.92	3.15(5)	3.38	2.26(10)	2.30
4	3.00(15)	2.95	3.65(5)	3.83	2.60(15)	2.55
5	3.15(20)	3.08	4.13(10)	3.75	2.85(20)	2.70
6	3.20(20)	3.05	4.00(10)	3.93	3.00(20)	2.73
7	3.30(25)	2.94	4.20(15)	3.86	3.10(25)	3.10
8	3.5(3)	2.85	4.70(15)	3.85	3.1(3)	3.07
9	3.6(3)	3.25	4.75(15)	4.27	3.1(3)	2.75

Table 3.7: Comparison between excitation energies (eV) of corresponding $(\mathrm{TiO}_2)_{n+1}$ and $(\mathrm{TiO}_2)_n\mathrm{ZnO}$ structures.

n	1	2	3	4	5	6	7
structure	**2A/2a**	**3A/3a**	**4B/4a**	**5C/5a**	**6A/6a**	**7A/7a**	**8B/8a**
ΔE $(\mathrm{TiO}_2)_{n+1}$	4.11	3.42	4.28	4.25	4.32	4.49	4.53
ΔE $(\mathrm{TiO}_2)_n\mathrm{ZnO}$	2.32	3.62	4.18	4.43	4.26	4.56	4.54

3.2.2.4 Adsorption on Anatase (101) Surface

The anatase structure of TiO_2 is of great interest, as in many cases it exhibits a higher activity than other polymorphs.[59,74] Moreover, this form is very popular among TiO_2 nanostructures,[45] in particular there are experimental evidences[159] that in the TiO_2–ZnO nanoparticles ZnO is present in form of small clusters on the anatase TiO_2 surface. The (101) surface is the most stable,[45,59] and forms over 90% of the total exposed surface in natural crystals.[118] Here adsorbtion of ZnO_{12} cage (see sec. 3.1.2.1) on anatase is investigated.

In order to find the minimal slab thickness needed to model the crystal surface, calculations on systems containing 3, 5 and 7 oxide layers have been conducted. In each case atom coordinates of the most inner layer are frozen in the bulk-like configuration. After geometry relaxation, surface energies γ are calculated as

$$E_{\mathrm{slab}} = nE_{\mathrm{TiO_2}} + 2A\gamma \tag{3.1}$$

where E_{slab} is the total energy of the slab, $E_{\mathrm{TiO_2}}$ is the energy of the bulk TiO_2 unit, n is the number of units in the model and A is the exposed area of one side of the slab. Tab. 3.8 summarizes the obtained results. It is observed, that relaxation of at least two oxide layers leads to almost converged values of γ which are in good agreement with results of Gong et. al.[59]

Interactions between ZnO dodecamer and anatase (101) surface are investigated using (2 × 4) slab of three TiO_2 layers (a = 31.49Å and b = 28.88Å). Atoms of the lowest layer are fixed at their bulk positions. As there are two faces of $(ZnO)_{12}$ (tetra- and hexagonal ring), two initial binding configurations have been used. On the contrary to previous reports[110] adsorption is observed for both configurations. Binding energy is calculated as

$$E_{\mathrm{bind}} = E_{\mathrm{surf\text{-}ZnO}} - (E_{\mathrm{surf}} + E_{\mathrm{ZnO}}) \tag{3.2}$$

with $E_{\mathrm{surf\text{-}ZnO}}$ as energy of the system after adsorption, and E_{surf} and E_{ZnO} as energies of surface and ZnO_{12} cluster before reaction. Adsorption energies for tetra- and hexagonal configurations are 3.76 and 4.59 eV, respectively. For the first case the resulting bonded structure is depicted in fig. 3.14a. The highly symmetric structure

Table 3.8: Surface energies (eV) for model systems of varied thickness. In each model geometry optimization for n oxide layers on each side of the slab has been performed. Resulst of Gong et. al.[59] are presented for comparison.

n	1	2	3	Gong et. al.
energy	$4.1 \cdot 10^{-2}$	$3.7 \cdot 10^{-2}$	$3.6 \cdot 10^{-2}$	$3.5 \cdot 10^{-2}$

of ZnO cluster is prevailing. To check convergence of the model systems additional calculations are conducted. For (3 × 6) slab of three layers (a = 59.11Å and b = 43.33Å) adsorption energy of 3.84 eV has been found. In case of (2 × 4) slab with four oxide layers the resulting energy equals 3.72 eV. It is concluded, that using more extensive models does not lead to a significant difference in the obtained results. Adsorption of $(ZnO)_{12}$ with the hexagonal face is presented in fig. 3.14a. In this case initial cluster structure is destroyed.

HOMO–LUMO gaps of TiO_2–ZnO systems are calculated directly from energies of SCF orbitals. Values of 2.64 eV and 2.16 eV are obtained for ZnO dodecamer and anatase surface, respectively. In case of adsorbed clusters gap of 0.76 eV and 1.05 eV for hexa- and tetragonal face configuration, respectively, has been obtained. It is well known,[64,108] that PBE tends to underestimate band gaps. Nevertheless, this error is systematic and may be corrected by applying an appropriate scaling factor (see for example refs. 104, 154 and fig. 1 in 64). Thus, the qualitative conclusion of a significant band gap decrease is justified.

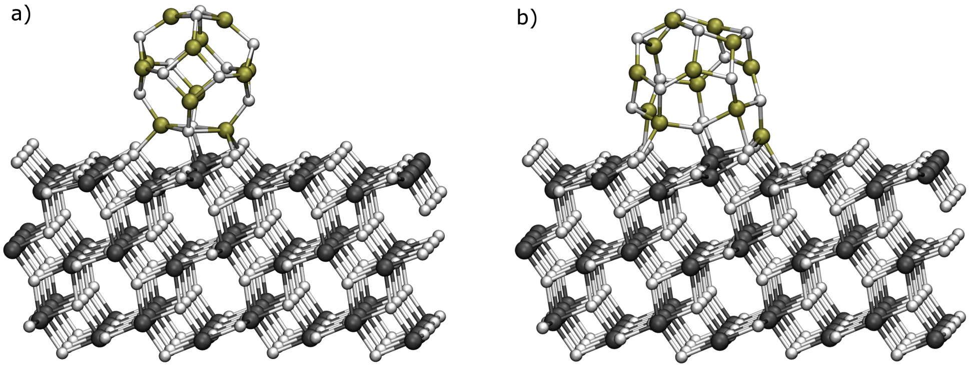

Figure 3.14: ZnO dodecamer adsorbed on TiO_2 anatase (101) surface using the a) tetragonal and b) hexagonal face.

Chapter 4

Conclusions and Future Investigation

4.1 Density Functional Theory for Molecular and Periodic Systems

Using the combination of DF approximation and CFMM scheme an efficient DFT method using Gaussian-type orbitals as basis functions has been implemented. The implementation treats molecular as well as periodic systems of any dimensionality on an equal footing and achieves an asymptotic $O(N)$ scaling for calculation of energy and its gradient. In this DF-CFMM approach the Coulomb interactions are partitioned into near- and far-field contributions. The far-field part is evaluated very efficiently using a hierarchy of multipole expansions whereas the calculation of the near-field contribution employs the DF scheme. For systems with periodic boundary conditions both contributions are evaluated entirely in direct space. The efficiency and scaling behavior of the implementation is tested using series of molecular and periodic model systems of increasing size, with the largest unit cell of hematite containing 640 atoms and 19072 basis functions.

4.2 ZnO and CdO Nanoclusters

The most obvious conclusion to be drawn from the combined experimental and theoretical study is a striking similarity between $(\mathrm{CdO})_n$ and $(\mathrm{ZnO})_n$ fragments at least up to $n = 12$. Although in some cases the order of stability of low energy structures is different, both systems show very similar structures and electronic properties in their ground and excited states. For larger clusters, the structural differences can be attributed to a different convergence rate toward different bulk limits, wurtzite or zinc blende for ZnO and rock salt structure for CdO. Because of similar frontier orbitals, the excitation–recombination pathways in $(CdO)_n^-$ are virtually identical to their $(ZnO)_n^-$ counterparts. They involve electron localization within the relaxed excited state, which together with rigid cluster structures leads to the observed exceptionally long-lived excited states, approximately 1 eV above the conduction band edge (LUMO of the neutral). These results render both rows of cluster homologues suitable building blocks for ACCAMs and, in addition, their excited-state lifetimes a valuable probe for the aptitude to serve as such.

Despite similar structures, electronic properties of the clusters are slightly different for both materials. The VDE basically determines the location of the conduction band (LUMO) of the neutral cluster, and it can be tuned from 2.0 eV for $(ZnO)_{12}$ to 2.6 eV for $(CdO)_{12}$. Also, the band gap is tunable between 2 eV for $(ZnO)_n$ and 1.2 eV for $(CdO)_n$. This has practical implications because the former, as light-harvesting chromophore, would not capture the complete spectrum of sunlight, while the latter with its low band gap is absolutely capable of doing just that. These results demonstrate that gas-phase studies of potential ACCAMs building blocks could facilitate band engineering and rational materials design. This approach seems especially viable because the HOMO–LUMO gap of C_{60} in the gas phase is 1.6 eV,[76] very close to bulk fullerite with $\Delta E_g = 1.5$ eV[148] Finally, the existence of a more general rule for $E^{II}O$ fragments (E^{II} = divalent element) forming $(E^{II}O)_n$ clusters with similar properties is suggested. In the future, the ACCAM construction kit may be expanded by investigation of more general rows of cluster homologues, including groups II-VI[61,93,95,97,102,134,135,144] and III-V[38,39,78,98,117,127,128,153,158,160] semiconductors of the type $(E^{II}Ch)_n$ (Ch = chalcogen, e.g., ZnS, ZnSe) and $(E^{III}Pn)_n$ (E^{III} = trivalent element, Pn = pnictogen, e.g., AlN, AlP), respectively.

4.3 Mixed ZnO-TiO_2 Materials

For molecular calculations, the striking similarity between structures of $(TiO_2)_n$ and $(TiO_2)_n$ZnO clusters has been observed. Examination of excitation energies revealed no consistent shift between Zn-containing and pure TiO_2 entities. Moreover, the corresponding excitation energy difference decreases with increasing the cluster size, and almost vanishes for structures containing at least 8 metal atoms. For pure clusters up to TiO_2 heptamer an "inverse quantum confinement effect" is observed.

Adsorption of ZnO dodecamer on anatase (101) surface has been investigated using the TURBOMOLE module developed during my PhD. The strong binding between $(ZnO)_{12}$ and the surface as well as significant reduction of the band gap in resulting system has been found for both tetra- and hexagonal configurations. This results suggest that deposition of $(ZnO)_n$ clusters on anatase-like nanostructures may result in novel materials with tunable properties, in particular solar cells capable of efficient capturing the sun light. Nevertheless, to achieve this further investigations are required. In particular, general adsorption behaviour of $(ZnO)_n$ clusters with varying size needs to be examined. Moreover, excited states properties have to be investigated using for example periodic electrostatic embedded cluster method.

Appendix A

Multipole Expansion

Calculation of the Coulomb interaction

$$\big(\rho_1(\mathbf{r})|\rho_2(\mathbf{r}')\big) = \int\int \frac{1}{2}\frac{\rho_1(\mathbf{r})\rho_2(\mathbf{r}')}{|\mathbf{r}-\mathbf{r}'|}d\mathbf{r}d\mathbf{r}' \tag{A.1}$$

is done using the factorisation[149]

$$\frac{1}{|\mathbf{r}-\mathbf{r}'|} = \sum_{l=0}^{\infty}\sum_{m=-l}^{l} O_{lm}(\mathbf{r})M_{lm}(\mathbf{r}') \tag{A.2}$$

with elements $O_{lm}(\mathbf{R})$ and $M_{lm}(\mathbf{R})$ defined using scaled associated Legandre polynomials. For $\mathbf{R} = (R, \theta, \phi)$ in spherical coordinates they are:

$$O_{lm}(\mathbf{R}) = \frac{R^l}{(l+|m|)!}P_{lm}(\cos(\theta))e^{-im\phi} \tag{A.3}$$

$$M_{lm}(\mathbf{R}) = \frac{(l-|m|)!}{R^{l-1}}P_{lm}(\cos(\theta))e^{im\phi} \tag{A.4}$$

Using the above terms, equation (A.1) is rewritten as

$$\begin{aligned}\big(\rho_1(\mathbf{r})|\rho_2(\mathbf{r}')\big) &= \sum_{l=0}^{\infty}\sum_{m=-l}^{l}\int \rho_1(\mathbf{r})O_{lm}(\mathbf{r})d\mathbf{r}\int \rho_2(\mathbf{r})M_{lm}(\mathbf{r})d\mathbf{r} \\ &= \sum_{l=0}^{\infty}\sum_{m=-l}^{l}\omega_{lm}^{\rho_1}\mu_{lm}^{\rho_2}. \end{aligned} \tag{A.5}$$

In practice, the infinite sum in eq. A.2 have to be truncated at L_{max}. The introduced error is bounded by

$$\frac{1}{|\mathbf{r}-\mathbf{r}'|}\left(\frac{r}{r'}\right)^{L_{max}+1}. \tag{A.6}$$

Thus equation A.2 requires r' larger than r. Multipole expansions about given origins can be shifted and transformed one into another using the following operators:[149]

- "extrenal to external" operator A: translates multipole expansion about **a** to $\mathbf{a} + \mathbf{b}$

$$\omega(\mathbf{a} + \mathbf{b}) = A(\mathbf{b}) \otimes \omega(\mathbf{a}) \tag{A.7}$$

- "extrenal to local" operator B: transforms multipole expansion about **a** to Taylor expansion at **a - b**

$$\mu(\mathbf{a} - \mathbf{b}) = B(\mathbf{b}) \otimes \omega(\mathbf{a}) \tag{A.8}$$

- "local to local" operator C: translates Taylor expansion at **b** to **r - b**

$$\mu(\mathbf{a} - \mathbf{b}) = C(\mathbf{a}) \otimes \mu(\mathbf{b}) \tag{A.9}$$

Appendix B

Details of Performance Analysis

B.1 Model Systems

The performance and scaling behaviour of the implementation is evaluated for different sets of molecular and periodic systems with examples shown in Figure B.1.

The molecular models are similar to those used by Sodt et al.[123] and consist of (i) alkane chains, (ii) H-terminated graphite sheets, and (iii) H-terminated diamond chunks. The alkane chains have the composition C_nH_{2n+2}, with $n = 10, 20, 40, 60, 120, 160, 200$ and the longest chain uses 5010 basis and 17024 auxiliary basis functions. The graphite sheets, $C_{16}H_{10}$, $C_{76}H_{22}$, $C_{102}H_{26}$, $C_{184}H_{34}$ and $C_{210}H_{38}$ contain up to 3340 basis and 13266 auxiliary basis functions. The diamond chunks have compositions $C_{11}H_{18}$, $C_{87}H_{64}$, $C_{168}H_{130}$ and $C_{246}H_{184}$. The largest chunk uses 4610 basis and 17214 auxiliary basis functions.

For 1D periodic calculations a series of single-walled carbon $(4, 4)$ armchair nanotubes (SWNT) is constructed. The unit cell of the smallest SWNT with length of 2.46 Å in periodic direction consists of 16 C atoms. The series uses doubled, tripled and quadrupled supercells. The largest supercell contains 960 basis and 3904 auxiliary basis functions.

2D periodic calculations are performed for models of the hydroxylated α-quartz (0001) surface. The hexagonal surface unit cell (lattice vector $a = 5.01$ Å) of the smallest model has the composition $Si_6O_{12}H_4$. The series consists of (1×1), (2×2), (3×3) and (4×4) surface supercells with the largest model using 5024 basis and 18528 auxiliary basis functions.

The 3D periodic model systems consist of (i) MgO supercells, (ii) supercells of NaCl with a chlorine vacancy (F-centre), (iii) hematite supercells with ferromagnetic spin configuration, and (iv) all-silica faujasite zeolite model. A series of MgO (1 × 1 × 1), (2 × 2 × 2), (3 × 3 × 3) and (4 × 4 × 4) supercells is constructed starting from the primitive unit cell containing one MgO unit ($a = b = c = 2.98$ Å and $\alpha = \beta = \gamma = 60°$). The largest supercell uses 2496 basis and 8320 auxiliary basis functions. The cubic unit cell of the smallest NaCl model (lattice vector $a = 5.62$ Å) has the composition Na_4Cl_4. The series uses (1 × 1 × 1), (2 × 2 × 2), (3 × 3 × 3) and (4 × 4 × 4) supercells with the largest model containing 11008 basis and 33792 auxiliary basis functions. For each size the corresponding model of F-centre is constructed by a removal of one Cl atom. In case of the (4 × 4 × 4) NaCl supercell this results in a system comprising 10985 basis and 33729 auxiliary basis functions. For hematite a series of (1 × 1 × 1), (2 × 2 × 2), (3 × 3 × 2), (3 × 3 × 3) and (4 × 4 × 4) supercells is constructed starting from the primitive unit cell ($a = b = c = 5.43$ Å and $\alpha = \beta = \gamma = 55.2°$) with the composition Fe_4O_6. The largest hematite model uses 19072 basis and 53632 auxiliary basis functions. For evaluation of the parallel performance of the implementation all-silica faujasite zeolite model constructed from the experimental crystal structure[14] is used. Its cubic unit cell with $a = 25.0$ Å shown in Figure B.1 contains 576 atoms, 9408 basis and 35520 auxiliary basis functions.

B.2 Methods and Basis Sets

All calculations employ the Becke-Perdew (BP86) exchange-correlation functional.[20,106] The performance and scaling behaviour is investigated using the split-valence plus polarization (def2-SVP) basis[116,147] and auxiliary basis[146] sets. For 3D periodic dense models (MgO, NaCl with F-centre and hematite) the pob-TZVP[105] basis sets along with appropriate auxiliary basis sets[146] are employed to avoid SCF convergence problems caused by small orbital exponents. The calculations are performed on the 2.40 GHz Intel Xeon E5-2695v2 CPU. Parallel efficiency is evaluated using up to 24 CPU cores. Timings for molecular systems (alkane chains, graphite sheets and diamond chunks) are obtained using a single CPU core. Calculations for the remaining systems are performed using 4 CPU cores. Calculations on the

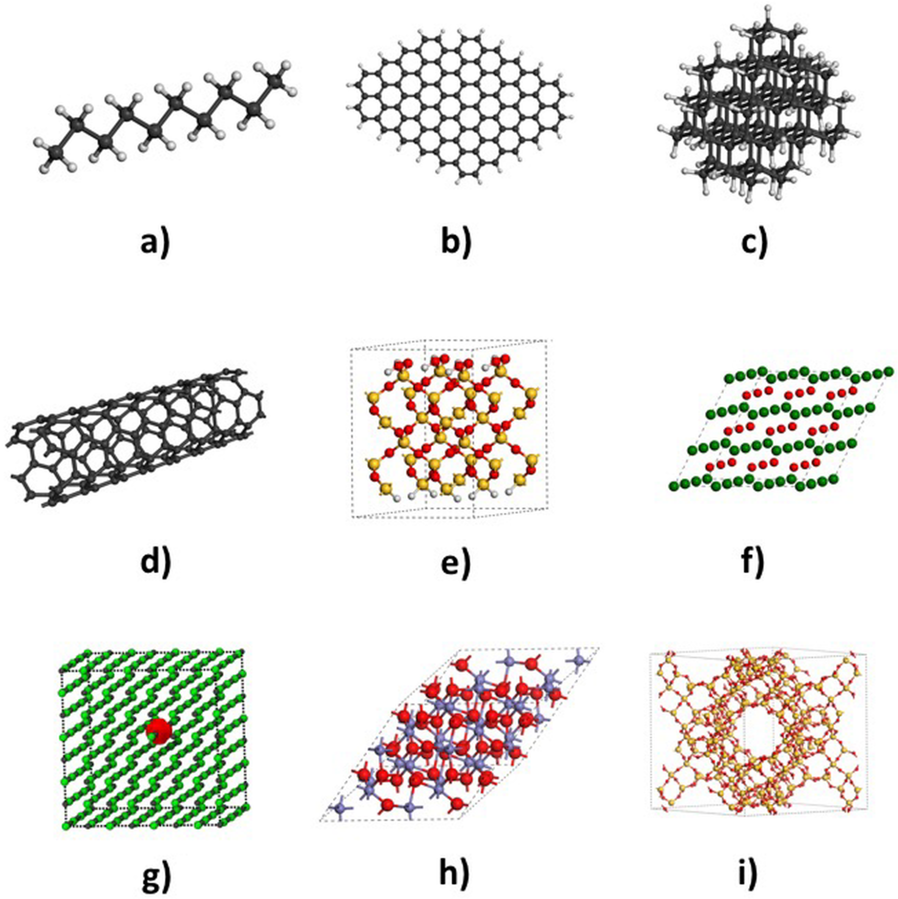

Figure B.1: Examples of test molecular and periodic systems: a) $C_{10}H_{22}$ alkane chain, b) H-terminated $C_{102}H_{26}$ graphite sheet, c) H-terminated $C_{87}H_{84}$ diamond chunk, d) 1D quadrupled supercell of $(4, 4)$ carbon nanotube $(C_{16})_n$, e) 2D 2×2 supercell of hydroxylated α-quartz (0001) $(Si_6O_{12}H_4)_n$ surface, f) 3D 3×3×3 supercell of MgO, g) 3D 4×4×4 supercell of NaCl $(Na_4Cl_4)_n$ containing a single Cl vacancy along with spin density isosurface, h) 3D 2×2×2 supercell of hematite $(Fe_4O_6)_n$, i) 3D all-silica faujasite $(Si_{192}O_{384})_n$.

F-centre and hematite models use spin unrestricted KS formalism. For remaining systems spin restricted calculations are performed. Unless stated otherwise, numerical integration of the exchange-correlation term uses grids of size 3.[28,133] DF-CFMM uses well-separateness criterion $ws = 3$, the order of multipole expansions $L = 20$, and the threshold $\varepsilon = 1 \times 10^{-9}$.[88,122] For all investigated systems these settings yield energies that differ from reference values ($ws = 4$, $L = 30$, $\varepsilon = 1 \times 10^{-11}$) by less than $10^{-6} E_{\mathrm{h}}$.

APPENDIX C

Computational Details

C.1 Vertical Detachment Energy

Vertical detachment energies (VDE) of all the clusters have been calculated as differences between energies of anionic and neutral species at the structure of the anion. During the PES experiment an electron can be ejected from one of the inner shells leaving an uncharged cluster in its excited singlet or triplet state. Related energies have been calculated as the energy differences between the ground state of M_n^- and vertical excited states of M_n (M = ZnO, CdO and TiO_2) on the corresponding structure of the anion. The lowest energy combined with corresponding VDE yields the values of HOMO–LUMO gaps for neutral clusters. The radiative decay times τ have been calculated from oscillator strength and energy of transition between ground and excited states (see ref. 65).

C.2 Methods for ZnO

In order to select the most suitable exchange-correlation functional vertical detachment energies (VDE), Zn-O bond lengths and vertical excitations energies of the three lowest excitations and the corresponding oscillator strengths have been calculated for the most stable structure of $(ZnO)_5^-$ (**5A**$^-$, fig. C.1) using the BLYP,[20,90] BP,[20,106] PBE,[107] B3LYP,[19,90] and BHLYP.[18,20,90] functionals along with the aug-cc-pV5Z[49] basis sets. The results are summarized in tabs. C.1 and C.2. For all the functionals the calculated excitation energies show only moderate variation of at most 0.28 eV. In contrast, the values of VDE vary by at most 0.6 eV. The best agreement of VDE with the experimental value of 1.8 eV is obtained for the PBE

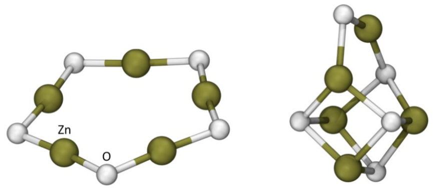

5A 5B

Figure C.1: Structures of the two most stable isomers of **5A**$^-$ $(ZnO)_5$ and $(ZnO)_5^-$ found by global structure optimization.

Table C.1: Vertical detachment energies (VDE) (eV) of along with Zn-O bond lengths (Å) in the ground states of **5A**$^-$ and **5A** calculated with various exchange-correlation functionals.

functional	VDE	Zn-O	
		5A$^-$	**5A**
BLYP	1.61	1.822	1.799
BP	1.91	1.810	1.783
PBE	1.82	1.812	1.785
B3LYP	1.49	1.805	1.781
BHLYP	1.31	1.791	1.769

functional, which is used through this work.

Tabs. C.3 and C.4 show the relative energies of the most stable structures of neutral (**5A** and **5B**, fig. C.1) and anionic (**5A**$^-$ and **5B**$^-$) clusters, VDEs of **5A**$^-$ and **5B**$^-$, vertical excitation energies and oscillator strengths for the three lowest energy excitations in **5A**$^-$, as well as Zn-O bond lengths in **5A** and **5A**$^-$ calculated using the def2-TZVPP,[147] def2-QZVPP,[147] aug-cc-pVTZ,[16,49,75] aug-cc-pVQZ[16,49,75] and aug-cc-pV5Z[16,49,75] basis sets. The Zn-O bond lengths and detachment energies show only a small variation of about 0.004 Å and 0.04 eV, respectively, between the different basis sets. With exception of the def2-TZVPP basis sets, the values of relative energies vary by at most 0.04 eV. Excitations energies and oscillator strengths of the three lowest excitations show only small variation between Dunning basis sets, but fully converged results are obtained only for the aug-cc-pV5Z basis sets.

Table C.2: Excitation energies (ΔE, eV) and oscillator strengths (f) for the lowest energy excitations in $(\mathrm{ZnO})_5^-$ calculated with various exchange-correlation functionals. The transition $a_1' \rightarrow a_1'$ is dipole forbidden ($f = 0$).

functional	$a_1' \rightarrow a_1'$	$D_0 \rightarrow D_1$		$D_0 \rightarrow D_2$	
	ΔE	ΔE	f	ΔE	f
BLYP	1.42	1.33	0.391	1.69	0.108
BP	1.43	1.52	0.280	1.64	0.07
PBE	1.35	1.43	0.275	1.57	0.079
B3LYP	1.38	1.36	0.386	1.55	0.116
BHLYP	1.49	1.50	0.366	1.48	0.122

Table C.3: Basis sets dependence of relative stabilities of anionic (ΔE(**5B**$^-$–**5A**$^-$)) and neutral (ΔE(**5B-5A**)) isomers of ZnO pentamer (fig. C.1) along with corresponding vertical detachment energies (VDE). All values in eV.

functional	ΔE(**5B**$^-$–**5A**)$^-$	ΔE(**5B**–**5A**)	VDE	
			5A$^-$	**5B**$^-$
def2-TZVPP	1.36	1.76	1.86	2.26
def2-QZVPP	1.52	1.93	1.82	2.23
aug-cc-pVTZ	1.55	1.95	1.84	2.25
aug-cc-pVQZ	1.55	1.97	1.82	2.24
aug-cc-pV5Z	1.55	1.97	1.82	2.24

The values of excitation energies calculated with the def2-TZVPP and def2-QZVPP basis sets are overestimated by up to 0.35 and 0.18 eV, respectively, compared to the Dunning basis sets. Similar calculations have been performed for structures of octamer and dodecamer, using the def2-QZVPP and aug-cc-pV5Z basis sets. Results summarized in tabs. C.5 and C.6 demonstrate that, in contrast to the calculated VDE, excitation energies and structural parameters show only a moderate variation between the two basis sets. Therefore, calculations for clusters larger than pentamer have been performed using the def2-QZVPP basis sets only.

Table C.4: Basis set dependence of the excitation energies (ΔE, eV) and oscillator strengths (f) of the three lowest excitations in **5A**$^-$ along with the Zn-O bond lengths (Å) in the ground states of **5A**$^-$and **5A**. The transition is dipole forbidden ($f = 0$).

basis	$a_1' \rightarrow a_1'$	$D_0 \rightarrow D_1$		$D_0 \rightarrow D_2$		Zn-O	
	Δ E	Δ E	f	Δ E	f	**5A**$^-$	**5B**$^-$
def2-TZVPP	1.54	1.68	0.216	1.92	0.045	1.816	1.787
def2-QZVPP	1.45	1.57	0.258	1.75	0.058	1.813	1.785
aug-cc-pVTZ	1.35	1.45	0.283	1.62	0.078	1.812	1.785
aug-cc-pVQZ	1.35	1.43	0.280	1.59	0.080	1.812	1.785
aug-cc-pV5Z	1.35	1.43	0.275	1.57	0.079	1.812	1.785

Table C.5: Basis set dependence of the vertical detachment energies (VDE), excitation energies (ΔE) and oscillator strengths of the two lowest excitations in **8A** and **8B**. All Zn-O bond lengths (Å) for **8A**$^-$ and **8A**, and the shortest one for **8B**$^-$ and **8B**. Energies in eV.

structure	basis	VDE	$D_0 \rightarrow D_1$		$D_0 \rightarrow D_2$		Zn-O	
			ΔE	f	ΔE	f	anionic	neutral
8A	def2-QZVPP	1.97	1.48	0.110	1.51	0.357	1.881 2.193	1.865 2.198
	aug-cc-pV5Z	1.98	1.45	0.121	1.48	0.378	1.880 2.195	1.864 2.199
8B	def2-QZVPP	2.12	1.24	0.166	1.56	0.092	1.898	1.883
	aug-cc-pV5Z	2.13	1.23	0.171	1.54	0.099	1.897	1.883

Table C.6: Basis set dependence of the vertical detachment energies (VDE), excitation energies (ΔE) and oscillator strengths of the two lowest excitations in $(\mathrm{ZnO})_{12}^{-}$. The $a_g \rightarrow a_g$ excitation is dipole forbidden ($f = 0$). Zn-O bond lengths in Å, energies in eV.

basis	VDE	$D_0 \rightarrow D_1$		$a_g \rightarrow a_g$	Zn-O	
		ΔE	f	ΔE	$(\mathrm{ZnO})_{12}^{-}$	ZnO_{12}
def2-QZVPP	2.22	1.47	0.455	1.82	1.886, 1.978	1.875, 1.969
aug-cc-pV5Z	2.22	1.46	0.480	1.80	1.885, 1.978	1.875, 1.969

C.3 Methods for CdO

For consistency with the ZnO case, the PBE exchange-correlation functional along with the def2-QZVPP basis set is used for all calculations. For Cd atoms, the ecp-28-mwb[11] effective core potential (ECP) is used. It has been checked that unlike in the case of ZnO the effects of increasing the basis set size beyond def2-QZVPP are negligible already for the smallest examined cluster.

C.4 Methods for Mixed ZnO - $\mathrm{TiO_2}$ Materials

In order to select the most suitable exchange-correlation functional vertical (VDE) and adiabatic (ADE) detachment energies along with HOMO–LUMO gaps have been calculated for the most stable structures of (n = 1–3, see fig. 3.10) refined using PBE and PBE0 functionals along with def2-QZVPP basis set. The results are summarized in tab. C.7, along with experimental values reported by Zhai and Wang.[156] Values calculated using both functionals show a significant variation up to 0.58 eV for detachment energies and 1.25 eV for HOMO-LUMO gaps. The results for structures 2C and 3A obtained at PBE0/def2-QZVPP are in very good agreement with the experiment. In case of the monomer the PBE0/def2-QZVPP calculations well reproduce detachment energies albeit overestimate the HOMO-LUMO gap. For **1A** results obtained with PBE functional are in good agreement with the experiment. On the contrary, for dimer and trimer at least one of the calculated values

Table C.7: Vertical (VDE) and adiabatic (ADE) detachment energies along with HOMO–LUMO gap (ΔE) of the most stables isomers of (n = 1–3). Results obtained with PBE and PBE0 functionals, along with experimental values reported by Zhai et. al.[156] All values in eV.

structure	VDE			ADE			ΔE		
	PBE	PBE0	exp	PBE	PBE0	exp	PBE	PBE0	exp
1	1.48	1.54	1.59	1.52	1.59	1.59	2.09	2.78	2.22
2A	1.66	1.62		1.92	2.17		2.75	3.22	
2B	1.92	1.86	2.06	2.18	2.18	2.27	2.46	3.19	2.59
2C	1.90	2.03		2.08	2.30		2.06	2.59	
3A	2.69	2.92	2.78	2.99	3.38	3.15	1.05	2.30	2.26
3B	2.05	2.03		2.21	2.79		2.74	3.02	

is far from the experimental one, regardless of the choice of the isomer. Therefore, PBE0 functional has been employed through this work. Good agreement between calculated and experimental energies for structure **2C** shows that the selected functional reproduces cluster energies, however may fail to unambiguously point the energetically lowest structure. Hence calculations for several most stable isomers are run for every cluster.

For examination of ZnO adsorption on anatase (101) surface the PBE exchange-correlation functional is used for consistency with the case of ZnO clusters. The pob-TZVP[105] basis sets are employed to avoid SCF convergence problems caused by small orbital exponents in periodic systems.

Bibliography

[1] TURBOMOLE developer version, a development of University of Karlsruhe and Forschungszentrum Karlsruhe GmbH, 1989-2007, TURBOMOLE GmbH, since 2007; available from `http://www.turbomole.com`.

[2] OpenMP Architecture Review Board, "OpenMP Application Program Interface, Version 4.0", July 2013. `http://www.openmp.org`.

[3] BLAS (Basic Linear Algebra Subprograms). `http://www.netlib.org/blas`.

[4] C. Adamo and V. Barone. Toward reliable density functional methods without adjustable parameters: The PBE0 model. *J. Chem. Phys.*, 110(13):6158–6170, 1999.

[5] R. Ahlrichs, M. Bär, M. Häser, H. Horn, and C. Kölmel. Electronic structure calculations on workstation computers: The program system turbomole. *Chem. Phys. Lett.*, 162(3):165–169, 1989.

[6] A. A. Al-Sunaidi, A. A. Sokol, C. R. A. Catlow, and S. M. Woodley. Structures of zinc oxide nanoclusters: As found by revolutionary algorithm techniques. *J. Phys. Chem. C*, 112(48):18860–18875, 2008.

[7] T. Albaret, F. Finocchi, and C. Noguera. Density functional study of stoichiometric and O-rich titanium oxygen clusters. *J. Chem. Phys.*, 113(6):2238–2249, 2000.

[8] A. Alvarez-Ibarra and A. M. Köster. A new mixed self-consistent field procedure. *Mol. Phys.*, 113(19-20):3128–3140, 2015.

[9] A. Amat and F. De Angelis. Challenges in the simulation of dye-sensitized ZnO solar cells: Quantum confinement, alignment of energy levels and excited state nature at the dye/semiconductor interface. *Phys. Chem. Chem. Phys .*, 14(30):No. 10662, 2012.

[10] S. Anandan, A. Vinu, T. Mori, N. Gokulakrishnan, P. Srinivasu, V. Murugesan, and K. Ariga. Photocatalytic degradation of 2,4,6-trichlorophenol using lanthanum doped ZnO in aqueous suspension. *Catal. Commun.*, 8(9):1377–1382, 2007.

[11] D. Andrae, U. Haussermann, M. Dolg, H. Stoll, and H. Preuss. Energy-adjusted abinitio pseudopotentials for the second and third row transition elements. *Theor. Chim. Acta*, 77(2):123–141, 1990.

[12] J. M. Azpiroz, I. Infante, X. Lopez, J. M. Ugalde, and F. De Angelis. A first-principles study of II–VI (II = Zn; VI = O, S, Se, Te) semiconductor nanostructures. *J. Mater. Chem.*, 22(40):21453–21465, 2012.

[13] E. J. Baerends, D. E. Ellis, and P. Ros. Self-consistent molecular Hartree–Fock–Slater calculations I. The computational procedure. *Chem. Phys.*, 2:41–51, 1973.

[14] C. Baerlocher, W. M. Meier, and D. H. Olson. *Atlas of Zeolite Framework Types*. Elsevier, Amsterdam, 6 edition, 2007.

[15] J. Baker, J. Andzelm, A. Scheiner, and B. Delley. The effect of grid quality and weight derivatives in density functional calculations. *J. Chem. Phys.*, 101(10):8894–8902, 1994.

[16] N. B. Balabanov and K. A. Peterson. Systematically convergent basis sets for transition metals. I. All-electron correlation consistent basis sets for the 3d elements Sc-Zn. *J. Chem. Phys.*, 123(6):No. 064107, 2005.

[17] O. P. Balaj, I. Balteanu, T. T. J. Rossteuscher, M. K. Beyer, and V. E. Bondybey. Catalytic oxidation of CO with N_2O on gas-phase platinum clusters. *Angew. Chem., Int. Ed.*, 43(47):6519–6522, 2004.

[18] A. D. Becke. A new mixing of Hartree–Fock and local density-functional theories. *J. Chem. Phys.*, 98(2):1372–1377, 1983.

[19] A. D. Becke. Density-functional thermochemistry .3. The role of exact exchange. *J. Chem. Phys.*, 98(7):5648–5652, 1983.

[20] A. D. Becke. Density-functional exchange-energy approximation with correct asymptotic behavior. *Phys. Rev. A*, 38(6):3098–3100, 1988.

[21] A. D. Becke. A multicenter numerical integration scheme for polyatomic molecules. *J. Chem. Phys.*, 88(4):2547–2553, 1988.

[22] E. Berardo, H. S. Hu, H. J. J. van Dam, S. A. Shevlin, S. M. Woodley, K. Kowalski, and M. A. Zwijnenburg. Describing excited state relaxation and localization in TiO_2 nanoparticles using TD-DFT. *J. Chem. Theory Comput.*, 10(12):5538–5548., 2014.

[23] V. Blum, R. Gehrke, F. Hanke, P. Havu, V. Havu, X. Ren, K. Reuter, and M. Scheffler. Ab initio molecular simulations with numeric atom-centered orbitals. *Comput. Phys. Commun.*, 180(11):3172–3191, 2009.

[24] J. Boström, F. Aquilante, T. B. Pedersen, and R. Lindh. Analytical gradients of Hartree–Fock exchange with density fitting approximations. *J. Chem. Theory Comput.*, 9(1):204–212, 2013.

[25] C. Braun, S. Pietsch, S. Proch, Y. D. Kim, and G. F. Ganteför. Relaxation dynamics of the mass-selected hydrated auride ion (Au^-). *Chem. Phys. Lett.*, 588(1):27–30, 2013.

[26] C. Braun, S. Proch, H. O. Seo, Y. D. Kim, and G. F. Ganteför. Studies of femtosecond time-resolved photoelectron spectroscopy of Au_3^- $(H_2O)_m$ clusters: Alteration of cluster relaxation dynamics of metal clusters by water molecules. *Chem. Phys. Lett.*, 530(1):35–38, 2012.

[27] J. C. Burant, M. C. Strain, G. E. Scuseria, and M. J. Frisch. Analitic energy gradients for the Gaussian very fast multipole method (GvFMM). *Chem. Phys. Lett.*, 248(1–2):43–49, 1996.

[28] A. M. Burow and M. Sierka. Linear scaling hierarchical integration scheme for the exchange-correlation term in molecular and periodic systems. *J. Chem. Theory Comput.*, 7(10):3097–3104, 2011.

[29] A. M. Burow, M. Sierka, and F. Mohamed. Resolution of identity approximation for the Coulomb term in molecular and periodic systems. *J. Chem. Phys.*, 131(21):No. 214101, 2009.

[30] M. Calatayud, L. Maldonado, and C. Minot. Reactivity of $(TiO_2)_n$ clusters (n = 1–10): Probing gas-phase acidity and basicity properties. *J. Phys. Chem. C*, 112(41):16087–16095, 2008.

[31] P. Čársky, R. Čurik, and Š. Varga. Efficient evaluation of Coulomb integrals in a mixed Gaussian and plane-wave basis using the density fitting and Cholesky decomposition. *J. Chem. Phys*, 136(11):114105, 2012.

[32] A. W. Jr. Castleman, S. N. Khanna, A. Sen, A. C. Reber, M. Qian, K. M. Davis, S. J. Peppernick, A. Ugrinov, and M. D. Merritt. From designer clusters to synthetic crystalline nanoassemblies. *Nano Lett.*, 7(9):2734–2741, 2007.

[33] C. R. A. Catlow, Z. X. Guo, M. Miskufova, S. A. Shevlin, A. G. H. Smith, A. A. Sokol, A. Walsh, D. J. Wilson, and S. M. Woodley. Advances in computational studies of energy materials. *Philos. T. R. Soc. A*, 368(1923):3379–3456, 2010.

[34] A. Cedillo, J. Robles, and J. L. Gazquez. New nonlocal exchange-energy functional from a kinetic-energy-density Pade-approximant model. *Phys. Rev. A*, 38(4):1697–1701, 1988.

[35] G. V. Chertihin and L. Andrews. Reactions of laser ablated titanium, zirconium, and hafnium atoms with oxygen molecules in condensing argon. *J. Phys. Chem.*, 99(17):6356–6366, 1995.

[36] K.-C. Chiu, J.-S. Wang, and C.-Y. Lin. Temperature dependence of the band gap in C_{60} crystals. *Appl. Phys.*, 79(3):1784–1787, 1996.

[37] S. A. Claridge, S. N. Castleman, A. W., Jr. Khanna, C. B. Murray, A. Sen, and P. S. Weiss. Cluster-assembled materials. *ACS Nano*, 3(2):244–255, 2009.

[38] A. Costales, M. A. Blanco, E. Francisco, R. Pandey, and A. M. Pendás. Evolution of the properties of Al_nN_n clusters with size. *J. Phys. Chem. B*, 109(51):24352–24360, 2005.

[39] A. Costales, M. A. Blanco, E. Francisco, A. M. Pendás, and Ravindra Pandey. First principles study of neutral and anionic (medium-size) aluminum nitride clusters: $\mathrm{Al}_n\mathrm{N}_n$, $n = 7$–16. *J. Phys. Chem. B*, 110(9):4092–4098, 2006.

[40] D. M. Cox, R. Brickman, K. Creegan, and A. Kaldor. Gold clusters: Reactions and deuterium uptake. *Z. Phys. D: At., Mol. Clusters*, 19(4):353–355, 1991.

[41] F. De Angelis and L. Armelao. Optical properties of ZnO nanostructures: a hybrid DFT/TDDFT investigation. *Phys. Chem. Chem. Phys.*, 13(2):467–475, 2012.

[42] W. A. de Heer. The physics of simple metal clusters: Experimental aspects and simple models. *Rev. Mod. Phys.*, 65(3):611–676, 1993.

[43] P. Deglmann, F. Furche, and R. Ahlrichs. An efficient implementation of second analytical derivatives for density functional methods. *Chem. Phys. Lett.*, 362(5-6):511–518, 2002.

[44] P. Deglmann, K. May, F. Furche, and R. Ahlrichs. Nuclear second analytical derivative calculations using auxiliary basis set expansions. *Chem. Phys. Lett.*, 384(1-3):103–107, 2004.

[45] U. Diebold. The surface science of titanium dioxide. *Surf. Sci. Rep.*, 48(5-8):53–229, 2003.

[46] R. Dovesi, R. Orlando, A. Erba, C. M. Zicovich-Wilson, B. Civalleri, S. Casassa, L. Maschio, M. Ferrabone, M. De La Pierre, P. D'Arco, Y. Noël, M. Causà, M. Rérat, and B. Kirtman. CRYSTAL14: A program for the ab initio investigation of crystalline solids. *Int. J. Quantum Chem.*, 114(19):1287–1317, 2014.

[47] B. I. Dunlap, J. W. D. Connolly, and J. R. Sabin. On some approximations in applications of Xα theory. *J. Chem. Phys.*, 71(8):3396–3402, 1979.

[48] B. I. Dunlap, N. Rosch, and S. B. Trickey. Variational fitting methods for electronic structure calculations. *Mol. Phys.*, 108(21-23):3167–3180, 2010.

[49] T. H. Dunning. Gaussian-basis sets for use in correlated molecular calculations. 1. the atoms boron through neon and hydrogen. *J. Chem. Phys.*, 90(2):1007–1023, 1989.

[50] O. T. Ehrler, J. P. Yang, C. Hättig, A.-N. Unterreiner, H. Hippler, and M. M. Kappes. Femtosecond pump/probe photoelectron spectroscopy of isolated C_{60} negative ions. *J. Chem. Phys.*, 125(7):No. 074312, 2006.

[51] K. Eichkorn, O. Treutler, H. Öhm, M. Häser, and R. Ahlrichs. Auxiliary basis-sets to approximate Coulomb potentials. *Chem. Phys. Lett.*, 242(6):625–660, 1995.

[52] R. A. Evarestov. *Quantum Chemistry of Solids*, volume 153. Springer, Berlin, 2012.

[53] P. P. Ewald. Die berechnung optischer und elektrostatischer gitterpotentiale. *Ann. Phys.*, 369(1):253–287, 1921.

[54] C. A. Fancher, H. L. de Clercq, O. C. Thomas, D. W. Robinson, and K. H. Bowen. Zinc oxide and its anion: A negative ion photoelectron spectroscopic study. *J. Chem. Phys.*, 109(19):8426–8429, 1998.

[55] A. Fernandez-Garcia, M. andMartinez-Arias, J. C. Hanson, and J. A. Rodriguez. Nanostructured oxides in chemistry: Characterization and properties. *Chem. Rev.*, 104(9):4063–4104, 2004.

[56] R. Fournier, J. Andzelm, and D. R. Salahub. Analytical gradient of the linear combination of gaussian-type orbitals local spin-density energy. *J. Chem. Phys*, 90(11):6371–6377, 1989.

[57] S. K. Ghosh and R. G. Parr. Phase-space approach to the exchange-energy functional of density-functional theory. *Phys. Rev. A*, 34(2):785–791, 1986.

[58] S. Goedecker. Linear scaling electronic structure methods. *Rev. Mod. Phys.*, 71(4):1085–1123, 1999.

[59] X.-Q. Gong, A. Selloni, M. Batzill, and U. Diebold. Steps on anatase TiO_2 (101). *Nat. Mater.*, 5(8):665–670, 2006.

[60] K. D. Gunaratne, C. Berkdemir, C. L. Harmon, and A. W., Jr. Castleman. Investigating the relative stabilities and electronic properties of small zinc oxide clusters. *J. Phys. Chem. A*, 116(51):12429–12437, 2012.

[61] S. Hamad, C. R. A. Catlow, E. Spano, J. M. Matxain, and J. M. Ugalde. Structure and Ppoperties of ZnS nanoclusters. *J. Phys. Chem. B*, 109(7):2703–2709, 2005.

[62] J. Heinzelmann, A. Koop, S. Proch, G. F. Ganteför, R. Łazarski, and M. Sierka. Cage-like nanoclusters of ZnO probed by time-resolved photoelectron spectroscopy and theory. *J. Phys. Chem. Lett.*, 5(15):2642–2648, 2014.

[63] F. Herman, J. P. Van Dyke, and I. B. Ortenburger. Improved statistical exchange approximation for inhomogeneous many-electron systems. *Phys. Rev. Lett.*, 22(16):807–811, 1969.

[64] J. Heyd, J. E. Peralta, G. E. Scuseria, and R. L. Martin. Energy band gaps and lattice parameters evaluated with the Heyd–Scuseria–Ernzerhof screened hybrid functional. *J. Chem. Phys.*, 123(17):No. 174101, 2005.

[65] R. C. Hilborn. Einstein coefficients, cross sections, f values, dipole moments, and all that. Available from `http://arxiv.org/abs/physics/0202029`.

[66] A. F. Izmaylov and G. E. Scuseria. Resolution of the identity atomic orbital Laplace transformed second order Møller-Plesset theory for nonconducting periodic systems. *Phys. Chem. Chem. Phys.*, 10(23):3421–3429, 2008.

[67] J. E. Jaffe and A. C. Hess. Gaussian basis density functional theory for systems periodic in two or three dimensions: Energy and forces. *J. Chem. Phys.*, 105(24):10983–10998, 1996.

[68] P. Jena and A. W. Jr. Castleman. *Nanoclusters: A Bridge across Disciplines.* Elsevier, Amsterdam, 2010.

[69] B. G. Johnson and M. J. Frisch. An implementation of analytic 2nd derivatives of the gradient-corrected density-functional energy. *J. Chem. Phys.*, 100(10):7429–7442, 1994.

[70] B. G. Johnson, P. M. W. Gill, and J. A. Pople. The performance of a family of density functional methods. *J. Chem. Phys.*, 98(7):5612–5626, 1993.

[71] Y. Jung, A. Sodt, P. M. W. Gill, and M. Head-Gordon. Auxiliary basis expansions for large-scale electronic structure calculations. *Proc. Natl. Acad. Sci. U. S. A.*, 102(19):6692–6697, 2005.

[72] P. V. Kamat, K. Tvrdy, D. R. Baker, and J. G. Radich. Beyond photovoltaics: Semiconductor nanoarchitectures for liquid-junction solar cells. *Chem. Rev.*, 110(11):6664–6688, 2010.

[73] S. H. Kang, W. Lee, Y. C. Nah, K. S. Lee, and H. S. Kim. Synthesis of nanobranched TiO_2 nanotubes and their application to dye-sensitized solar cells. *Curr. Appl. Phys.*, 13(1):252–255, 2013.

[74] L. Kavan, M. Grätzel, S. E. Gilbert, C. Klemenz, and H. J. Scheel. Electrochemical and photoelectrochemical investigation of single-crystal anatase. *J. Am. Chem. Soc.*, 118(28):6716–6723, 1996.

[75] R. A. Kendall, T. H. Dunning, and R. J Harrison. Electron-affinities of the 1st-row atoms revisited — Systematic basis-sets and wave-functions. *J. Chem. Phys.*, 96(9):6796–6806, 1992.

[76] H. Kietzmann, R. Rochow, G. F. Ganteför, W. Eberhardt, K. Vietze, G. Seifert, and P. W. Fowler. The electronic structure of small fullerens: Evidence for a high stability of C_{32}. *Phys. Rev. Lett.*, 81(24):5378–5381, 1998.

[77] A. Komornicki and G. Fitzgerald. Molecular gradients and hessians implemented in density functional theory. *J. Chem. Phys.*, 98:1398–1421, 1993.

[78] L. Koponen, L. Tunturivuori, M. J. Puska, and R. M. Nieminen. Photoabsorption spectra of boron nitride fullerenelike structures. *J. Chem. Phys.*, 126(21):No. 214306, 2007.

[79] K. Koyasu, C. Braun, S. Proch, and G. F. Gantefoer. The metal-semiconductor transition monitored by excited state lifetimes of $Al_4O_m^-$ clusters. *Clusters. Appl. Phys. A: Mater. Sci. Process.*, 100(2):431–436, 2010.

[80] K. Koyasu, K. Komatsu, and F. Misaizu. Zinc oxide cluster cations: Smallest tube like structure at $(ZnO)_6^+$. *J. Chem. Phys.*, 139(16):No. 164308, 2013.

[81] W. Krätschmer, L. D. Lamb, K. Fostiropoulos, and D. R. Huffman. Solid C_{60}: a new form of carbon. *Nature*, 347(6291):354–358, 1990.

[82] G. Kresse and J. Furthmüller. Efficiency of ab-initio total energy calculations for metals and semiconductors using a plane-wave basis set. *Comput. Mat. Sci.*, 6(1):15–50, 1996.

[83] K. N. Kudin and G. E. Scuseria. A fast multipole algorithm for the efficient treatment of the Coulomb problem in electronic structure calculations of periodic systems with Gaussian orbitals. *Chem. Phys. Lett.*, 289(5–6):611–616, 1998.

[84] K. N. Kudin and G. E. Scuseria. A fast multipole method for periodic systems with arbitrary unit cell geometries. *Chem. Phys. Lett.*, 283(1):61–68, 1998.

[85] K. N. Kudin and G. E. Scuseria. Linear-scaling density-functional theory with Gaussian orbitals and periodic boundary conditions: Efficient evaluation of energy and forces via the fast multipole method. *Phys. Rev. B*, 61(24):16440–16453, 2000.

[86] K. N. Kudin and G. E. Scuseria. Revisiting infinite lattice sums with the periodic fast multipole method. *J. Chem. Phys.*, 121:2886–2890, 2004.

[87] S. M. Lang, I. Fleischer, T. M. Bernhardt, R. N. Barnett, and U. Landman. $Pd_6O_4^+$: An oxidation resistant yet highly catalytically active nano-oxide cluster. *J. Am. Chem. Soc.*, 134(51):20654–20659, 2012.

[88] R. Łazarski, A. M. Burow, and M. Sierka. Density functional theory for molecular and periodic systems using density fitting and continuous fast multipole methods. *J. Chem. Theory Comput.*, 11(7):3029–3041, 2015.

[89] R. Łazarski, A. M. Burow, and M. Sierka. Density functional theory for molecular and periodic systems using density fitting and continuous fast multipole method: analytical gradients. *J. Comp. Chem.*, 37(28):2518–2526, 2016.

[90] C. T. Lee, W. T. Yang, and R. G. Parr. Development of the Colle-Salvetti correlation-energy formula into a functional of the electron-density. *Phys. Rev. B*, 37(2):785–789, 1988.

[91] S. G. Li and D. A. Dixon. Molecular structures and energetics of the $(TiO_2)_n$ (n = 1–4) clusters and their anions. *J. Phys. Chem. A*, 112(29):6646–6666, 2008.

[92] G. Lippert, J. Hutter, and M. Parrinello. A hybrid Gaussian and plane wave density functional scheme. *Mol. Phys.*, 92(3):477–487, 1997.

[93] L. Ma, J. Wang, and G. Wang. Search for global minimum geometries of medium sized Cd_nTe_n clusters (n = 15, 16, 20, 24 and 28). *Chem. Phys. Lett.*, 552(1):73–77, 2012.

[94] L. Maschio and D. Usvyat. Fitting of local densities in periodic systems. *Phys. Rev. B*, 78(7):No. 073102, 2008.

[95] J. M. Matxain, J. M. Mercero, J. E. Fowler, and J. M. Ugalde. Clusters of group II-VI materials: Cd_iO_i ($i \leq 15$). *J. Phys. Chem. A*, 107(46):9918–9923, 2003.

[96] J. M. Matxain, J. M. Mercero, J. E. Fowler, and J. M. Ugalde. Electronic excitation energies of Zn_iO_i clusters. *J. Am. Chem. Soc.*, 125(31):9494–9499, 2003.

[97] J. M. Matxain, M. Piris, X. Lopez, and J. M. Ugalde. Thermally stable solids based on endohedrally doped zns clusters. *Chem. Eur. J.*, 15(20):5138 – 5144, 2009.

[98] J. M. Matxain, J. M. Ugalde, M. D. Towler, and R. J. Needs. Stability and aromaticity of B_iN_i rings and fullerenes. *J. Phys. Chem. A*, 107(46):10004–10010, 2003.

[99] N. Memarian, I. Concina, A. Braga, S. M. Rozati, A. Vomiero, and G. Sberveglieri. Hierarchically assembled ZnO nanocrystallites for high-efficiency dye-sensitized solar cells. *Angew. Chem., Int. Ed.*, 50(51):12321–12325, 2011.

[100] H. J. Monkhorst and J. D. Pack. Special points for Brillouin-zone integrations. *Phys. Rev. B*, 13(12):5188–5192, 1976.

[101] P. Murugan, V. Kumar, Y. Kawazoe, and N. Ota. Bonding nature and magnetism in small MoX_2 ($X = O$ and S) clusters — a comparative study by first principles calculations. *Chem. Phys. Lett.*, 423(1–3):202–207, 2006.

[102] S. P. Nanavati, V. Sundararajan, S. Mahamuni, V. Kumar, and S. V. Ghaisas. Optical properties of zinc selenide clusters from first-principles calculations. *Phys. Rev. B*, 80(24):No. 245417, 2009.

[103] C. A. Nelson, N. R. Monahan, and X. Y. Zhu. Exceeding the shockley-queisser limit in solar energy conversion. *Energy Environ. Sci.*, 6(12):3508–3519, 2013.

[104] Y. J. Oh, Lee I.-H., S. Kim, J. Lee, and K. J. Chang. Dipole-allowed direct band gap silicon superlattices. *Sci. Rep.*, 5(1):No. 37096, 2015.

[105] M. F. Peintinger, D. V. Oliviera, and T. Bredov. Consistent Gaussian basis sets of triple-zeta valence with polarization quality for solid-state calculations. *J. Comput. Chem.*, 34(6):451–459, 2013.

[106] J. P. Perdew. Density-functional approximation for the correlation-energy of the inhomogeneous electron-gas. *Phys. Rev. B*, 33(12):8822–8824, 1986.

[107] J. P. Perdew, K. Burke, and M. Ernzerhof. Generalized gradient approximation made simple. *Phys. Rev. Lett.*, 77(18):3865–3868, 1996.

[108] J. P. Perdew and M. Levy. Physical content of the exact Kohn–Sham orbital energies: Band gaps and derivative discontinuities. *Phys. Rev. Lett.*, 51(20):1884–1887, 1983.

[109] J. P. Perdew and W. Yue. Accurate and simple density functional for the electronic exchange energy: Generalized gradient approximation. *Phys. Rev. B*, 33(12):8800–8802, 1986.

[110] W. Pipornpong and V. Ruangpornvisuti. First-principles investigation of ZnO sodalite-like cage binding onto TiO_2 (001) surface and its ability for CO oxidation to CO_2. *J. Mater. Sci.*, 49(21):76200–7624, 2014.

[111] C. Pisani and R. Dovesi. Exact-exchange Hartree-Fock calculations for periodic systems. I. Illustration of the method. *Int. J. Quantum Chem.*, 17(3):501–516, 1980.

[112] J. A. Pople, P. M. W. Gill, and B. G. Johnson. Kohn-Sham density-functional theory within a finite basis set. *Chem. Phys. Lett.*, 199(6):557–560, 1992.

[113] P. Pulay. Ab-initio calculation of force constants and equilibrium geometries in polyatomic molecules I. Theory. *Theory. Mol. Phys.*, 17(2):197–204, 1969.

[114] A. C. Reber, S. N. Khanna, J. S. Hunjan, and M. R. Beltran. Rings, towers, cages of ZnO. *Eur. Phys. J. D*, 43(1-3):221–224, 2007.

[115] I. A. Sarsari, S. J. Hashemifar, and H. Salamati. First-principles study of ring to cage structural crossover in small ZnO clusters. *J. Phys.: Condens. Matter*, 24(50):No. 505502., 2012.

[116] A. Schäfer, H. Horn, and R. Ahlrichs. Fully optimized contracted Gaussian basis sets for atoms Li to Kr. *J. Chem. Phys.*, 97(4):2571–2577, 1992.

[117] G. Seifert, P. W. Fowler, D. Mitchell, D. Porezag, and T. Frauenheim. Boron-nitrogen analogues of the fullerenes: Electronic and structural properties. *Chem. Phys. Lett.*, 268(5-6):352–358, 1997.

[118] A. Selloni. Crystal growth — Anatase shows its reactive side. *Nat. Mater.*, 7(8):613–615, 2008.

[119] Y. H. Shao, C. A. White, and M. Head-Gordon. Efficient evaluation of the Coulomb force in density-functional theory calculations. *J. Chem. Phys.*, 114(15):6572–6577, 2001.

[120] S. R. Shirsath, D. V. Pinjari, P. R. Gogate, S. H. Sonawane, and A. B. Pandit. Ultrasound assisted synthesis of doped TiO_2 nano-particles: Characterization and comparison of effectiveness for photocatalytic oxidation of dyestuff effluent. *Ultrason. Sonochem.*, 20(1):277–286, 2013.

[121] M. Sierka. Synergy between theory and experiment in structure resolution of low-dimensional oxides. *Prog. Surf. Sci.*, 85(9-12):398–434, 2010.

[122] M. Sierka, A. Hogekamp, and R. Ahlrichs. Fast evaluation of the Coulomb potential for electron densities using multipole accelerated resolution of identity approximation. *J. Chem. Phys.*, 118(20):9136–9148, 2003.

[123] A. Sodt, J. E. Subotnik, and M. Head-Gordon. Linear scaling density fitting. *J. Chem. Phys.*, 125(19):No. 194109, 2006.

[124] R. Srinivasaraghavan, R. Chandiramouli, B. G. Jeyaprakash, and S. Seshadri. Quantum chemical studies on CdO nanoclusters stability. *Spectrochim. Acta A*, 102(1):242–249, 2013.

[125] M. C. Strain, G. E. Scuseria, and M. J. Frisch. Achieving linear scaling for the electronic quantum Coulomb problem. *Science*, 271(5245):51–53, 1996.

[126] R. E. Stratmann, G. E. Scuseria, and M. J. Frisch. Achieving linear scaling in exchange-correlation density functional quadratures. *Chem. Phys. Lett.*, 257(3–4):213–223, 1996.

[127] D. L. Strout. Structure and stability of boron nitrides: isomers of $B_{12}N_{12}$. *J. Phys. Chem. A*, 104(15):3364–3366, 2000.

[128] D. L. Strout. Structure and stability of boron nitrides: The crossover between rings and cages. *J. Phys. Chem. A*, 105(1):261–263, 2000.

[129] Y. M. Sun, J. H. Seo, C. J. Takacs, J. Seifter, and A. J. Heeger. Inverted polymer solar cells integrated with a low-temperature-annealed sol-gel-derived ZnO film as an electron transport layer. *Adv. Mater.*, 23(14):1679–1683, 2011.

[130] J. M. Tao, J. P. Perdew, V. N. Staroverov, and G. E. Scuseria. Climbing the density functional ladder: Nonempirical meta-generalized gradient approximation designed for molecules and solids. *Phys. Rev. Lett.*, 91(14):146401, 2003.

[131] M. Tobita, S. Hirata, and R. J. Bartlett. The analytical energy gradient scheme in the Gaussian based Hartree-Fock and density functional theory for two-dimensional systems using the fast multipole method. *J. Chem. Phys.*, 118(13):5776–5792, 2003.

[132] M. D. Towler, A. Zupan, and M. Causà. Density functional theory in periodic systems using local Gaussian basis sets. *Comput. Phys. Commun.*, 98(1):181–205, 1996.

[133] O. Treutler and R. Ahlrichs. Efficient molecular numerical integration schemes. *J. Chem. Phys.*, 102:346–354, 1995.

[134] M. C. Troparevsky, L. Kronik, and J. R. Chelikowsky. Structural and electronic properties of CdS and CdSe clusters. *J. Chem. Phys.*, 114(2):943–949, 2001.

[135] M. C. Troparevsky, L. Kronik, and J. R. Chelikowsky. Ab initio absorption spectra of CdSe clusters. *Phys. Rev. B*, 65(3):No. 033311, 2002.

[136] E. V. Trushin, I. L. Zilberberg, and A. V. Bulgakov. Structure and stability of small zinc oxide clusters. *Phys. Solid State*, 54(4):859–865, 2012.

[137] O. Vahtras, J. Almlöf, and M. W. Feyereisen. Integral approximations for LCAO-SCF calculations. *Chem. Phys. Lett.*, 213(5–6):514–518, 1993.

[138] J. VandeVondele, M. Krack, F. Mohamed, M. Parrinello, T. Chassaing, and J. Hutter. QUICKSTEP: Fast and accurate density functional calculations

using a mixed Gaussian and plane waves approach. *Comput. Phys. Commun.*, 162(11):103–128, 2005.

[139] Š. Varga. Long-range analysis of density fitting in extended systems. *Int. J. Quantum Chem.*, 108(9):1518–1527, 2008.

[140] S. H. Vosko, L. Wilk, and M. Nusair. Accurate spin-dependent electron liquid correlation energies for local spin-density calculations — a critical analysis. *Can. J. Phys.*, 58(8):1200–1211, 1980.

[141] M. Walter, H. Hakkinen, J. Stanzel, M. Neeb, and W. Eberhardt. Symmetry-induced long-lived excited state in Au_6^-. *Phys. Rev. B*, 76(15):No. 155422, 2007.

[142] B. L. Wang, S. Nagase, J. J. Zhao, and G. H. Wang. Structural growth sequences and electronic properties of zinc oxide clusters $(\mathrm{ZnO})_n$ (n=2-18). *J. Phys. Chem. C*, 111(13):4956–4963, 2007.

[143] B. L. Wang, X. Q. Wang, G. B. Chen, S. G. Nagase, and J. J. Zhao. Cage and tube structures of medium-sized zinc oxide clusters $(\mathrm{ZnO})_n$ (n = 24, 28, 36, and 48). *J. Chem. Phys.*, 128(14):No. 144710, 2008.

[144] J. Wang, L. Ma, J. Zhao, and K. A. Jackson. Structural growth behavior and polarizability of $\mathrm{Cd}_n\mathrm{Te}_n$ (n = 1–14) clusters. *J. Chem. Phys.*, 130(21):No. 214307, 2009.

[145] X. Wang, B. Wang, L. Tang, L. Sai, and J. Zhao. What is atomic structures of $(\mathrm{ZnO})_{34}$ magic cluster? *Phys. Lett. A*, 374(6):850–853, 2010.

[146] F. Weigend. Accurate Coulomb-fitting basis sets for H to Rn. *Phys. Chem. Chem. Phys.*, 8(9):1057–1065, 2006.

[147] F. Weigend and R. Ahlrichs. Balanced basis sets of split valence, triple zeta valence and quadruple zeta valence quality for H to Rn: Design and assessment of accuracy. *Phys. Chem. Chem. Phys.*, 7(18):3297–3305, 2005.

[148] C. Wen, T. Aida, I. Honma, H. Komiyama, and K. Yamada. The optical-absorption and photoluminescence spectra of C_{60} Single-Crystals. *J. Phys.: Condens. Matter*, 6(8):1603–1610, 1994.

[149] C. A. White and M. Head-Gordon. Derivation and efficient implementation of the fast multipole method. *J. Chem. Phys.*, 101(8):6593–6605, 1994.

[150] C. A. White and M. Head-Gordon. Fractional tiers in fast multipole method calculations. *Chem. Phys. Lett.*, 257(6–6):647–650, 1996.

[151] C. A. White, B. G. Johnson, P. M. W. Gill, and M. Head-Gordon. The continuous fast multipole method. *Chem. Phys. Lett.*, 230(1–2):8–16, 1994.

[152] S. B. Woodley, A. A. Sokol, C. R. A. Catlow, A. A. Al-Sunaidi, and S. M. Woodley. Structural and optical properties of Mg and Cd doped ZnO nanoclusters. *J. Phys. Chem. C*, 117(51):27127–27145, 2013.

[153] H.-S. Wu, F.-Q. Zhang, X.-H. Xu, C.-J. Zhang, and H. Jiao. Geometric and energetic aspects of aluminum nitride cages. *J. Phys. Chem. A*, 107(1):204–209, 2002.

[154] N. Xia, L.-F. Yuan, and J. Yang. Transition between direct gap and indirect gap in two dimensional hydrogenated honeycomb Si_xGe_{1-x} alloys. *Theor. Chem. Acc.*, 133(10):No. 1353, 2014.

[155] C. K. Xu, J. M. Wu, U. V. Desai, and D. Gao. High-efficiency solid-state dye-sensitized solar cells based on TiO_2-coated ZnO nanowire arrays. *Nano Lett.*, 12(5):2420–2424, 2012.

[156] H.-J. Zhai and L.-S. Wang. Probing the electronic structure and band gap evolution of titanium oxide clusters $(TiO_2)_n^-$ $(n = 1–10)$ using photoelectron spectroscopy. *J. Am. Chem. Soc.*, 129(10):3022–3026, 2007.

[157] Q. F. Zhang, C. S. Dandeneau, X. Y. Zhou, and G. Z. Cao. ZnO nanostructures for dye-sensitized solar cells. *Adv. Mater.*, 21(41):4087–4108, 2009.

[158] S. Zhang, Y. Zhang, S. Huang, H. Liu, P. Wang, and H. Tian. Theoretical investigation of growth, stability, and electronic properties of beaded ZnO nanoclusters. *J. Mater. Chem.*, 21(42):16905–16910, 2011.

[159] D. H. Zhao, J. Ruan, and Z. J. Cai. Combination prediction method of chaotic time series. *Chinese Sci. Bull.*, 52(4):570–573, 2007.

[160] J. Zhao, L. Wang, J. Jia, X. Chen, X. Zhou, and W. Lu. Lowest-energy structures of $\mathrm{Al}_n\mathrm{P}_n$ ($n = 1$–9) clusters from density functional theory. *Chem. Phys. Lett.*, 443(1-3):29–33, 2007.

[161] M. W. Zhao, Y. Y. Xia, Z. Y. Tan, X. D. Liu, and L. M. Mei. Design and energetic characterization of ZnO clusters from first-principles calculations. *Phys. Lett. A*, 372(1):39–43, 2007.

[162] Y. Zhao, C. Z. Li, X. H. Liu, F. Gu, H. L. Du, and L. Shi. Surface characteristics and microstructure of dispersed $\mathrm{TiO_2}$ nanoparticles prepared by diffusion flame combustion. *Mater. Chem. Phys.*, 107(2-3):344–349, 2008.

Ehrenwörtliche Erklärung

Ich erkläre hiermit ehrenwörtlich, dass ich die vorliegende Arbeit selbständig, ohne unzulässige Hilfe dritter und ohne Benutzung anderer als der angegebenen Hilfsmittel und Literatur angefertigt habe. Die aus anderen Quellen direkt oder indirekt übernommen Daten und Konzepte sind unter Angabe der Quelle gekennzeichnet.

Bei der Auswahl und Auswertung folgenden Materials haben mir die nachstehend aufgeführten Personen in der jeweils beschriebenen Weise unentgeltlich geholfen:

1. Prof. Dr. Marek Sierka - Betreuer
2. Dr. Piotr Janas - Hilfestellung bei Ausdruck- und Grammatikfragen

Weitere Personen waren an der inhaltlich-materiellen Erstellung der vorliegenden Arbeit nicht beteiligt. Insbesondere habe ich hierfür nicht die entgeltiche Hilfe von Vermittlungs- bzw. Beratungsdiensten (Promotionsberater oder andere Personen) in anspruch genommen.

Niemand hat von mir unmittelbar oder mittelbar geldwerte Leistungen für Arbeiten erhalten, die im Zusammenhang mit dem Inhalt der vorgelegten Dissertation stehen.

Die Arbeit wurde bisher weder im In- noch im Ausland in gleicher oder ähnlicher Form einer anderen Prüfungsbehörde vorgelegt.

Die geltende Promotionsordnung der Physikalisch-Astronomischen Fakultät ist mir bekannt.

Ich versichere ehrenwörtlich, dass ich nach bestem Wissen die reine Wahrheit gesagt und nichts verschwiegen habe.

Jena, 12.04.2017

Curriculum Vitae

Łazarski Roman

Date of Birth	September 29, 1988
Place of Birth	Rabka-Zdrój, Poland
1995-2001	Elementary School No. I, Rabka-Zdrój, Poland
2001-2004	Middle School No. II, Rabka-Zdrój, Poland
2004-2007	High School No. VIII, Kraków, Poland Mathematics – Chemistry – Informatics profile A-level equivalent
10/2007-06/2010	Jagiellonian University, Kraków, Poland Licencjat (Bachelor of Science equivalent) in Chemistry Final Grade: Very Good
10/2010-07/2012	Jagiellonian University, Kraków, Poland Magister (Master of Science equivalent) in Chemistry Master Thesis: Applicability Analysis of the Automatic Code Generation Techniques for Implementation of Selected Quantum-Chemical Calculations Final Grade: Very Good
09/2012-03/2017	Doctoral Candidate, Otto Schott Institute of Materials Research, Friedrich Schiller University Jena, Germany (with Prof. Dr. Marek Sierka)

Jena, 12.04.2017